


2012

Quadrature-based moment methods: High-order realizable schemes and multi-physics applications

Varun Vikas

Iowa State University

Follow this and additional works at: <https://lib.dr.iastate.edu/etd>

 Part of the [Aerospace Engineering Commons](#), [Applied Mathematics Commons](#), and the [Chemical Engineering Commons](#)

Recommended Citation

Vikas, Varun, "Quadrature-based moment methods: High-order realizable schemes and multi-physics applications" (2012). *Graduate Theses and Dissertations*. 12945.

<https://lib.dr.iastate.edu/etd/12945>

This Dissertation is brought to you for free and open access by the Iowa State University Capstones, Theses and Dissertations at Iowa State University Digital Repository. It has been accepted for inclusion in Graduate Theses and Dissertations by an authorized administrator of Iowa State University Digital Repository. For more information, please contact digirep@iastate.edu.

**Quadrature-based moment methods: High-order realizable schemes and
multi-physics applications**

by

Varun Vikas

A dissertation submitted to the graduate faculty
in partial fulfillment of the requirements for the degree of
DOCTOR OF PHILOSOPHY

Major: Aerospace Engineering

Program of Study Committee:

Z. J. Wang, Co-major Professor

Rodney O. Fox, Co-major Professor

Paul Durbin

Alric P. Rothmayer

Shankar Subramaniam

Iowa State University

Ames, Iowa

2012

Copyright © Varun Vikas, 2012. All rights reserved.

DEDICATION

To the four people who are beyond any acknowledgement,
who cared for me more than others when the conditions were adverse:
my late father, my mother, my sister and Mr. F. B. Karn.

TABLE OF CONTENTS

LIST OF TABLES	iv
LIST OF FIGURES	v
ACKNOWLEDGEMENTS	vi
ABSTRACT	vii
CHAPTER 1. GENERAL INTRODUCTION	1
1.1 Background	1
1.2 Original contributions of this dissertation	3
1.2.1 Development of high-order realizable schemes	3
1.2.2 Bubble-column flow modeling using QMOM	4
1.2.3 Radiation transport modeling using EQMOM	4
1.3 Outline of dissertation	4
CHAPTER 2. REALIZABLE HIGH-ORDER FINITE-VOLUME SCHEMES FOR QUADRATURE-BASED MOMENT METHODS	5
Abstract	5
2.1 Introduction	6
2.2 Quadrature method of moments	8
2.2.1 Kinetic equation	8
2.2.2 Moment transport equations	9
2.2.3 Quadrature-based closures	10
2.2.4 Finite-volume method	11
2.2.5 Solution algorithm	15
2.2.6 Non-realizability problem	16

2.3	Improved realizable finite-volume schemes	18
2.3.1	Basic idea	18
2.3.2	Realizability criterion for 1-D cases	21
2.3.3	Realizability criterion for 2-D/3-D cases	21
2.4	Multi-stage time-integration	24
2.4.1	RK2 scheme	24
2.4.2	RK2SSP scheme	25
2.4.3	Calculation of time-step size	27
2.5	Numerical results	28
2.5.1	Spatial accuracy study	28
2.5.2	Grid convergence study	29
2.5.3	Comparison of schemes for 1-D case with only convection terms	32
2.5.4	Comparison of schemes for 1-D case with both convection and drag terms	33
2.5.5	Comparison of schemes for 2-D case with only convection terms	36
2.5.6	Comparison of schemes for 2-D case with both convection and drag terms	38
2.6	Conclusions	42
	Appendix	43

**CHAPTER 3. REALIZABLE HIGH-ORDER FINITE-VOLUME SCHEMES
FOR QUADRATURE-BASED MOMENT METHODS APPLIED TO
DIFFUSION POPULATION BALANCE EQUATIONS**

	Abstract	47
3.1	Introduction	48
3.2	Quadrature-based moment method	50
3.2.1	Diffusion PBE	50
3.2.2	Moment transport equations	51
3.2.3	Quadrature-based closures	51
3.2.4	Finite-volume method	52
3.2.5	Non-realizability problem	54
3.3	Improved realizable finite-volume schemes	56

3.3.1	Basic idea	56
3.3.2	Consistency	59
3.3.3	Realizability conditions	60
3.3.4	Calculation of time-step size	62
3.4	Realizable schemes for multidimensional cases	63
3.4.1	Unstructured mesh	63
3.4.2	Uniform Cartesian mesh	68
3.5	Numerical results	70
3.5.1	Problem I	70
3.5.2	Problem II	71
3.5.3	Problem III	72
3.5.4	Problem IV	74
3.5.5	Problem V	75
3.6	Conclusions	76
CHAPTER 4. MODELING OF BUBBLE-COLUMN FLOWS WITH		
QUADRATURE-BASED MOMENT METHODS		79
	Abstract	79
4.1	Introduction	79
4.2	Description of Model	81
4.2.1	Liquid-phase governing equations	82
4.2.2	Bubble-phase governing equations	83
4.3	Description of Flow Solver	88
4.3.1	Liquid-phase solution strategy	89
4.3.2	Bubble-phase solution strategy	93
4.3.3	Coupling algorithm	96
4.4	Numerical Results	98
4.4.1	Description of 2-D test case	98
4.4.2	Lower gas flow rate	100
4.4.3	Higher gas flow rate	104

4.5	Conclusions	104
CHAPTER 5. RADIATION TRANSPORT MODELING USING EXTENDED		
QUADRATURE METHOD OF MOMENTS 108		
	Abstract	108
5.1	Introduction	109
5.2	Equations of radiative transfer	111
5.3	Extended quadrature method of moments	113
5.4	Solution algorithm	116
5.4.1	Convection term	116
5.4.2	External source term	118
5.4.3	Material coupling terms	119
5.5	Numerical results	120
5.5.1	Plane-source problem	121
5.5.2	Two-beam instability problem	122
5.5.3	Reed cell problem	123
5.5.4	Marshak wave problem	124
5.5.5	Su-Olson problem	125
5.6	Conclusions	126
CHAPTER 6. GENERAL CONCLUSIONS 135		
6.1	Development of high-order realizable schemes	135
6.2	Bubble-column flow modeling using QMOM	135
6.3	Radiation transport modeling using EQMOM	136
BIBLIOGRAPHY 137		

LIST OF TABLES

Table 2.1	L_1 error and order of accuracy of schemes using 1-node quadrature. . .	30
Table 2.2	L_1 error and order of accuracy of schemes using 2-node quadrature. . .	31
Table 3.1	Orders of accuracy based on L_1 errors for Problem I.	71
Table 3.2	Orders of accuracy based on L_1 errors for Problem II.	72
Table 3.3	Orders of accuracy based on L_1 errors for Problem III.	74
Table 3.4	Orders of accuracy based on L_1 errors for Problem IV.	74
Table 3.5	Orders of accuracy based on L_1 errors for Problem V.	76
Table 4.1	Gas (bubble) and liquid properties.	99
Table 4.2	Boundary conditions.	99
Table 5.1	Quantities and units.	121
Table 5.2	Opacities and external source terms for the Reed cell problem.	123

LIST OF FIGURES

Figure 2.1	Cells with faces aligned along Cartesian axes.	23
Figure 2.2	Grid convergence study for different schemes.	31
Figure 2.3	Comparison of schemes for 1-D case with only convection terms.	32
Figure 2.4	Fluid velocity for 1-D case.	33
Figure 2.5	Comparison of schemes using mean density for 1-D case with convection and drag terms.	34
Figure 2.6	Comparison of schemes using mean velocity for 1-D case with convection and drag terms.	35
Figure 2.7	Mean particle density for crossing particle jets for different schemes at two times.	37
Figure 2.8	Fluid velocity for 2-D Taylor-Green flow.	38
Figure 2.9	Grid resolution study of mean particle density in 2-D Taylor-Green flow at $t = 4$ with 1 st -order scheme.	39
Figure 2.10	Grid resolution study of mean particle density in 2-D Taylor-Green flow at $t = 4$ with <i>quasi</i> -2 nd -order scheme.	40
Figure 2.11	Mean particle density in 2-D Taylor-Green flow at $t = 4$ on triangular mesh with different schemes and cell numbers.	41
Figure 2.12	Particle number density in 2-D Taylor-Green flow obtained by Lostec et al. [64] using a Lagrangian simulation. Density is proportional to darkness.	42
Figure 3.1	Second-order reconstruction stencils for the terms involving weights and abscissas at the face e of an unstructured mesh.	64

Figure 3.2	<i>Quasi</i> -fourth-order reconstruction stencils for the terms involving weights and abscissas at the face $(i + \frac{1}{2}, j)$ of a uniform Cartesian mesh.	70
Figure 3.3	L_1 errors for Problem II: M^0 {2 nd -order} ($-\bullet-$), M^0 { <i>quasi</i> -4 th -order} ($-\blacksquare-$), M^1 {2 nd -order} ($-\bullet-$), M^1 { <i>quasi</i> -4 th -order} ($-\star-$).	72
Figure 3.4	L_1 errors for Problem III: M^0 {2 nd -order} ($-\bullet-$), M^0 { <i>quasi</i> -4 th -order} ($-\blacksquare-$), M^1 {2 nd -order} ($-\bullet-$), M^1 { <i>quasi</i> -4 th -order} ($-\star-$), M^2 {2 nd -order} ($-\blacklozenge-$), M^2 { <i>quasi</i> -4 th -order} ($-\bullet-$).	77
Figure 3.5	L_1 errors for Problem IV: M^0 {moment-based} ($-\bullet-$), M^0 {weight/abscissa-based} ($-\blacksquare-$), M^1 {moment-based} ($-\bullet-$), M^1 {weight/abscissa-based} ($-\star-$), M^2 {moment-based} ($-\blacklozenge-$), M^2 {weight/abscissa-based} ($-\bullet-$), M^3 {moment-based} ($-\blacksquare-$), M^3 {weight/abscissa-based} ($-\blacklozenge-$).	78
Figure 4.1	Control volume and its neighbors for an unstructured mesh.	89
Figure 4.2	Schematic of the control flow for the coupled bubbly flow solver.	97
Figure 4.3	Schematic of the 2-D domain used for simulations.	98
Figure 4.4	Instantaneous contour plots of bubble-phase volume fraction (ε_b) for gas flow rate equal to 1.6 l/min at $t = 60$ s (a) using QBMM, (b) using Eulerian-Lagrangian approach.	102
Figure 4.5	Instantaneous contour plots for gas flow rate equal to 1.6 l/min at $t = 60$ s for liquid-phase (a) velocity magnitude ($ \mathbf{U}_l $, m s ⁻¹), (b) velocity vectors.	102
Figure 4.6	Instantaneous contour plots of bubble-phase (a) granular temperature (m s ⁻¹), (b) Mach number, (c) Stokes number for gas flow rate equal to 1.6 l/min at $t = 60$ s.	103
Figure 4.7	Instantaneous contour plots of bubble-phase volume fraction (ε_b) for gas flow rate equal to 1.6 l/min.	103
Figure 4.8	Instantaneous contour plots of bubble-phase volume fraction (ε_b) for gas flow rate equal to 8.0 l/min at $t = 60$ s (a) using QBMM, (b) using Eulerian-Lagrangian approach.	105

Figure 4.9	Instantaneous contour plots for gas flow rate equal to 8.0 l/min at $t = 60$ s for liquid-phase (a) velocity magnitude ($ \mathbf{U}_l $, m s $^{-1}$), (b) velocity vectors.	105
Figure 4.10	Instantaneous contour plots of bubble-phase (a) granular temperature (m s $^{-1}$), (b) Mach number, (c) Stokes number for gas flow rate equal to 8.0 l/min at $t = 60$ s.	106
Figure 4.11	Instantaneous contour plots of bubble-phase volume fraction (ε_b) for gas flow rate equal to 8.0 l/min.	106
Figure 5.1	Solutions for the plane-source problem at $ct = 1$: Semi-analytic (—), 220 cells (⋯⋯⋯), 440 cells (----), 880 cells (- -).	127
Figure 5.2	Solutions for the plane-source problem at $ct = 2$: Semi-analytic (—), 300 cells (⋯⋯⋯), 600 cells (----), 1200 cells (- -).	128
Figure 5.3	Solutions for the plane-source problem at $ct = 4$: Semi-analytic (—), 410 cells (⋯⋯⋯), 820 cells (----), 1640 cells (- -).	129
Figure 5.4	Solutions for the two-beam instability problem at steady state: Semi-analytic (—), 100 cells (⋯⋯⋯), 200 cells (----), 400 cells (- -).	130
Figure 5.5	Solutions for the Reed cell problem at steady state: Reference (—), 100 cells (⋯⋯⋯), 200 cells (----), 400 cells (- -).	131
Figure 5.6	Solutions for the Marshak wave problem at $ct = 300, 1500, 3000$: Semi-analytic (—), 30 cells (⋯⋯⋯), 60 cells (----), 120 cells (- -).	132
Figure 5.7	Solutions for the Su-Olson problem at $ct = 1, 3.16, 10$: Semi-analytic (●, ■, ▲), 240 cells (⋯⋯⋯), 480 cells (----), 960 cells (- -).	133
Figure 5.8	Solutions for the Su-Olson problem at $ct = 1, 3.16, 10$ on a logarithmic scale: Semi-analytic (●, ■, ▲), 240 cells (⋯⋯⋯), 480 cells (----), 960 cells (- -).	134

ACKNOWLEDGEMENTS

I have been fortunate enough to have not one but two of the best possible advisers - Dr. Wang and Dr. Fox. I would like to thank them for all the help, support and motivation that they provided over the whole period of my PhD. My special thanks to them for giving me enough freedom in my research work. I would like to thank Dr. Durbin, Dr. Rothmayer and Dr Shankar for being on my committee. I owe special gratitude to Dr. Shankar for being my Preparing Future Faculty mentor and helping me with multiphase flows.

I would like to acknowledge the financial support from National Science Foundation (Grant Number: CISE-0830214) without which, probably I wouldn't even have been here in the first place. Despite the financial support from the grant, it would have been extremely difficult for me if I would not have got extra financial help from my friends - Piyush, Amit, Vidya, Om Prakash, Takanori, Anoop, Prasanna, Ravi, Bo, Chakresh, Vishwanath and Rupesh in particular. I owe a lot to them!

For his unending help and support, both financial and technical, I owe a debt to Takanori that cannot be repaid. He has been kind and patient in answering my questions and has contributed immensely to my knowledge of CFD. Other than the technical conversations, I have enjoyed the frequent trips to Old Chicago with him. Besides Takanori, I would like to thank the past and current members of the research group with whom I have enjoyed many conversations - Ying, Andrew, Meilin, Lei, Ben, Jeff and the two kids. I also owe my sincere gratitude to Jason (Cansheng), Alberto and Sudheer for technical conversations and to Vidya, Prasanna, Kaustubh, Praveen, Sunil, Hari, Ravi, Xu and De for not so technical conversations. The coffee sessions at Stomping Grounds with Alberto and the movie trips with Prasanna have been very relaxing.

ABSTRACT

Kinetic equations occur in mesoscopic models for many physical phenomena. The direct solution of the kinetic equation is prohibitively expensive due to the high dimensionality of the space of independent variables. A viable alternative is to reformulate the problem in terms of the moments of the distribution function. Recently, a suite of quadrature-based moment methods has been developed for approximating solutions to kinetic equations. This suite of quadrature-based moment methods has several desirable properties that makes it more efficient and robust compared to the other moment methods. Despite these desirable properties, there is often a bottleneck associated with these methods. Use of higher than first-order discretization schemes for the convection terms and higher than second-order discretization schemes for the diffusion terms often leads to non-realizable moment sets. A non-realizable moment set does not correspond to a non-negative distribution function. The discretization schemes that can guarantee the non-negativity of the distribution function are called realizable schemes. The standard high-order discretization schemes are non-realizable. As a part of current research study, a set of high-order realizable schemes has been developed for both convection and diffusion terms that guarantee the non-negativity of the distribution function using constraints on the time step size, known as realizability conditions. In addition, the current study also shows the application of quadrature-based moment methods to two multi-physics phenomena – bubble-column flow and radiation transport. The two problems have been formulated and solved using the quadrature-based moment methods with particular attention to realizability.

CHAPTER 1. GENERAL INTRODUCTION

1.1 Background

Many physical phenomena can be described by studying the time evolution of a system consisting of a large number of elementary objects, also referred to as particles. The identity and properties of these particles vary from one phenomenon to another. Depending on the physical phenomenon under consideration, the particles can be electrons [117], photons [13], bubbles [116] or gas molecules [17]. The mathematical study of such systems leads to a class of partial differential equations called kinetic equations. Solution of kinetic equations is essential to understand the dynamics of these systems. However, any attempt at obtaining a direct solution [8, 77] of a kinetic equation is prohibitively expensive due to the high dimensionality of the space of independent variables. Lagrangian solvers [10] and Monte Carlo methods [49], based on the idea of particle tracking are often employed to obtain accurate solutions. However, a large number of particles are needed by these methods which makes them computationally very expensive. Moreover, these methods are subject to statistical noise. To avoid the computational cost of a direct solver or a particle tracking method, continuum models which are valid only when the system is close to equilibrium have been formulated. For example, in the context of dispersed-phase flows, like bubble-column flows, these models are referred to as hydrodynamic models [27]. For the dispersed-phase flows that are far away from equilibrium, the hydrodynamic models do not work properly. In particular, phenomena such as particle-trajectory crossing cannot be captured. In the context of radiation transport modeling, equilibrium models are referred to as diffusion models [78]. The diffusion models work well only for the optically thick systems that are nearly opaque and allow very little light to pass through. For optically thin systems, in which very little material is present and most of the light passes through,

diffusion models fail to give an accurate solution.

Moment methods [43, 104] are a class of methods that use a continuum formulation but do not make any assumption about equilibrium of the system. As a result, moment methods are valid in both equilibrium and non-equilibrium regimes. Moment methods are based on the idea of tracking a set of moments of the distribution function. The accuracy of the moment methods can be systematically improved by increasing the number of tracked moments. However, the system of moment transport equations is not closed and this leads to the well-known moment-closure problem [100]. The moment-closure problem is solved by specifying a form of the distribution function and an algorithm (moment-inversion algorithm) using which the distribution function is reconstructed from the tracked moments. The moment methods differ in the form of the distribution function they assume and the moment-inversion algorithm that they use. The quadrature-based moment methods (QBMM) are a class of moment methods that use quadrature-based closures. Different versions of QBMM are available. Quadrature method of moments (QMOM) [25, 33, 34, 35, 71] assumes that the distribution function is a weighted sum of delta functions. The locations of the delta functions are called abscissas. QMOM has been developed for uni-variate, bi-variate and tri-variate cases. For some problems, pointwise values of the distribution function are required that QMOM fails to provide. To solve this problem, a continuous form of QMOM, referred to as extended quadrature method of moments (EQMOM) [127] has been developed. EQMOM assumes the distribution function is a weighted sum of smooth kernel density functions, with each kernel density function centered around an abscissa. Currently, EQMOM exists only for uni-variate cases. Robust moment-inversion algorithms have been developed for both QMOM and EQMOM. As both QMOM and EQMOM use non-negative basis functions, when the weights are non-negative, the non-negativity of the distribution function is also guaranteed. Moreover, unlike many other moment methods, the moment-inversion algorithms for QMOM and EQMOM do not involve solving a constrained, convex optimization problem. The inversion algorithm for QMOM is non-iterative while the inversion algorithm for EQMOM involves only a one-dimensional root finding method. These two properties - non-negative distribution function and an efficient inversion algorithm - make QBMM preferable over other moment methods.

QBMM has already been successfully applied to gas-particle flows [79]. In the current research study, the purview of QBMM is extended to two more applications - gas-liquid flows (bubble-columns flows) and radiation transport. A fully two-way coupled flow solver is developed that solves the incompressible Navier-Stokes equation for the liquid phase and moment transport equations using QMOM for the dispersed bubble phase. For radiation transport modeling, EQMOM is used.

As mentioned earlier, if the weights are non-negative, the distribution function assumed by QBMM is also non-negative. The weights and abscissas are obtained from the tracked moments using the moment-inversion algorithm. The weights are non-negative only if the set of moments is realizable. Moreover, if the moment set is non-realizable, the abscissas may lie outside the support interval of the distribution function. To avoid this, it is of paramount importance that the moment set always remain realizable. It has been observed that the use of standard high-order discretization schemes often leads to negative weights and abscissas that are outside the support interval of the distribution function. As a part of the current research study, it is shown that the use of standard high-order discretization schemes cannot guarantee the realizability of the moment set. Moreover, new high-order realizable schemes are developed for convection and diffusion terms, that guarantee the realizability of the moment set if the time step size satisfies the constraints called realizability conditions.

1.2 Original contributions of this dissertation

The original and significant contributions of this research work are summarized in the following.

1.2.1 Development of high-order realizable schemes

Realizability of standard high-order finite-volume schemes in both space and time is discussed. The issue of reconstruction of moments vs reconstruction of weights and abscissas is debated. New realizable high-order finite-volume schemes based on the reconstruction of weights and abscissas are proposed and suitable realizability criteria are derived.

1.2.2 Bubble-column flow modeling using QMOM

A novel approach to model bubble-column flows using QMOM is presented. A fully two-way coupled flow solver is developed that solves the incompressible Navier-Stokes equation for the liquid phase and moment transport equations using QMOM for the dispersed bubble phase.

1.2.3 Radiation transport modeling using EQMOM

The equations governing radiation transport are formulated using EQMOM with special attention to realizability and a set of standard one-dimensional benchmark problems encompassing optically thin, thick and transition regimes is solved.

1.3 Outline of dissertation

The dissertation consists of a set of papers that has been published in, submitted to or prepared for submission to scholarly journals.

Chapter 2 is the paper titled *Realizable high-order finite-volume schemes for quadrature-based moment methods*. This paper [115] is published in Journal of Computational Physics.

Chapter 3 is the paper titled *Realizable high-order finite-volume schemes for quadrature-based moment methods applied to diffusion population balance equations*. This paper is submitted to Journal of Computational Physics.

Chapter 4 is the paper titled *Modeling of bubble-column flows with quadrature-based moment methods*. This paper [116] is published in Chemical Engineering Science.

Chapter 5 is the paper titled *Radiation transport modeling using extended quadrature method of moments*. This paper is submitted to Journal of Computational Physics.

Chapter 6 summarizes the general conclusions from the current research study.

CHAPTER 2. REALIZABLE HIGH-ORDER FINITE-VOLUME SCHEMES FOR QUADRATURE-BASED MOMENT METHODS

A paper published in Journal of Computational Physics

Varun Vikas¹, Z. J. Wang, Alberto Passalacqua, Rodney O. Fox

Abstract

Dilute gas-particle flows can be described by a kinetic equation containing terms for spatial transport, gravity, fluid drag and particle-particle collisions. However, direct numerical solution of kinetic equations is often infeasible because of the large number of independent variables. An alternative is to reformulate the problem in terms of the moments of the velocity distribution. Recently, a quadrature-based moment method was derived for approximating solutions to kinetic equations. The success of the new method is based on a moment-inversion algorithm that is used to calculate non-negative weights and abscissas from the moments. The moment-inversion algorithm does not work if the moments are non-realizable, which might lead to negative weights. It has been recently shown [25] that realizability is guaranteed only with the 1st-order finite-volume scheme that has an inherent problem of excessive numerical diffusion. The use of high-order finite-volume schemes may lead to non-realizable moments. In the present work, realizability of the finite-volume schemes in both space and time is discussed for the first time. A generalized idea for developing realizable high-order finite-volume schemes for quadrature-based moment methods is presented. These finite-volume schemes give remarkable improvement in the solutions for a certain class of problems. It is also shown that the standard Runge-Kutta time-integration schemes do not guarantee realizability. However,

¹Primary researcher and author.

realizability can be guaranteed if strong stability-preserving (SSP) Runge-Kutta schemes are used. Numerical results are presented on both Cartesian and triangular meshes.

2.1 Introduction

Kinetic equations occur in mesoscopic models for many physical phenomena, such as rarefied gases [11, 19, 20, 43, 76, 109], plasmas [15, 63, 123], multiphase flows [25, 96, 112, 122], optics [7, 30, 40, 94, 95], and quantum physics [41, 50, 51], to name just a few. In this work, we will use the kinetic equation describing dilute gas-particle flows as an example application. However, the proposed numerical schemes can easily be extended to treat a wide range of kinetic equations describing other applications.

Gas-particle flows occur in many engineering and natural systems such as fluidized-bed reactors, catalytic crackers, volcanic ash transport in the atmosphere, and helicopter brown-out. Currently, there exist several different approaches for simulating the kinetic equation describing the particle phase and its coupling to the gas phase. In general, all approaches use the same type of flow solver for the gas phase, but they differ in the way in which the kinetic equation is treated:

- (i) direct solver that discretizes the velocity phase space of the particle number density function [8, 77],
- (ii) Lagrangian solver that tracks all the particles individually [10],
- (iii) hydrodynamic models with kinetic-theory moment closures [31],
- (iv) quadrature method of moments (QMOM) that solves for moments of the particle number density function with quadrature-based closures [25, 33, 65, 79].

In many applications, the direct solution of the kinetic equation is prohibitively expensive due to the high dimensionality of the space of independent variables, while Lagrangian solvers are computationally very expensive, since the number of particles to be tracked is very large. On the other hand, hydrodynamic models are developed assuming that the Knudsen number of the particle phase is very small, which is equivalent to assuming a Maxwellian (or nearly

Maxwellian) equilibrium particle velocity distribution. This, however, is not correct in relatively dilute gas-particle flows, where the Knudsen number can be high, the collision frequency is small and phenomena like particle trajectory crossing can occur. In particular, Desjardins et al. [25] showed that the assumption that a gas-particle flow can be described accounting for only the mean momentum of the particle phase leads to incorrect predictions of all the velocity moments, including the particle number density, showing the need of using a multi-velocity method, in order to correctly capture the physics of the flow. Similar observations were made for moderately collisional gas-particle flows by Sakiz and Simonin [96].

QMOM for gas-particle flow [33, 34, 35] is based on the idea of tracking a set of velocity moments of arbitrarily high order, providing closures to the source terms and the moment spatial fluxes in the moment transport equations by means of a quadrature approximation of the number density function. The key step of the approach is an inversion algorithm that allows one to uniquely determine a set of weights and abscissas from the set of transported moments. The condition for the inversion algorithm to be applied is that the set of moments is realizable, meaning it actually corresponds to a velocity distribution. This condition is not generally satisfied by the traditional finite-volume methods used in computational fluid dynamics.

Desjardins et al. [25] recently showed that realizability is guaranteed only with the 1st-order finite-volume scheme. The use of any other high-order finite-volume scheme may lead to non-realizable moments, thereby resulting in negative weights. Weights are representative of particle density and hence cannot be negative. This limitation in turn leads to the use of a highly refined mesh for computation as a first-order finite-volume scheme produces highly diffused solutions on a coarse mesh. For this reason, improved finite-volume schemes are sought that could provide less-diffused solutions and simultaneously guarantee the realizability of moments.

In the present work, a generalized idea for developing improved finite-volume schemes for quadrature-based moment methods is presented. The realizability of the new improved finite-volume schemes is guaranteed under suitable realizability criteria. These new schemes give remarkable improvement in the solutions for the class of problems where the velocity abscissas are constant over a range of cells. The present work also shows that the standard Runge-Kutta time-integration schemes do not guarantee realizability. However, the realizability can

be guaranteed if strong stability-preserving (SSP) Runge-Kutta schemes [42] are used.

The remainder of this paper is organized as follows. In Sec. 2.2, QMOM is reviewed. Section 2.2 also discusses finite-volume schemes and their realizability properties. Thereafter, in Sec. 2.3, new realizable high-order finite-volume schemes are presented. In Sec. 2.4, multi-stage time-integration is discussed and realizability properties of the standard RK2 and RK2SSP schemes are presented. Section 2.5 presents some numerical results including accuracy studies. Conclusions from the present study are summarized in Sec. 2.6. Finally, in the appendix to this chapter, we present an extension of the realizable schemes to velocity-independent density functions.

2.2 Quadrature method of moments

2.2.1 Kinetic equation

Dilute gas-particle flows can be modeled by a kinetic equation [16, 19, 104] of the form:

$$\partial_t f + \mathbf{v} \cdot \partial_{\mathbf{x}} f + \partial_{\mathbf{v}} \cdot (f \mathbf{F}) = \mathbb{C}, \quad (2.1)$$

where $f(\mathbf{v}, \mathbf{x}, t)$ is the velocity-based number density function, \mathbf{v} is the particle velocity, \mathbf{F} is the force acting on an individual particle, and \mathbb{C} is the collision term representing the rate of change in the number density function due to particle-particle collisions. The collision term can be described using the Bhatnagar-Gross-Krook (BGK) collision operator [9]:

$$\mathbb{C} = \frac{1}{\tau} (f_{\text{eq}} - f), \quad (2.2)$$

where τ is the characteristic collision time, and f_{eq} is the Maxwellian equilibrium number density function given by

$$f_{\text{eq}}(\mathbf{v}) = \frac{M^0}{\sqrt{(2\pi\sigma_{\text{eq}})^3}} \exp\left(-\frac{|\mathbf{v} - \mathbf{U}_p|^2}{2\sigma_{\text{eq}}}\right), \quad (2.3)$$

in which \mathbf{U}_p is the mean particle velocity, σ_{eq} is the equilibrium variance and $M^0 = \int f d\mathbf{v}$ is the particle number density. In gas-particle flows, the force term is given by the sum of the gravitational contribution (\mathbf{F}_g) and the drag term (\mathbf{F}_d) exerted from the fluid on the particles:

$$\mathbf{F} = \mathbf{F}_g + \mathbf{F}_d. \quad (2.4)$$

For dilute gas-particle flows, the drag force on a particle can be approximated by

$$\mathbf{F}_d = \frac{3m_p\rho_g}{4\rho_p d_p} C_d |\mathbf{U}_r| \mathbf{U}_r, \quad (2.5)$$

where $\mathbf{U}_r = \mathbf{U}_g - \mathbf{U}_p$ is the relative velocity between two phases, \mathbf{U}_g is the gas velocity, \mathbf{U}_p is the particle phase local mean velocity, ρ_g and ρ_p are gas and particle densities, respectively, and d_p is the particle diameter. The drag coefficient C_d is given by the Schiller-Naumann correlation [98]:

$$C_d = \frac{24}{\text{Re}_p} (1 + 0.15 \text{Re}_p^{0.687}), \quad (2.6)$$

in which $\text{Re}_p = \rho_g d_p |\mathbf{U}_g - \mathbf{U}_p| / \mu_g$, μ_g being the dynamic viscosity of gas phase.

2.2.2 Moment transport equations

In the quadrature-based moment method of Fox [33, 34, 35], a set of moments of the number density function f is transported and its evolution in space and time is tracked. Each element of the moment set is defined through integrals of the number density function. For the first few moments the defining integrals are:

$$M^0 = \int f d\mathbf{v}, \quad M_i^1 = \int v_i f d\mathbf{v}, \quad M_{ij}^2 = \int v_i v_j f d\mathbf{v}, \quad M_{ijk}^3 = \int v_i v_j v_k f d\mathbf{v}. \quad (2.7)$$

In these equations, the superscript of M represents the order of corresponding moment. Moment transport equations are obtained by applying the definition of moments to (2.1). The transport equations for moments in (2.7) can be written as:

$$\begin{aligned} \frac{\partial M^0}{\partial t} + \frac{\partial M_i^1}{\partial x_i} &= 0, \\ \frac{\partial M_i^1}{\partial t} + \frac{\partial M_{ij}^2}{\partial x_j} &= g_i M^0 + D_i^1, \\ \frac{\partial M_{ij}^2}{\partial t} + \frac{\partial M_{ijk}^3}{\partial x_k} &= g_i M_j^1 + g_j M_i^1 + C_{ij}^2 + D_{ij}^2, \\ \frac{\partial M_{ijk}^3}{\partial t} + \frac{\partial M_{ijkl}^4}{\partial x_l} &= g_i M_{jk}^2 + g_j M_{ik}^2 + g_k M_{ij}^2 + C_{ijk}^3 + D_{ijk}^3. \end{aligned} \quad (2.8)$$

In (2.8), g_i, g_j, g_k are the components of gravity, $D_i^1, D_{ij}^2, D_{ijk}^3$ are due to the drag force and C_{ij}^2, C_{ijk}^3 are due to collisions.

2.2.3 Quadrature-based closures

Using the BGK model, the collision terms in (2.8) can be closed. However, the set of transport equations in (2.8) is still unclosed because of the spatial flux and drag terms. Each equation contains the spatial fluxes of the moments of order immediately higher. In quadrature-based moment methods, quadrature formulas are used to provide closures to these terms in the moment transport equations, by introducing a set of weights and abscissas. The number density function f is written in terms of the quadrature weights (n_α) and abscissas (\mathbf{U}_α) using a Dirac delta representation:

$$f(\mathbf{v}) = \sum_{\alpha=1}^{\beta} n_\alpha \delta(\mathbf{v} - \mathbf{U}_\alpha). \quad (2.9)$$

The method based on (2.9) is called β -node quadrature method. The moments can be computed as a function of quadrature weights and abscissas by using the above definition of f in (2.7):

$$M^0 = \sum_{\alpha=1}^{\beta} n_\alpha, \quad M_i^1 = \sum_{\alpha=1}^{\beta} n_\alpha U_{i\alpha}, \quad M_{ij}^2 = \sum_{\alpha=1}^{\beta} n_\alpha U_{i\alpha} U_{j\alpha}, \quad M_{ijk}^3 = \sum_{\alpha=1}^{\beta} n_\alpha U_{i\alpha} U_{j\alpha} U_{k\alpha}. \quad (2.10)$$

The source terms due to drag and gravity are computed as:

$$\begin{aligned} D_i^1 &= \sum_{\alpha=1}^{\beta} \frac{n_\alpha}{m_p} F_{i\alpha}, \\ D_{ij}^2 &= \sum_{\alpha=1}^{\beta} \frac{n_\alpha}{m_p} (F_{i\alpha} U_{j\alpha} + F_{j\alpha} U_{i\alpha}), \\ D_{ijk}^3 &= \sum_{\alpha=1}^{\beta} \frac{n_\alpha}{m_p} (F_{i\alpha} U_{j\alpha} U_{k\alpha} + F_{j\alpha} U_{k\alpha} U_{i\alpha} + F_{k\alpha} U_{i\alpha} U_{j\alpha}). \end{aligned} \quad (2.11)$$

The details of the computation of the force terms $F_{i\alpha}$, $F_{j\alpha}$ and $F_{k\alpha}$, can be found in [33].

In order to ensure that the moments remain realizable and that the discretized fluxes are hyperbolic, the spatial flux terms are closed according to their kinetic description [87, 23, 82, 25]. Each moment involved in the spatial derivative is decomposed into two contributions, as shown in (2.12) for the zero-order moments:

$$M_i^1 = \int_{-\infty}^0 v_i \left(\int f dv_j dv_k \right) dv_i + \int_0^{+\infty} v_i \left(\int f dv_j dv_k \right) dv_i. \quad (2.12)$$

In a 1-D case, the left integral will account for particles going from left to right and the right integral will account for particles going from right to left at the face. Using (2.9), (2.12) can

be written as:

$$M_i^1 = \sum_{\alpha=1}^{\beta} n_{\alpha} \min(0, U_{i\alpha}) + \sum_{\alpha=1}^{\beta} n_{\alpha} \max(0, U_{i\alpha}). \quad (2.13)$$

For a 1-D case, the left integral/summation in (2.12)/(2.13) is evaluated using the values on left side of the face and right integral/summation is evaluated using the values on right side of the face.

In order to solve the abovementioned moment transport equations, boundary conditions are needed. These boundary conditions can be specified either in terms of moments or in terms of the weights and abscissas. The latter approach is more convenient and is followed in the present work. In this work, three types of boundary conditions are used: Dirichlet, periodic and wall-reflective. At a Dirichlet boundary, the weights and abscissas are specified. Periodic boundary conditions copy the weights and abscissas from the outgoing periodic boundary cell to the corresponding incoming periodic boundary cell. The boundary conditions at the walls are set so that a particle that collides with the wall is specularly reflected. This condition corresponds to changing the sign of the velocity component of the particle along the direction perpendicular to the wall. The implementation of this boundary condition in the quadrature-based algorithm is done by changing the sign of the abscissas in the appropriate direction [79]. If $i = 0$ indicates the position of the wall, perpendicular to the second direction of reference frame, and $i = 1$ indicates the neighboring computational cell, the boundary condition can be written as:

$$\begin{pmatrix} n_{\alpha} \\ U_{\alpha} \\ V_{\alpha} \\ W_{\alpha} \end{pmatrix}_{i=0} = \begin{pmatrix} n_{\alpha}/e_w \\ U_{\alpha} \\ -e_w V_{\alpha} \\ W_{\alpha} \end{pmatrix}_{i=1}, \quad (2.14)$$

where e_w is the particle-wall restitution coefficient. All the boundary conditions are applied using a ghost-cell approach.

2.2.4 Finite-volume method

The moment transport equations in (2.8) contain convection, drag and collision terms. The three terms are treated separately using an *operator-splitting* technique. The solution

algorithm involving all the terms is given later. The collision and the force terms do not create non-realizability problems. Hence for all the analysis, these terms are dropped. For simplicity, a one-dimensional case with two quadrature nodes is discussed here. A general 3-D case is presented in a later section. For the 1-D case, the set of moment transport equations after dropping collision and drag terms can be written as:

$$\frac{\partial \mathbf{W}}{\partial t} + \frac{\partial \mathbf{H}(\mathbf{W})}{\partial x} = 0, \quad (2.15)$$

where

$$\mathbf{W} = [M^0 \ M^1 \ M^2 \ M^3]^\top \quad \text{and} \quad \mathbf{H}(\mathbf{W}) = [M^1 \ M^2 \ M^3 \ M^4]^\top. \quad (2.16)$$

For a 2-node quadrature there are two weights (n_1, n_2) and two abscissas (U_1, U_2) . Let the set of weights and abscissas be denoted as $\mathbf{N} = [n_1 \ n_2 \ U_1 \ U_2]^\top$. The first four moments can be written in terms of these weights and abscissas as:

$$\begin{aligned} M^0 &= n_1(U_1)^0 + n_2(U_2)^0, \\ M^1 &= n_1(U_1)^1 + n_2(U_2)^1, \\ M^2 &= n_1(U_1)^2 + n_2(U_2)^2, \\ M^3 &= n_1(U_1)^3 + n_2(U_2)^3. \end{aligned} \quad (2.17)$$

In the first two equations for M^0 and M^1 , powers of U_1 and U_2 are redundant.

The conserved moments and moment fluxes in (2.16) can be written in terms of the number density function:

$$\mathbf{W} = \int \mathbf{K}(v) f(v) dv, \quad \mathbf{H}(\mathbf{W}) = \int v \mathbf{K}(v) f(v) dv, \quad (2.18)$$

where

$$\mathbf{K}(v) = [1 \ v \ v^2 \ v^3]^\top. \quad (2.19)$$

The moments in (2.15) can be advanced in time using a finite-volume scheme. If a single-stage explicit time-integration scheme is used, the updated set of moments can be written as:

$$\mathbf{W}_i^{n+1} = \mathbf{W}_i^n - \frac{\Delta t}{\Delta x} \left[\mathbf{G} \left(\mathbf{W}_{i+1/2,l}^n, \mathbf{W}_{i+1/2,r}^n \right) - \mathbf{G} \left(\mathbf{W}_{i-1/2,l}^n, \mathbf{W}_{i-1/2,r}^n \right) \right], \quad (2.20)$$

where superscripts n and $n + 1$ denote time levels, \mathbf{G} is the numerical flux function evaluated at cell interfaces, and l and r denote the left and right states at the interfaces respectively.

Henceforth, the variables with subscript i will denote the cell-averaged values and the ones with $(i + 1/2)$ or $(i - 1/2)$ as subscript will denote the reconstructed values at the interfaces.

\mathbf{G} is defined as:

$$\mathbf{G}(\mathbf{W}_l, \mathbf{W}_r) = \int v^+ \mathbf{K} f_l dv + \int v^- \mathbf{K} f_r dv, \quad (2.21)$$

where

$$v^+ = \frac{1}{2}(v + |v|) \quad \text{and} \quad v^- = \frac{1}{2}(v - |v|). \quad (2.22)$$

This corresponds to a splitting between particles going from left to right (first term) and particles going from right to left (second term). Inserting the expression for f in (2.21) yields:

$$\mathbf{G}(\mathbf{W}_l, \mathbf{W}_r) = \mathbf{H}^+(\mathbf{W}_l) + \mathbf{H}^-(\mathbf{W}_r), \quad (2.23)$$

with

$$\begin{aligned} \mathbf{H}^+(\mathbf{W}_l) &= n_{1l} \max(U_{1l}, 0) \begin{pmatrix} 1 \\ U_{1l} \\ U_{1l}^2 \\ U_{1l}^3 \end{pmatrix} + n_{2l} \max(U_{2l}, 0) \begin{pmatrix} 1 \\ U_{2l} \\ U_{2l}^2 \\ U_{2l}^3 \end{pmatrix}, \\ \mathbf{H}^-(\mathbf{W}_r) &= n_{1r} \min(U_{1r}, 0) \begin{pmatrix} 1 \\ U_{1r} \\ U_{1r}^2 \\ U_{1r}^3 \end{pmatrix} + n_{2r} \min(U_{2r}, 0) \begin{pmatrix} 1 \\ U_{2r} \\ U_{2r}^2 \\ U_{2r}^3 \end{pmatrix}. \end{aligned} \quad (2.24)$$

Before discussing the first-, second- and third-order finite-volume schemes, it is worth noticing that, in order to calculate the fluxes at the interface, variables need to be reconstructed at the faces of each cell. However, there is an ambiguity in the choice of variables to be chosen for reconstruction. Two choices are possible: (i) reconstructing the moments ($\mathbf{H}(\mathbf{W}) = [M^1 \ M^2 \ M^3 \ M^4]^T$) and (ii) reconstructing the weights and abscissas ($\mathbf{N} = [n_1 \ n_2 \ U_1 \ U_2]^T$). For the first-order finite-volume scheme both choices are equivalent. However, for second or any high-order finite-volume schemes, these two choices are in general different. The former approach often leads to non-realizable moments, especially in the problems involving discontinuous velocity fields. For this reason, the second approach is adopted in this work. In the

sections below, any reconstruction essentially refers to reconstruction of the weights and abscissas. For example, $\mathbf{W}_{i+1/2,l}$ refers to moments at the left side of interface $i + 1/2$ calculated using the reconstructed values of the weights and abscissas.

2.2.4.1 First-order finite-volume scheme

The 1st-order finite-volume scheme for solving moment transport equations uses a piecewise constant approximation and is described in [25]. The weights and abscissas are assumed to be constant over a cell:

$$\mathbf{N}_{i-1/2,r}^n = \mathbf{N}_i^n, \quad \mathbf{N}_{i+1/2,l}^n = \mathbf{N}_i^n. \quad (2.25)$$

2.2.4.2 Second-order finite-volume scheme

In the 2nd-order finite-volume scheme, a piecewise linear reconstruction for the weights and abscissas is used. The piecewise linear reconstruction is obtained using a minmod slope limiter [56]. For the i^{th} cell, this can be written as:

$$\begin{aligned} \mathbf{N}_{i-1/2,r}^n &= \mathbf{N}_i^n - \frac{\Delta x}{2} \partial \mathbf{N}_i, \\ \mathbf{N}_{i+1/2,l}^n &= \mathbf{N}_i^n + \frac{\Delta x}{2} \partial \mathbf{N}_i, \end{aligned} \quad (2.26)$$

where

$$\partial \mathbf{N}_i = \text{minmod} \left(\frac{\mathbf{N}_i^n - \mathbf{N}_{i-1}^n}{\Delta x}, \frac{\mathbf{N}_{i+1}^n - \mathbf{N}_i^n}{\Delta x} \right). \quad (2.27)$$

The minmod function is defined as:

$$\text{minmod}(x, y) = \text{sign}(x) \left(\frac{1 + \text{sign}(xy)}{2} \right) \min(|x|, |y|). \quad (2.28)$$

2.2.4.3 Third-order finite-volume scheme

In the 3rd-order finite-volume scheme, a piecewise parabolic reconstruction for the weights and abscissas is used. For the i^{th} cell, the reconstructed weights and abscissas can be written as:

$$\begin{aligned} \mathbf{N}_{i-1/2,r}^n &= \mathbf{N}_i^n - \left[\frac{1}{3}(\mathbf{N}_i^n - \mathbf{N}_{i-1}^n) + \frac{1}{6}(\mathbf{N}_{i+1}^n - \mathbf{N}_i^n) \right], \\ \mathbf{N}_{i+1/2,l}^n &= \mathbf{N}_i^n + \left[\frac{1}{6}(\mathbf{N}_i^n - \mathbf{N}_{i-1}^n) + \frac{1}{3}(\mathbf{N}_{i+1}^n - \mathbf{N}_i^n) \right]. \end{aligned} \quad (2.29)$$

The third-order MUSCL reconstruction without a limiter is the same as (2.29). However, in the case of a discontinuous solution a limiter is essential. A limited version of third-order MUSCL can be found in [56].

2.2.5 Solution algorithm

The finite-volume schemes presented in the above section are used to solve for the spatial transport part of the moment transport equations. However, the complete moment transport equations have collision and force terms as well. As mentioned earlier, these two terms are treated using an *operator-splitting* technique. A detailed solution algorithm involving all the terms can be found in [25, 35, 79]. Here a brief overview of the steps involved in the solution procedure is presented, assuming a single-stage explicit time-integration:

1. Initialize weights and abscissas in the domain.
2. Apply boundary conditions to weights and abscissas.
3. Compute moments using weights and abscissas.
4. Compute time-step size Δt .
5. Reconstruct weights and abscissas at cell faces.
6. Compute spatial flux terms at cell faces.
7. Advance moments by Δt due to spatial flux terms using a finite-volume approach.
8. Compute weights and abscissas from moments using the moment-inversion algorithm.
9. Advance weights by Δt due to force terms (drag and gravity).
10. Compute moments using weights and abscissas.
11. Advance moments by Δt due to collision terms.
12. Compute weights and abscissas from moments using the moment-inversion algorithm.
13. Apply boundary conditions to weights and abscissas.

14. Repeat steps (4) through (13) at each time step.

2.2.6 Non-realizability problem

At each time step, the weights and abscissas need to be recovered from the moments. The moment-inversion algorithm computes the set of weights and abscissas from the corresponding set of moments by solving a set of nonlinear equations. In the moment-inversion algorithm M^0 , M^1 , M^2 , M^3 are known and n_1 , n_2 , U_1 , U_2 are computed, by solving (2.17) in reverse direction using the product-difference (PD) algorithm [71, 121, 86]. However, the set of moments cannot be constituted by arbitrary values of each moment, but they have to conform to the definition of the *non-negative* number density function. The application of the PD algorithm to a set of realizable moments leads to a set of weights and abscissas that satisfy the properties of Gaussian quadrature. In particular the weights are always positive. During the development of the numerical schemes, which is the object of this work, a set of weights and abscissas will be said to represent realizable moments if weights are positive and abscissas lie in the interior of the support of f . Because of the non-linearity of the inversion problem, it is extremely difficult to determine in advance whether a given set of moments is realizable. However, Desjardins et al. [25] described how any finite-volume scheme that could guarantee non-negativity of the effective number density function will always keep the moments in realizable space.

The updated set of moments can be written as:

$$\mathbf{W}_i^{n+1} = \int \mathbf{K}h \, dv, \quad (2.30)$$

where

$$\begin{aligned} h &= f_i^n - \lambda \left(v^+ f_{i+1/2,l}^n + v^- f_{i+1/2,r}^n - v^+ f_{i-1/2,l}^n - v^- f_{i-1/2,r}^n \right) \\ &= f_i^n - \lambda v^+ f_{i+1/2,l}^n - \lambda v^- f_{i+1/2,r}^n + \lambda v^+ f_{i-1/2,l}^n + \lambda v^- f_{i-1/2,r}^n \end{aligned} \quad (2.31)$$

in which $\lambda = \Delta t / \Delta x$. In (2.31), h is the effective number density function and has different forms for different finite-volume schemes as the interface values are reconstructed in different ways. Desjardins et al. [25] stated that any finite-volume scheme that guarantees the non-negativity of h for all v , is realizable. Using this proposition, they derived the realizability criterion for the 1st-order finite-volume scheme. In the sections below, the realizability of the 1-D version of 1st-, 2nd- and high-order finite-volume schemes is discussed.

2.2.6.1 First-order finite-volume scheme

For the 1st-order finite-volume scheme (2.25) implies

$$f_{i-1/2,r}^n = f_i^n, \quad f_{i+1/2,l}^n = f_i^n. \quad (2.32)$$

Using this in (2.31), the effective number density function for the 1st-order finite-volume scheme can be written as:

$$h = (1 - \lambda|v|)f_i^n + \lambda v^+ f_{i-1}^n - \lambda v^- f_{i+1}^n. \quad (2.33)$$

As the moments at time level n are assumed to be realizable, the non-negativity of the number density function at time level n is guaranteed, i.e., $f_i^n \geq 0$, $f_{i-1}^n \geq 0$ and $f_{i+1}^n \geq 0$ for all v . Also, $v^+ \geq 0$ and $v^- \leq 0$. Hence, the non-negativity of h will be guaranteed if $(1 - \lambda|v|) \geq 0$. When written in terms of the abscissas, this condition becomes:

$$\lambda \leq \frac{1}{\max(|U_{i1}^n|, |U_{i2}^n|)}. \quad (2.34)$$

This is the realizability criterion for the first-order finite-volume scheme [25].

2.2.6.2 Second- & high-order finite-volume schemes

For the second-order and, in general, any high-order finite-volume scheme, the reconstructed values at the cell interfaces are different from the cell-averaged values. The equality of reconstructed values and cell-averaged values is a *special* property that holds only for the first-order finite-volume scheme. For second and high-order finite-volume schemes, the effective number density function h can be obtained from (2.31) by putting in the reconstructed values. An interesting thing to notice in (2.31) is that on the right-hand side, out of the five terms, only three are non-negative. The second and fifth terms are always non-positive. As was stated in [25], realizability can only be guaranteed if the effective number density function is non-negative for all velocities. Clearly this does not hold, in general, for second and high-order finite-volume schemes. Hence, realizability cannot be guaranteed for any finite-volume scheme other than first-order.

2.3 Improved realizable finite-volume schemes

2.3.1 Basic idea

As was stated earlier, the two non-positive terms on the right-hand side of (2.31) might lead to non-realizability problems. The non-negative terms present a physical view of the number density function. An important thing to notice is that, despite the presence of the two non-positive terms, the first-order finite-volume scheme is still realizable under the restriction of a realizability criterion. This is possible because in the first-order finite-volume scheme, the interface values are the same as the cell-averaged values ($f_i^n = f_{i+1/2,l}^n = f_{i-1/2,r}^n$), thereby allowing a grouping of the first term with the two non-positive terms on right-hand side of (2.31). This idea of grouping the terms is essential to the realizability of the first-order finite-volume scheme and it also forms the basis of the development of new improved realizable finite-volume schemes.

For high-order finite-volume schemes, in general:

$$\mathbf{N}_i^n \neq \mathbf{N}_{i+1/2,l}^n \neq \mathbf{N}_{i-1/2,r}^n, \quad (2.35)$$

i.e.

$$n_{i,\alpha}^n \neq n_{i+1/2,\alpha,l}^n \neq n_{i-1/2,\alpha,r}^n \quad \text{and} \quad U_{i,\alpha}^n \neq U_{i+1/2,\alpha,l}^n \neq U_{i-1/2,\alpha,r}^n. \quad (2.36)$$

Consider a special reconstruction where

$$n_{i,\alpha}^n \neq n_{i+1/2,\alpha,l}^n \neq n_{i-1/2,\alpha,r}^n \quad \text{and} \quad U_{i,\alpha}^n = U_{i+1/2,\alpha,l}^n = U_{i-1/2,\alpha,r}^n. \quad (2.37)$$

For this special reconstruction, realizability can always be guaranteed with a suitable constraint on the time-step size. This is the subject of the following theorem.

Theorem 1. *Let $\beta, p \in \mathbb{N}$ and $\alpha \in \{1, 2, \dots, \beta\}$. Also let the cell-averaged and reconstructed values of the weights satisfy $n_{i,\alpha}^n > 0$ and $n_{i+1/2,\alpha,l}^n, n_{i-1/2,\alpha,r}^n \geq 0 \forall \alpha$. If a finite-volume scheme using a single-stage Euler explicit time-integration scheme is devised that uses a p^{th} -order reconstruction for weights and 1^{st} -order reconstruction for abscissas, the non-negativity of the effective number density function (2.31) in the i^{th} cell can always be guaranteed under an explicit constraint on time-step size ($\Delta t \in \mathbb{R}^+$).*

Proof. Using (2.31), the effective number density function, regardless of the finite-volume scheme used, can be written as:

$$h = f_i^n - \lambda v^+ f_{i+1/2,l}^n + \lambda v^- f_{i-1/2,r}^n + \xi^+. \quad (2.38)$$

In the above expression, the first non-negative term and the two non-positive terms have been represented explicitly. The other two terms are always non-negative and have been grouped under ξ^+ . For a β -node quadrature, using (2.9), the expression for h becomes:

$$\begin{aligned} h = \sum_{\alpha=1}^{\beta} [& n_{i,\alpha}^n \delta(v - U_{i,\alpha}^n) - \lambda v^+ n_{i+1/2,\alpha,l}^n \delta(v - U_{i+1/2,\alpha,l}^n) \\ & + \lambda v^- n_{i-1/2,\alpha,r}^n \delta(v - U_{i-1/2,\alpha,r}^n)] \\ & + \xi^+. \end{aligned} \quad (2.39)$$

If a first-order reconstruction is used for the abscissas, then the interface values of the abscissas will be the same as the cell-averaged values:

$$U_{i,\alpha}^n = U_{i+1/2,\alpha,l}^n = U_{i-1/2,\alpha,r}^n. \quad (2.40)$$

Putting this in (2.39), the effective number density function becomes:

$$h = \sum_{\alpha=1}^{\beta} \{ n_{i,\alpha}^n - \lambda v^+ n_{i+1/2,\alpha,l}^n + \lambda v^- n_{i-1/2,\alpha,r}^n \} \delta(v - U_{i,\alpha}^n) + \xi^+. \quad (2.41)$$

For $\Delta t \in \mathbb{R}^+$ satisfying the condition:

$$\lambda = \min_{\alpha \in \{1,2,\dots,\beta\}} \left(\frac{n_{i,\alpha}^n}{n_{i+1/2,\alpha,l}^n \max(U_{i,\alpha}^n, 0) - n_{i-1/2,\alpha,r}^n \min(U_{i,\alpha}^n, 0)} \right), \quad (2.42)$$

h is non-negative for all v . This concludes the proof. \square

Clearly, Theorem 1 guarantees the realizability of the special reconstruction in (2.37), for all cases except for the one where $n_{i,\alpha}^n = 0$. However this case turns out to be trivial if a minmod limiter is used to limit the reconstructed values. A minmod limiter guarantees that whenever $n_{i,\alpha}^n = 0$, then $n_{i+1/2,\alpha,l}^n = n_{i-1/2,\alpha,r}^n = 0$, thereby automatically dropping the two non-positive terms in (2.39). For $p = 1$, (2.42) reduces to the same realizability criterion as in (2.34):

$$\lambda = \min_{\alpha \in \{1,2,\dots,\beta\}} \left(\frac{1}{|U_{i,\alpha}^n|} \right). \quad (2.43)$$

This new reconstruction uses a high-order reconstruction for the weights, but a first-order reconstruction for the abscissas. To remove the ambiguity, it is worth clarifying that all the finite-volume schemes discussed earlier, in which the same order of reconstruction was used for the weights and abscissas will be termed *standard* finite-volume schemes. For example, a *standard* second-order finite-volume scheme is the one discussed in Sec. 2.2.4.2, where a second-order reconstruction is used for both the weights and abscissas. More generally, a *standard* p^{th} -order finite-volume scheme uses a p^{th} -order reconstruction for both the weights and abscissas. It is worth reiterating that the realizability of the *standard* p^{th} -order finite-volume scheme is not guaranteed. Corresponding to the *standard* p^{th} -order finite-volume scheme another scheme can be developed based on the special reconstruction discussed above. This new scheme will use p^{th} -order reconstruction for the weights and 1st-order reconstruction for the abscissas. Realizability of this new scheme is guaranteed by the constraint, also known as realizability criterion, in (2.42). Because a 1st-order reconstruction is used for the abscissas, the new scheme is less accurate than the *standard* p^{th} -order finite-volume scheme and henceforth will be termed a *quasi- p^{th}* -order finite-volume scheme. The *standard* 1st-order finite-volume scheme and the *quasi-1st*-order finite-volume scheme are the same and will be simply referred to as the 1st-order finite-volume scheme.

Two important facts about the new schemes are: (i) they are better than first-order finite-volume schemes as far as accuracy is concerned and (ii) realizability is guaranteed under the realizability criterion that has an explicit form. This marks a significant improvement in solution methods for quadrature-based moment methods. Over the years, many high-order finite-volume schemes have been developed [113, 21, 60, 118, 119, 4, 5, 120] for convection-dominated problems in the field of fluid dynamics. However, quadrature-based moment methods have not benefited from these high-order schemes because of the non-realizability limitation. However, with the new approach, all the already existing knowledge about high-order finite-volume schemes can now be utilized for solutions using quadrature-based moment methods.

In general, the new *quasi- p^{th}* -order realizable finite-volume scheme will be less accurate compared to the *standard* p^{th} -order finite-volume scheme but for the problems where the velocities are constant over a range of cells, the difference in accuracy will be negligible. This

fact is further demonstrated in Sec. 2.5. Next the realizability criterion for different dimensions is presented, and we explain the way in which it is applied. In the appendix to this chapter, we show how *quasi-p*th-order finite-volume schemes can also be written for the advection of *velocity-independent* density functions.

2.3.2 Realizability criterion for 1-D cases

The relation given in (2.42) is the realizability criterion for 1-D problems. It can also be written as:

$$\{n_{i,\alpha}^n - \lambda \max(U_{i\alpha}, 0)n_{i+1/2,\alpha,l}^n + \lambda \min(U_{i\alpha}, 0)n_{i-1/2,\alpha,r}^n\} \geq 0 \quad \forall \alpha \in \{1, 2, \dots, \beta\}. \quad (2.44)$$

This simple realizability criterion can be used for the calculation of λ and hence Δt for 1-D cases with β -node quadrature.

2.3.3 Realizability criterion for 2-D/3-D cases

In (2.44), $[\max(U_{i\alpha}, 0)n_{i+1/2,\alpha,l}^n - \min(U_{i\alpha}, 0)n_{i-1/2,\alpha,r}^n]$ is the total outgoing flux from the i^{th} cell for the α^{th} weight. Hence, (2.44) can also be written as:

$$\{n_{i,\alpha}^n - \lambda \sum \text{Outgoing_Flux}_{i,\alpha}^n\} \geq 0 \quad \forall \alpha \in \{1, 2, \dots, \beta\}, \quad (2.45)$$

where the summation is over the faces of the i^{th} cell. This form of the realizability criterion can be used for 2-D and 3-D cases. Although (2.45) was obtained using an analogy from (2.44), it can be derived directly from the expression for finite-volume scheme in 2-D or 3-D.

Consider a 3-D case. Let Ω_i and $\partial\Omega_i$ denote the i^{th} cell and its boundary respectively. Also let $e \in \partial\Omega_i$ be a face of the i^{th} cell, A_e be its area and $\hat{\mathbf{n}}_e = [n_{e,x} \ n_{e,y} \ n_{e,z}]$ be the outward unit normal at this face. The finite-volume expression for the single-stage Euler explicit time-integration, analogous to (2.20) can be written as:

$$\mathbf{W}_i^{n+1} = \mathbf{W}_i^n - \frac{\Delta t}{|\Omega_i|} \sum_{e \in \partial\Omega_i} \{\mathbf{G}(\mathbf{W}_{e,l}^n, \mathbf{W}_{e,r}^n, \hat{\mathbf{n}}_e) A_e\}, \quad (2.46)$$

where $|\Omega_i|$ denotes the volume of the i^{th} cell and $\mathbf{W}_{e,l}^n$ and $\mathbf{W}_{e,r}^n$ represent the reconstructed value of \mathbf{W} on the left and right sides of face e . The outward normal vector $\hat{\mathbf{n}}_e$ defined above,

points from the left side to the right side of face e . The form of \mathbf{W} analogous to the one in (2.18) is:

$$\mathbf{W} = \int \mathbf{K}(u, v, w) f(u, v, w) du dv dw. \quad (2.47)$$

The numerical flux function can be written as:

$$\mathbf{G}(\mathbf{W}_{e,l}^n, \mathbf{W}_{e,r}^n, \hat{\mathbf{n}}_e) = \int v_n^+ \mathbf{K} f_{e,l} du dv dw + \int v_n^- \mathbf{K} f_{e,r} du dv dw, \quad (2.48)$$

where

$$\begin{aligned} v_n^+ &= \max(n_{e,x}u + n_{e,y}v + n_{e,z}w, 0), \\ v_n^- &= \min(n_{e,x}u + n_{e,y}v + n_{e,z}w, 0). \end{aligned} \quad (2.49)$$

Substituting (2.47) and (2.48) in (2.46), the effective number density can be written as:

$$h = f_i^n - \lambda \sum_{e \in \partial\Omega_i} (v_n^+ f_{e,l} A_e + v_n^- f_{e,r} A_e). \quad (2.50)$$

In (2.50), $\lambda = \Delta t / |\Omega_i|$. For β -node quadrature, f has the same form as in (2.9). Using (2.9) and the special reconstruction $\mathbf{U}_{e,\alpha,l}^n = \mathbf{U}_{e,\alpha,r}^n = \mathbf{U}_{i,\alpha}^n$, h can be further written as:

$$\begin{aligned} h &= \sum_{\alpha=1}^{\beta} \left\{ n_{i,\alpha}^n - \lambda \sum_{e \in \partial\Omega_i} (v_n^+ n_{e,\alpha,l}^n A_e + v_n^- n_{e,\alpha,r}^n A_e) \right\} \delta(\mathbf{v} - \mathbf{U}_{i,\alpha}^n) \\ &= \sum_{\alpha=1}^{\beta} \left\{ n_{i,\alpha}^n - \lambda \sum_{e \in \partial\Omega_i} (v_n^+ n_{e,\alpha,l}^n A_e) \right\} \delta(\mathbf{v} - \mathbf{U}_{i,\alpha}^n) + \xi^+, \end{aligned} \quad (2.51)$$

where again all the non-negative terms except for the first one have been grouped under ξ^+ .

Non-negativity of h can be guaranteed if:

$$\left\{ n_{i,\alpha}^n - \lambda \sum_{e \in \partial I} (v_n^+ n_{e,\alpha,l}^n A_e) \right\} \geq 0 \quad \forall \alpha \in \{1, 2, \dots, \beta\}. \quad (2.52)$$

This is exactly the same as (2.45). It is worth reiterating that the summation in (2.45) and (2.52) is for the outgoing fluxes only. Hence, for calculating these fluxes only the reconstructed weights on the interior sides (side towards the i^{th} cell) of faces should be used, the ones on the opposite side should be set to zero, i.e., the flux coming in from neighboring cells should not be accounted for. Consider a simple 2-D Cartesian case shown in Figure 2.1. For the sake of simplicity, subscript α and superscript n will be dropped and only 1-node quadrature will be demonstrated. The cell in the center, Ω_0 , has four neighbors – $\Omega_1, \Omega_2, \Omega_3, \Omega_4$ – and the

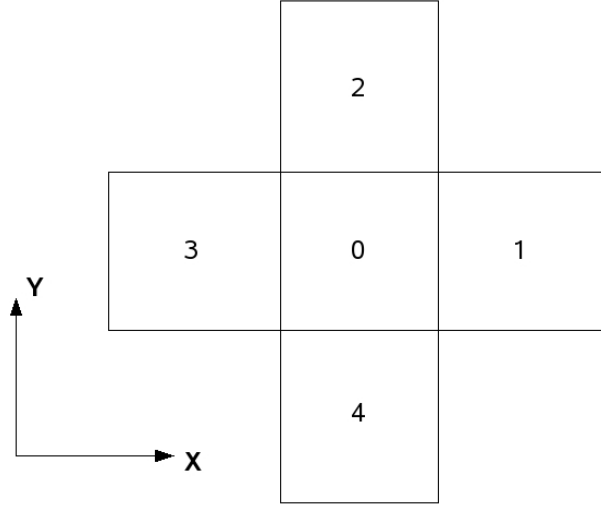


Figure 2.1 Cells with faces aligned along Cartesian axes.

reconstructed values of the weights on inner sides of the corresponding faces are n_{01} , n_{02} , n_{03} , n_{04} , respectively. The cell-averaged weight for $cell_0$ is n_0 and the corresponding X -direction and Y -direction abscissas are U_0 and V_0 , respectively. The realizability condition for Ω_0 can be written as:

$$\{n_0 - \lambda[n_{01}A_1 \max(U_0, 0) + n_{02}A_2 \max(V_0, 0) - n_{03}A_3 \min(U_0, 0) - n_{04}A_4 \min(V_0, 0)]\} \geq 0, \quad (2.53)$$

where A_1 , A_2 , A_3 , A_4 are the areas of the four faces. In (2.53), $\lambda = \Delta t/|\Omega_0|$.

All the analysis to this point has been done for a number density function that depends on the velocity. However, many population balance models involve density functions that do not depend on velocity. For such cases, each moment can be advected independently using a first-order finite-volume scheme without violating realizability of the moment set. On the other hand, the use of any high-order finite-volume scheme may lead to unphysical or non-realizable moment sets [85, 72, 73, 124]. As demonstrated in the appendix to this chapter, this problem can be avoided if QMOM is used with the *quasi-p*th-order finite-volume schemes described above.

Before moving onto the next section, here is a brief discussion on the Courant-Friedrichs-Lewy (CFL) criterion vs. the realizability criterion. The realizability criterion is analogous

to a CFL criterion. However, their purposes are different. A CFL criterion guarantees the stability of the solution while the realizability criterion guarantees the physical nature of the solution. An explicit form of the CFL criterion exists only for 1-D cases, which is equivalent to the realizability criterion. For 2-D and 3-D problems, there is no explicit form for the CFL criterion. However, there exists an explicit form for the realizability criterion even for 2-D and 3-D cases as shown above. It also turns out from numerical experiments that the realizability criterion is a more strict constraint on Δt as compared to the CFL criterion. Also the realizability criterion corresponding to a p^{th} -order ($p > 1$) finite-volume scheme is in general stricter than the one for the 1st-order finite-volume scheme.

2.4 Multi-stage time-integration

For simplicity, all the previous sections employed single-stage Euler explicit time-integration. However, single-stage Euler explicit time-integration is only first-order accurate in time. To improve time-accuracy, multi-stage explicit time-integration schemes are used in practice. Nevertheless, not all multi-stage time-integration schemes guarantee realizability. Here, two different time-integration schemes are presented: RK2 and RK2SSP [42]. The former is the standard 2nd-order two-stage Runge-Kutta scheme, while the latter is the 2nd-order two-stage strong-stability-preserving (SSP) Runge-Kutta scheme.

2.4.1 RK2 scheme

The standard 2nd-order two-stage Runge-Kutta scheme can be written as:

$$\mathbf{W}_i^* = \mathbf{W}_i^n - \frac{\Delta t}{2\Delta x} \left[\mathbf{G} \left(\mathbf{W}_{i+1/2,l}^n, \mathbf{W}_{i+1/2,r}^n \right) - \mathbf{G} \left(\mathbf{W}_{i-1/2,l}^n, \mathbf{W}_{i-1/2,r}^n \right) \right], \quad (2.54)$$

$$\mathbf{W}_i^{n+1} = \mathbf{W}_i^n - \frac{\Delta t}{\Delta x} \left[\mathbf{G} \left(\mathbf{W}_{i+1/2,l}^*, \mathbf{W}_{i+1/2,r}^* \right) - \mathbf{G} \left(\mathbf{W}_{i-1/2,l}^*, \mathbf{W}_{i-1/2,r}^* \right) \right]. \quad (2.55)$$

2.4.1.1 First stage

The first stage is the same as the single-stage Euler explicit time-integration scheme, the only difference being the factor of (1/2) in $\frac{\Delta t}{2\Delta x}$. If $\lambda = \frac{\Delta t}{2\Delta x}$, realizability can be guaranteed for 1st-order and *quasi-p*th-order finite-volume schemes subject to condition (2.42).

2.4.1.2 Second stage

The set of moments for the i^{th} cell after the second stage can be written as:

$$\mathbf{W}_i^{n+1} = \int \mathbf{K} h^{n+1} dv, \quad (2.56)$$

where

$$\begin{aligned} h_i^{n+1} &= f_i^n - \lambda \left(v^+ f_{i+1/2,l}^* + v^- f_{i+1/2,r}^* - v^+ f_{i-1/2,l}^* - v^- f_{i-1/2,r}^* \right) \\ &= f_i^n - \lambda v^+ f_{i+1/2,l}^* - \lambda v^- f_{i+1/2,r}^* + \lambda v^+ f_{i-1/2,l}^* + \lambda v^- f_{i-1/2,r}^* \\ &= f_i^n - \lambda v^+ f_{i+1/2,l}^* + \lambda v^- f_{i-1/2,r}^* + \xi^+, \end{aligned} \quad (2.57)$$

in which $\lambda = \Delta t / \Delta x$. For the 1st-order and *quasi-p*th-order finite-volume schemes:

$$U_{i+1/2,\alpha,l}^* = U_{i-1/2,\alpha,r}^*, \quad (2.58)$$

but in general

$$U_{i,\alpha}^n \neq U_{i+1/2,\alpha,l}^* \quad \text{and} \quad U_{i,\alpha}^n \neq U_{i-1/2,\alpha,r}^*. \quad (2.59)$$

Hence, grouping of terms is not possible and realizability cannot be guaranteed for the second stage.

The RK2 scheme does not guarantee realizability of the moment set.

2.4.2 RK2SSP scheme

The 2nd-order two-stage strong stability-preserving Runge-Kutta scheme can be written as:

$$\mathbf{W}_i^* = \mathbf{W}_i^n - \frac{\Delta t}{\Delta x} \left[\mathbf{G} \left(\mathbf{W}_{i+1/2,l}^n, \mathbf{W}_{i+1/2,r}^n \right) - \mathbf{G} \left(\mathbf{W}_{i-1/2,l}^n, \mathbf{W}_{i-1/2,r}^n \right) \right], \quad (2.60)$$

$$\mathbf{W}_i^{n+1} = \frac{1}{2} \left[\mathbf{W}_i^n + \mathbf{W}_i^* - \frac{\Delta t}{\Delta x} \left\{ \mathbf{G} \left(\mathbf{W}_{i+1/2,l}^*, \mathbf{W}_{i+1/2,r}^* \right) - \mathbf{G} \left(\mathbf{W}_{i-1/2,l}^*, \mathbf{W}_{i-1/2,r}^* \right) \right\} \right]. \quad (2.61)$$

2.4.2.1 First stage

The first stage is exactly the same as the single-stage Euler explicit time-integration scheme and realizability can be guaranteed for 1st-order and *quasi-p*th-order finite-volume schemes subject to condition (2.42).

2.4.2.2 Second stage

The set of moments for the i^{th} cell after the second stage can be written as:

$$\mathbf{W}_i^{n+1} = \int \mathbf{K} h_i^{n+1} dv, \quad (2.62)$$

where

$$\begin{aligned} h_i^{n+1} &= \frac{1}{2} \left[f_i^n + f_i^* - \lambda \left(v^+ f_{i+1/2,l}^* + v^- f_{i+1/2,r}^* - v^+ f_{i-1/2,l}^* - v^- f_{i-1/2,r}^* \right) \right] \\ &= \frac{1}{2} \left[f_i^n + f_i^* - \lambda v^+ f_{i+1/2,l}^* - \lambda v^- f_{i+1/2,r}^* + \lambda v^+ f_{i-1/2,l}^* + \lambda v^- f_{i-1/2,r}^* \right] \\ &= \frac{1}{2} \left[f_i^n + f_i^* - \lambda v^+ f_{i+1/2,l}^* + \lambda v^- f_{i-1/2,r}^* \right] + \xi^+ \\ &= \frac{1}{2} \left[f_i^* - \lambda v^+ f_{i+1/2,l}^* + \lambda v^- f_{i-1/2,r}^* \right] + \psi^+, \end{aligned} \quad (2.63)$$

in which $\lambda = \Delta t / \Delta x$ and $\psi^+ = \xi^+ + \frac{1}{2} f_i^n$. For the 1st-order and *quasi-p*th-order finite-volume schemes, grouping of the first three terms is possible because

$$U_{i,\alpha}^* = U_{i+1/2,\alpha,l}^* = U_{i-1/2,\alpha,r}^*. \quad (2.64)$$

After grouping:

$$h_i^{n+1} = \sum_{\alpha=1}^{\beta} \{ n_{i,\alpha}^* - \lambda v^+ n_{i+1/2,\alpha,l}^* + \lambda v^- n_{i-1/2,\alpha,r}^* \} \delta(v - U_{i,\alpha}^*) + \psi^+. \quad (2.65)$$

This is exactly the same form as in (2.42) with the superscript n replaced by $*$. Hence, the realizability condition can be guaranteed using (2.42), by replacing superscript n with $*$.

The RK2SSP scheme, combined with *quasi-p*th-order finite-volume schemes, guarantees realizability of the moment set.

2.4.2.3 Alternate form

Another way to write RK2SPP is:

$$\begin{aligned} \mathbf{W}_i^{(0)} &= \mathbf{W}_i^n, \\ \mathbf{W}_i^{(1)} &= \mathbf{W}_i^{(0)} - \frac{\Delta t}{\Delta x} \left[\mathbf{G} \left(\mathbf{W}_{i+1/2,l}^{(0)}, \mathbf{W}_{i+1/2,r}^{(0)} \right) - \mathbf{G} \left(\mathbf{W}_{i-1/2,l}^{(0)}, \mathbf{W}_{i-1/2,r}^{(0)} \right) \right], \\ \mathbf{W}_i^{(2)} &= \mathbf{W}_i^{(1)} - \frac{\Delta t}{\Delta x} \left[\mathbf{G} \left(\mathbf{W}_{i+1/2,l}^{(1)}, \mathbf{W}_{i+1/2,r}^{(1)} \right) - \mathbf{G} \left(\mathbf{W}_{i-1/2,l}^{(1)}, \mathbf{W}_{i-1/2,r}^{(1)} \right) \right], \\ \mathbf{W}_i^{n+1} &= \frac{1}{2} \left[\mathbf{W}_i^{(0)} + \mathbf{W}_i^{(2)} \right]. \end{aligned} \quad (2.66)$$

This form is more amenable to using an operator-splitting technique for the collision and drag terms.

2.4.3 Calculation of time-step size

The global time-step size (Δt) should satisfy both the CFL and realizability criteria to guarantee stability and physical nature preservation. Usually, the largest value of CFL $\sim O(1)$ that gives a stable solution is used as a CFL criterion for all 1-D/2-D/3-D cases. The definition of the CFL varies, but a general form is:

$$\text{CFL} = \Delta t \left(\frac{\text{cell velocity magnitude}}{\text{cell length scale}} \right). \quad (2.67)$$

Let $\Delta t_{\text{CFL},i}$ and $\Delta t_{\text{realizable},i}$ be the time-step sizes in the i^{th} cell satisfying the CFL and realizability criteria, respectively. An obvious way to calculate global time-step size is:

$$\Delta t = \min_i (\Delta t_{\text{CFL},i}, \Delta t_{\text{realizable},i}). \quad (2.68)$$

However, in the present paper a slightly different approach is used for the calculation of Δt .

As stated earlier, in general $\Delta t_{\text{realizable},i} < \Delta t_{\text{CFL},i}$. This implies that most of the time $\Delta t = \min_i (\Delta t_{\text{realizable},i})$. To have a better time accuracy, a multi-stage time-integration is used. For a multi-stage time-integration, Δt calculated for the 1st-stage is used in all the later stages. But $\min_i (\Delta t_{\text{realizable},i})$ may be different for different stages of time integration and in that case Δt calculated for the 1st-stage will not satisfy the realizability criterion for a later stage. In order to get rid of this problem, the following approach is used. Suppose, the problem under consideration uses a *quasi-p*th-order finite-volume scheme. A value of the CFL $\sim O(1)$ is pre-specified and Δt is calculated as $\Delta t = \min_i (\Delta t_{\text{CFL},i})$. During each stage of time integration, this Δt is used as the global time-step size, and the realizability condition corresponding to *quasi-p*th-order finite-volume scheme is checked in each cell. For the cells in which the check succeeds, a *quasi-p*th-order reconstruction is used for the weights. And for the cells in which the check fails, a 1st-order reconstruction is used for the weights. Thereafter, in the failed cells, the realizability criterion corresponding to 1st-order finite-volume scheme is checked. This check succeeds on almost all occasions if the CFL is not very large, thereby satisfying the realizability criterion in each cell. However, if the last check fails, the whole process is re-initiated using a smaller CFL.

2.5 Numerical results

In this section several results are presented for 1-D and 2-D cases. For all the cases a 2nd-order RK2SSP scheme is used for time-integration and Δt is calculated using CFL = 0.5 unless otherwise stated. Periodic boundary conditions are used for all 1-D cases while for the 2-D cases a combination of wall, Dirichlet and periodic boundary conditions is used. The domain for the 1-D cases is defined by $x \in [-1, 1]$. The simulations consider either the spatial flux terms alone or in combination with fluid drag terms. Collisions are not included. The drag force is calculated using (2.5) and the abscissas are updated using simple kinematic relations. More details can be found in [33, 34, 35]. The drag terms are dependent on the Stokes number defined by

$$\text{St} = \frac{1}{18} \frac{\rho_p d_p^2}{\mu_g}. \quad (2.69)$$

For the two cases presented here that include the drag terms, $\text{St} = 1$ is used.

For the 1-D cases, the numerical results using the *quasi*-2nd-order and *quasi*-3rd-order schemes are presented. For the *quasi*-2nd-order scheme, a linear reconstruction with the minmod limiter as described in Sec. 2.2.4.2 is used while for the *quasi*-3rd-order scheme a MUSCL technique [113, 56] is used. For the 2-D cases, results using the *quasi*-2nd-order scheme are presented. A second-order least-squares reconstruction [118, 4] is used for the weights using neighboring cell-averaged values. Moreover, a limiter [118, 4, 39] is applied to the least-squares reconstruction to avoid spurious oscillations. The results for the *standard* 2nd-order scheme are presented only for the simplest 1-D cases with constant abscissas because of the non-realizability problem. In all the cases, the mean density is computed using $\sum n_\alpha$ and the mean velocity is computed with $\sum(n_\alpha u_\alpha) / \sum n_\alpha$.

2.5.1 Spatial accuracy study

It was stated earlier that although in general the new *quasi* schemes have lower spatial accuracy compared to *standard* schemes, for problems where the velocities are constant over a range of cells, both schemes have almost the same order of spatial accuracy. Here, the order of spatial accuracy of the *standard* and the new *quasi* schemes is discussed for cases where the

abscissas are constant over a range of cells. Results in this section are based on simple 1-D cases for which analytical solutions exist. L_1 errors are calculated by comparing the numerical solution with the analytical solution for mean density. L_1 errors and order of convergence are presented for four schemes: 1st-order, *standard* 2nd-order, *quasi*-2nd-order, *quasi*-3rd-order. Tables 2.1 and 2.2 show the results for 1-node and 2-node quadrature, respectively. For both cases $\Delta t = 0.001$ is used. For 1-node quadrature, the initial weight (n) and abscissa (U) are given as:

$$n = 1.0 + \sin(\pi x), \quad U = 1. \quad (2.70)$$

For 2-node quadrature, initial weights (n_1, n_2) and abscissas (U_1, U_2) are given as:

$$\begin{aligned} n_1 &= |\sin(\pi x)|, \quad n_2 = 0, \quad U_1 = 1, \quad U_2 = 0 \quad \text{for } x \in [-1, 0), \\ n_1 &= 0, \quad n_2 = |\sin(\pi x)|, \quad U_1 = 0, \quad U_2 = -1 \quad \text{for } x \in [0, 1]. \end{aligned} \quad (2.71)$$

For 1-node quadrature, errors are calculated at $t = 4$, while for 2-node quadrature errors are calculated at $t = 1$. It is observed that the formal order of accuracy can be obtained for 1-node quadrature, but as the number of quadrature nodes is increased, the order of accuracy for all schemes decreases. Although the reason for this loss of order of accuracy has not been studied extensively, it can be attributed to the combined effects of an increase in the number of equations and use of the moment-inversion algorithm for ill-conditioned points. At many points the values of the weights are very small and the non-linear equations solved using the moment-inversion algorithm are often ill-conditioned for these points in the case of multiple quadrature nodes. It can also be observed that the *quasi*-2nd-order scheme always has approximately the same order of convergence as the *standard* 2nd-order scheme, and the *quasi*-3rd-order scheme is better compared to both.

2.5.2 Grid convergence study

Grid convergence studies for the *quasi*-2nd-order and *quasi*-3rd-order schemes in 1-D are presented in Figure 2.2. For both the schemes, the mean density obtained using different grid resolutions is compared with the analytical solution. Four different uniform grids have been considered with the number of cells equal to 25, 50, 100, 200. The comparisons have been

Table 2.1 L_1 error and order of accuracy of schemes using 1-node quadrature.

Grid Size	L_1 Error	Order
<i>1st-order scheme</i>		
25	0.504533	-
50	0.347427	0.54
100	0.207609	0.74
200	0.114032	0.86
<i>standard 2nd-order scheme</i>		
25	0.133869	-
50	0.055688	1.27
100	0.016926	1.72
200	0.004903	1.79
<i>quasi-2nd-order scheme</i>		
25	0.133869	-
50	0.055688	1.27
100	0.016926	1.72
200	0.004903	1.79
<i>quasi-3rd-order scheme (without limiter)</i>		
25	0.010411	-
50	0.001318	2.98
100	0.000165	2.99
200	0.000024	2.77
<i>quasi-3rd-order scheme</i>		
25	0.019774	-
50	0.004261	2.21
100	0.000885	2.27
200	0.000180	2.30

Table 2.2 L_1 error and order of accuracy of schemes using 2-node quadrature.

Grid Size	L_1 Error	Order
1 st -order scheme		
25	0.210375	-
50	0.148604	0.50
100	0.091184	0.70
200	0.051804	0.82
<i>standard</i> 2 nd -order scheme		
25	0.071737	-
50	0.028923	1.31
100	0.011792	1.29
200	0.004584	1.36
<i>quasi</i> -2 nd -order scheme		
25	0.071198	-
50	0.028921	1.30
100	0.011793	1.29
200	0.004584	1.36
<i>quasi</i> -3 rd -order scheme		
25	0.022921	-
50	0.009345	1.29
100	0.002946	1.67
200	0.000990	1.57

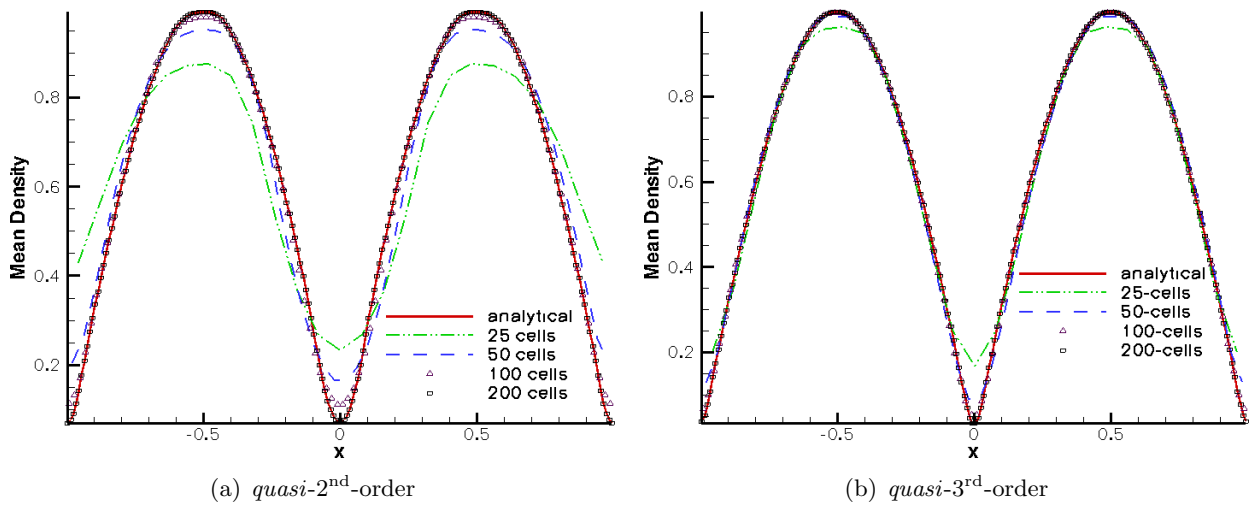
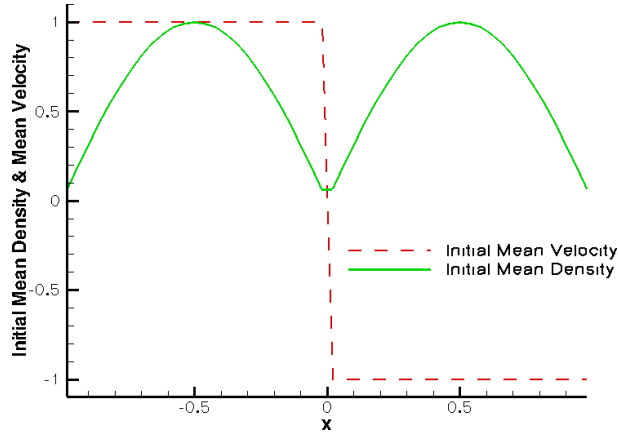
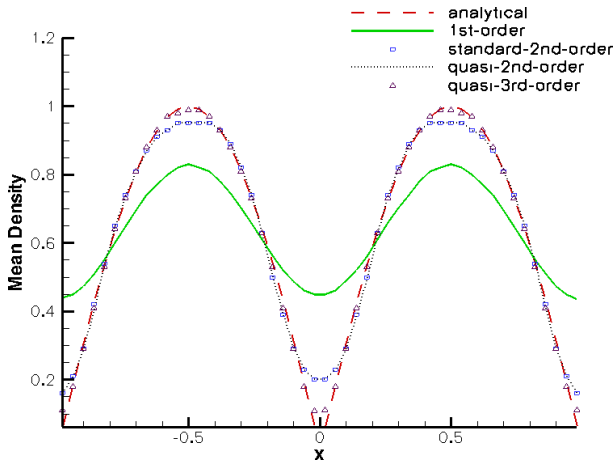


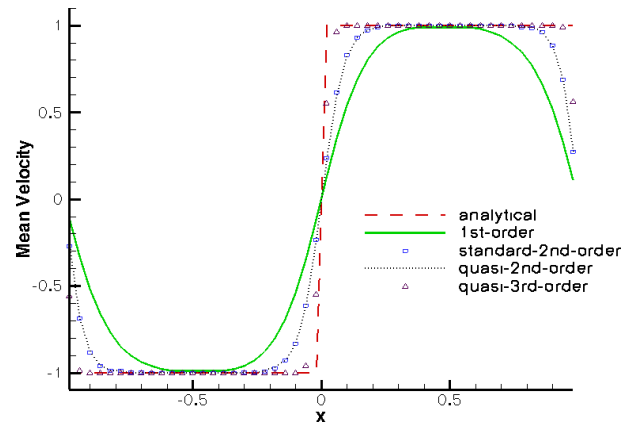
Figure 2.2 Grid convergence study for different schemes.



(a) Initial mean density and velocity



(b) Final mean density



(c) Final mean velocity

Figure 2.3 Comparison of schemes for 1-D case with only convection terms.

done for a 2-node quadrature case with the same initializations as in (2.71). Figures 2.2(a) and 2.2(b) show grid convergence for the *quasi-2nd*-order and *quasi-3rd*-order schemes, respectively. As the number of grid cells is increased, the solutions using both schemes converge towards the analytical solution.

2.5.3 Comparison of schemes for 1-D case with only convection terms

For this case, 2-node quadrature is used with the weights being sinusoidal functions and the abscissas being square functions. 50 grid points are used and the results are shown in Figure 2.3. The initial ($t = 0$) conditions are same as in (2.71) and are shown in Figure 2.3(a). Figures

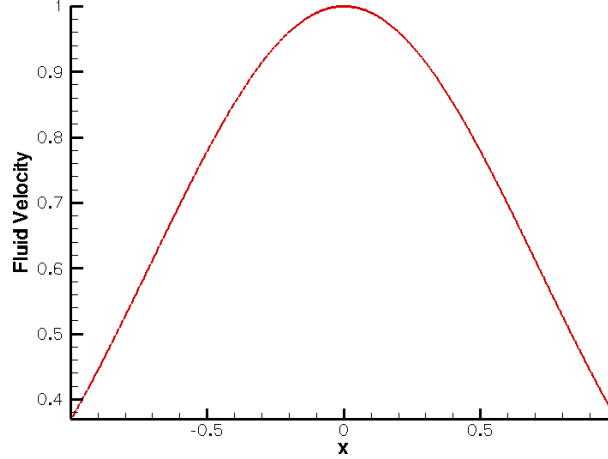


Figure 2.4 Fluid velocity for 1-D case.

2.3(b) and 2.3(c) show the final conditions for the mean density and mean velocity, respectively ($t = 1$). The weight distribution is symmetric about $x = 0$, with the left wave moving towards the right (negative abscissa) and the right wave moving towards the left (positive abscissa). The final time has been chosen such that the waves coalesce at $x = 0$ and then separate again. Four different schemes have been compared: 1st-order, *standard* 2nd-order, *quasi*-2nd-order, *quasi*-3rd-order. The *standard* 2nd-order and *quasi*-2nd-order results are on top of each other. The *quasi*-3rd-order scheme shows an improvement over the *quasi*-2nd-order scheme.

2.5.4 Comparison of schemes for 1-D case with both convection and drag terms

For this case, 4-node quadrature is used. Initial conditions ($t = 0$) for $x \in [-0.8, -0.7]$ are given as:

$$\begin{aligned} n_1 = n_2 = n_3 = n_4 &= \sin(10\pi(x + 0.8)), \\ U_1 = U_2 = U_3 = U_4 &= 0. \end{aligned} \tag{2.72}$$

Everywhere else both the weights and abscissas are zero. The particle flow is driven by fluid drag. The fluid velocity is given by

$$U_g = e^{-x^2}, \tag{2.73}$$

and is shown in Figure 2.4. The QMOM results using three schemes – 1st-order, *quasi*-2nd-order, *quasi*-3rd-order – are compared with the Lagrangian results. The results for the mean density are presented at four different times in Figure 2.5. The *quasi*-3rd-order and *quasi*-2nd-

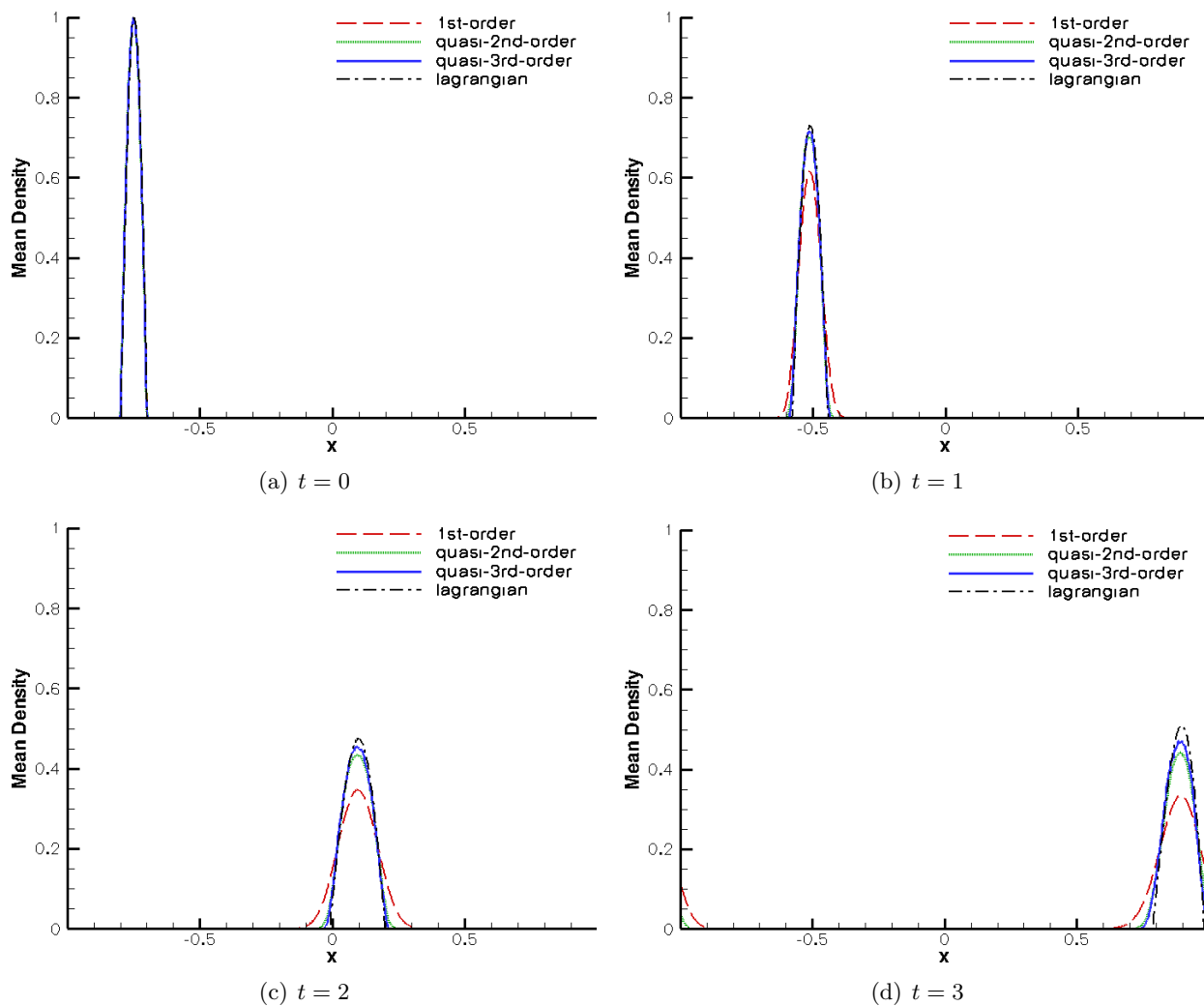


Figure 2.5 Comparison of schemes using mean density for 1-D case with convection and drag terms.

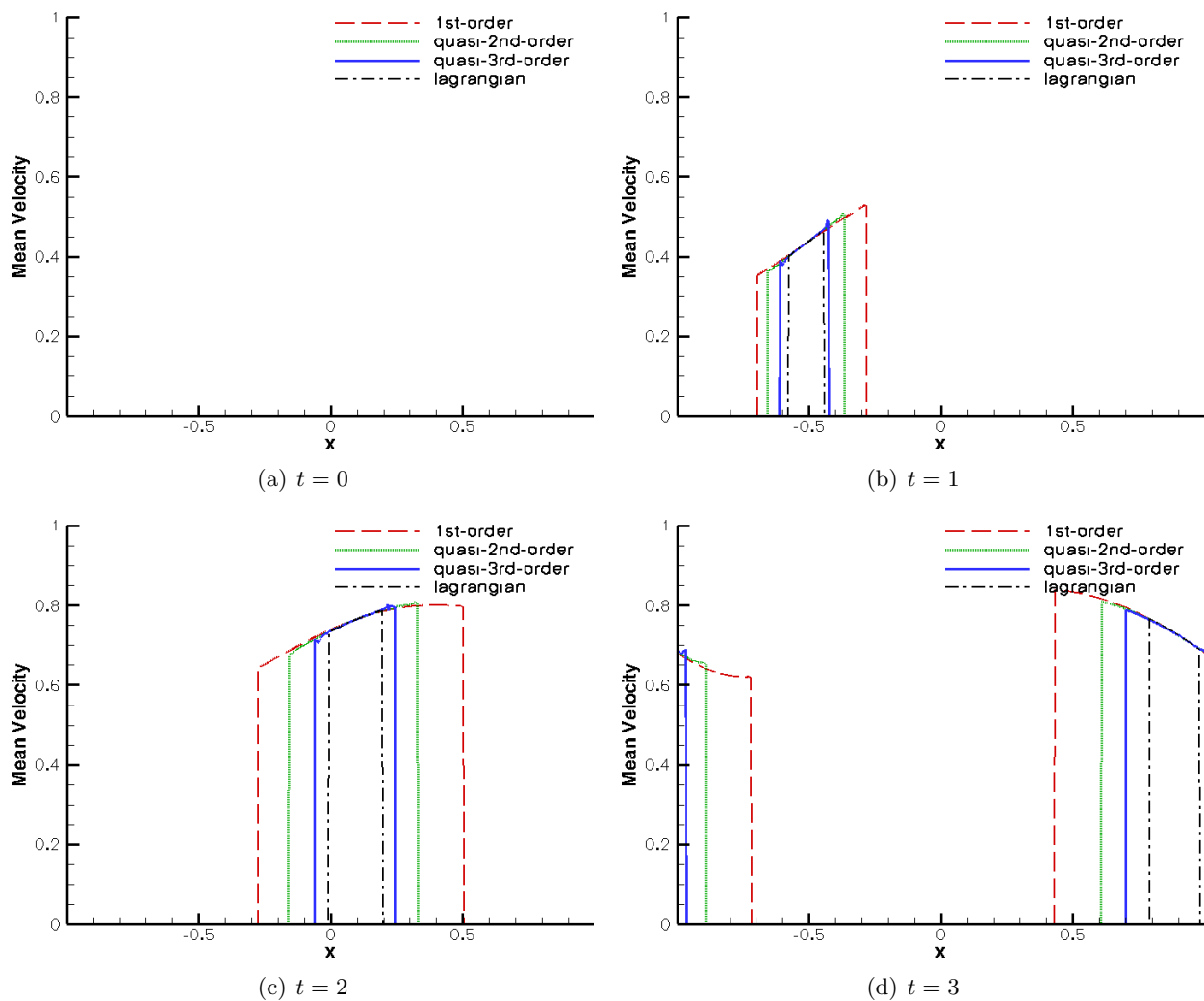


Figure 2.6 Comparison of schemes using mean velocity for 1-D case with convection and drag terms.

order results are closer to the Lagrangian results as compared to the 1st-order ones. Figure 2.6 shows comparisons for the mean velocity at the same times as in Figure 2.5. It is evident that the mean velocity is not constant but varies over a range of cells at each time. Clearly in such scenarios as well, the new realizable schemes give better solutions compared to the 1st-order scheme.

2.5.5 Comparison of schemes for 2-D case with only convection terms

Here a dilute impinging-jet problem in 2-D is presented. The domain consists of a square (7×7) box with two openings on the bottom wall through which particle jets enter. As time progresses, the jets cross each other, strike the wall and then rebound. These simulations are done using 4-node quadrature (n_1, U_1, V_1) , (n_2, U_2, V_2) , (n_3, U_3, V_3) , (n_4, U_4, V_4) . Initial ($t = 0$) conditions are given as:

$$\begin{aligned} n_1 = n_2 = n_3 = n_4 &= 0.0001, \\ U_1 = 0.001, \quad U_2 = -0.001, \quad U_3 = 0.001, \quad U_4 = -0.001, \\ V_1 = 0.001, \quad V_2 = 0.001, \quad V_3 = -0.001, \quad V_4 = -0.001. \end{aligned} \tag{2.74}$$

The values of the weights and abscissas at the left inlet jet (Dirichlet) are:

$$\begin{aligned} n_1 = n_2 = n_3 = n_4 &= 0.01, \\ U_1 = 1.001, \quad U_2 = 0.999, \quad U_3 = 1.001, \quad U_4 = 0.999, \\ V_1 = 1.001, \quad V_2 = 1.001, \quad V_3 = 0.999, \quad V_4 = 0.999. \end{aligned} \tag{2.75}$$

And the values at the right inlet jet (Dirichlet) are:

$$\begin{aligned} n_1 = n_2 = n_3 = n_4 &= 0.01, \\ U_1 = -1.001, \quad U_2 = -0.999, \quad U_3 = -1.001, \quad U_4 = -0.999, \\ V_1 = 1.001, \quad V_2 = 1.001, \quad V_3 = 0.999, \quad V_4 = 0.999. \end{aligned} \tag{2.76}$$

For elastic collisions with the walls, $e_w = 1$. Results are presented for the 1st-order and *quasi*-2nd-order schemes in Figure 2.7. The computational grid contains 2562 triangular elements. Figure 2.7(a) and 2.7(c) show the mean density using the 1st-order and *quasi*-2nd scheme, respectively, at $t = 4$ after the jets cross. Figures 2.7(b) and 2.7(d) show the mean density at $t = 7$ after the jets bounce off the walls. The solution obtained using the 1st-order scheme

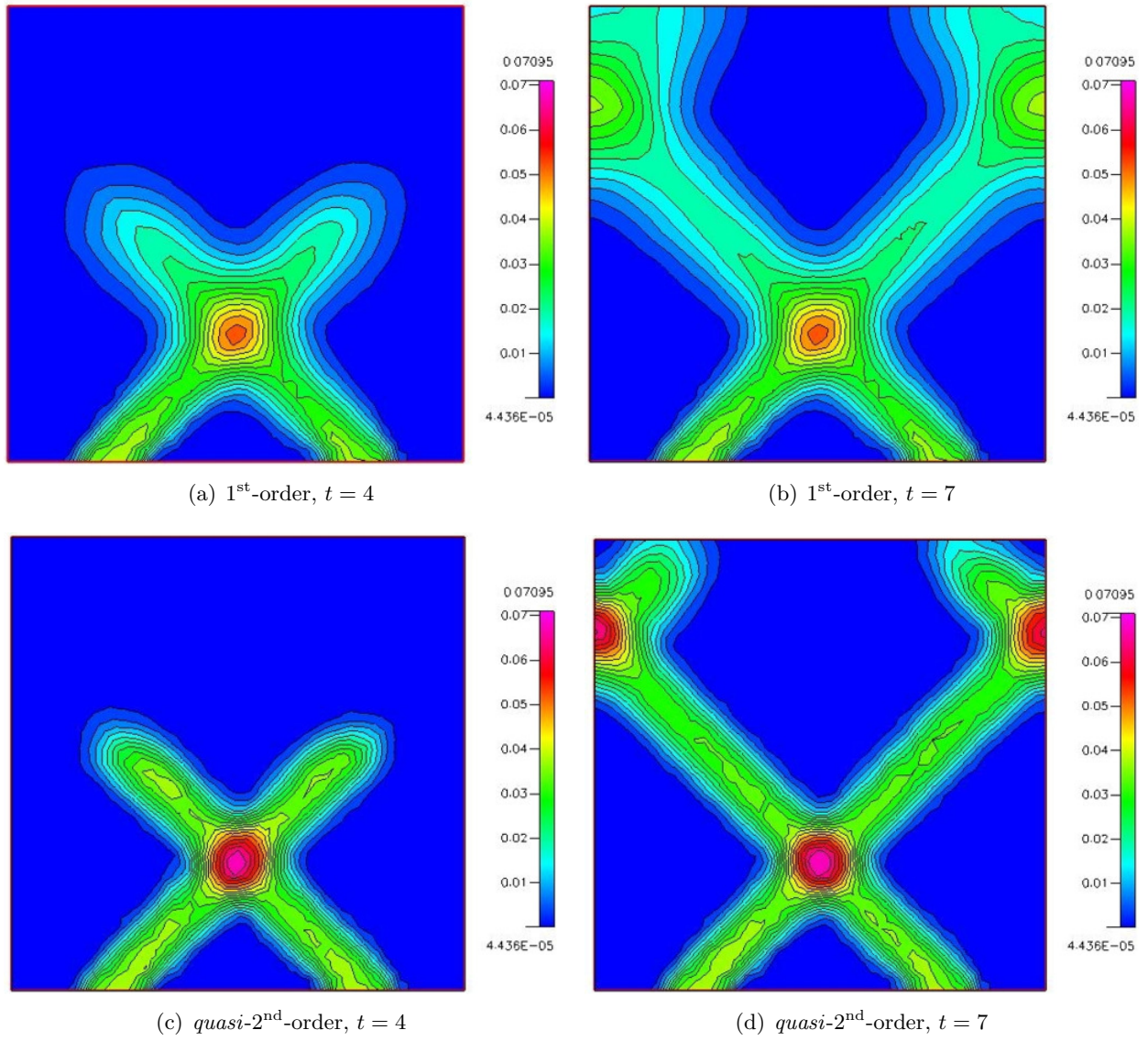


Figure 2.7 Mean particle density for crossing particle jets for different schemes at two times.

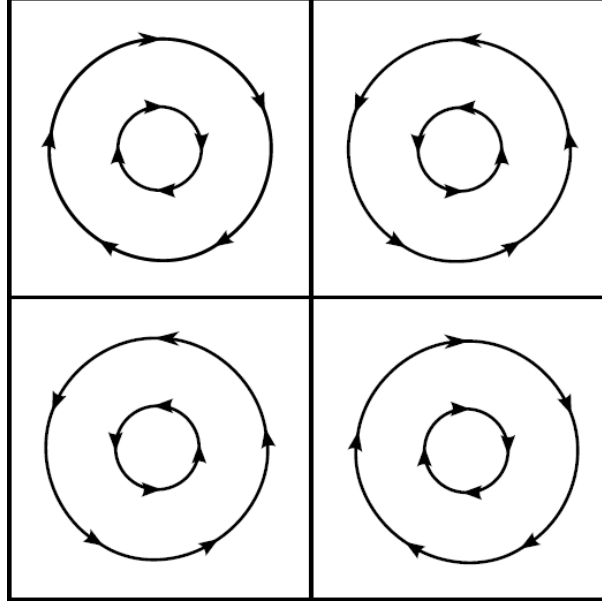


Figure 2.8 Fluid velocity for 2-D Taylor-Green flow.

is more diffused. The improvement in the solution using the *quasi-2nd*-order scheme is clearly evident.

2.5.6 Comparison of schemes for 2-D case with both convection and drag terms

In this case, the evolution of particles in a Taylor-Green flow is presented. The domain consists of a square (1×1) box. All the boundaries are periodic. The fluid velocity in the Taylor-Green flow is given by

$$\begin{aligned} U_{gx} &= \sin(2\pi x) \cos(2\pi y), \\ U_{gy} &= -\sin(2\pi y) \cos(2\pi x), \end{aligned} \tag{2.77}$$

and is shown in Figure 2.8. Figures 2.9 and 2.10 present results for different schemes on a structured mesh, and Figure 2.11 presents results for unstructured meshes. Results are presented for the 1st-order and *quasi-2nd*-order schemes at $t = 4$. For the structured mesh, four different grid resolutions are used: 100×100 , 200×200 , 400×400 , 800×800 . Lostec et al. [64] presented results for the same problem using both a Lagrangian simulation and 1st-order QMOM. Here, the Lagrangian result obtained in [64] is presented in Figure 2.12. Note that the particle number density shown in Figure 2.12 is proportional to the mean particle

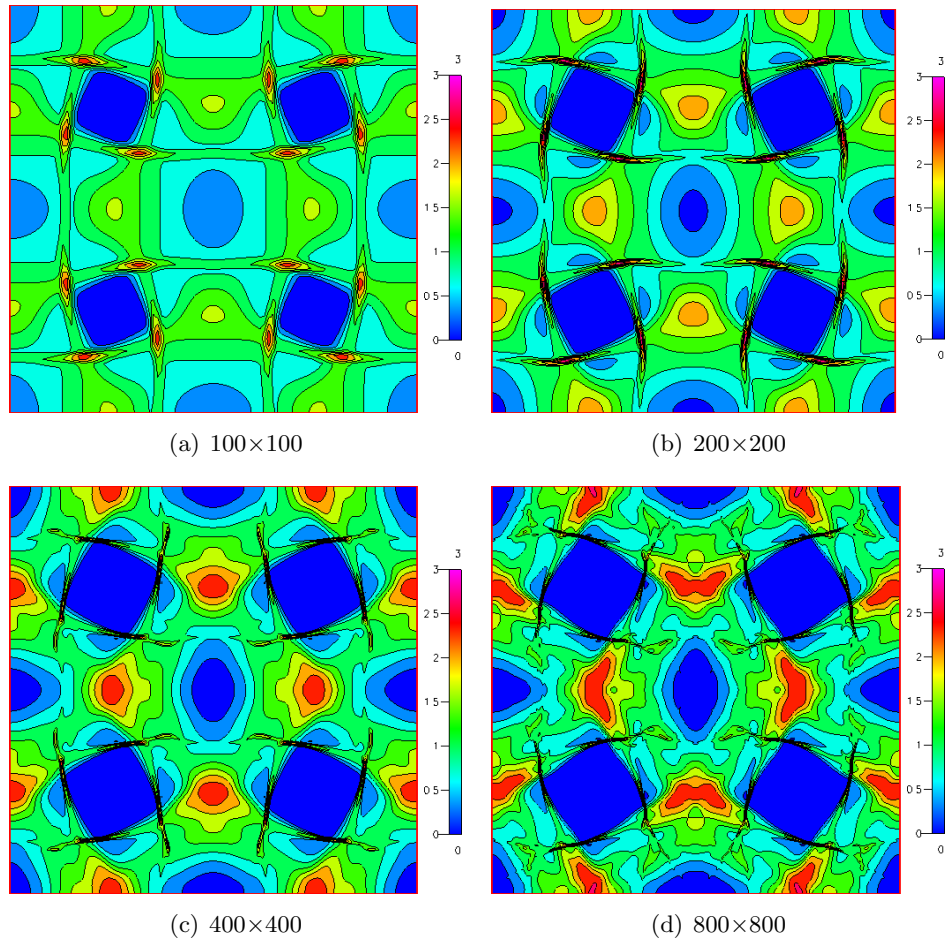


Figure 2.9 Grid resolution study of mean particle density in 2-D Taylor-Green flow at $t = 4$ with 1st-order scheme.

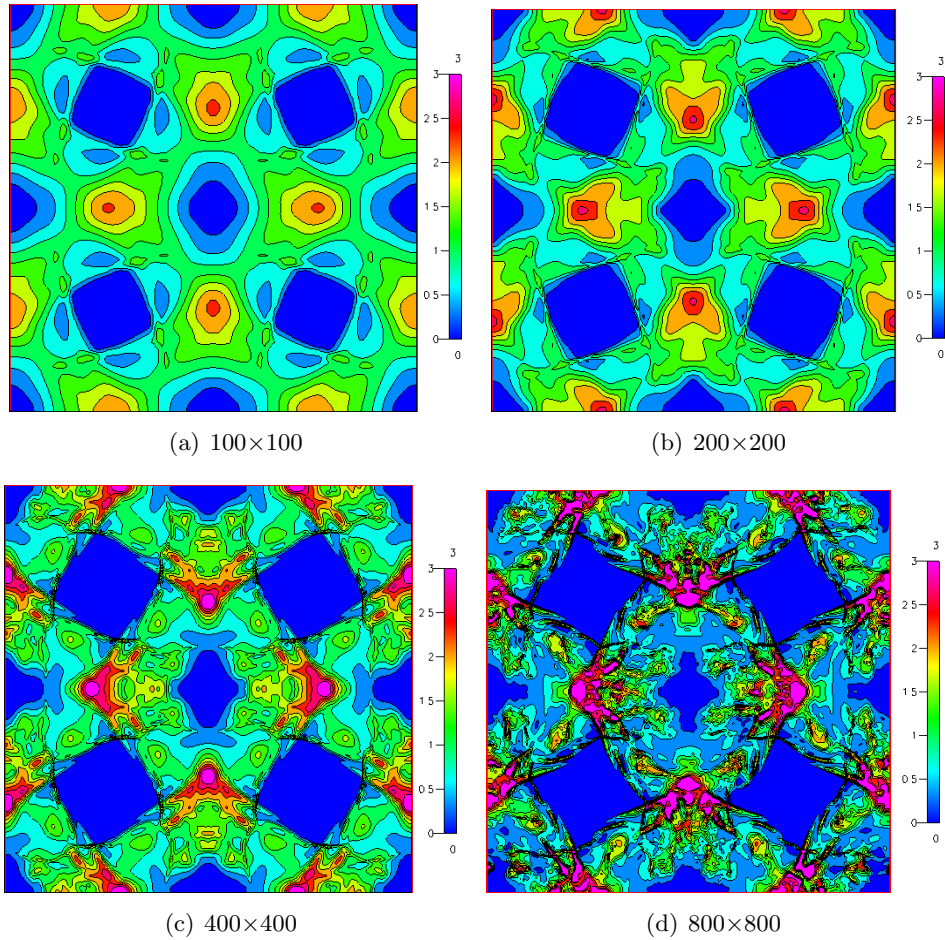


Figure 2.10 Grid resolution study of mean particle density in 2-D Taylor-Green flow at $t = 4$ with *quasi*-2nd-order scheme.

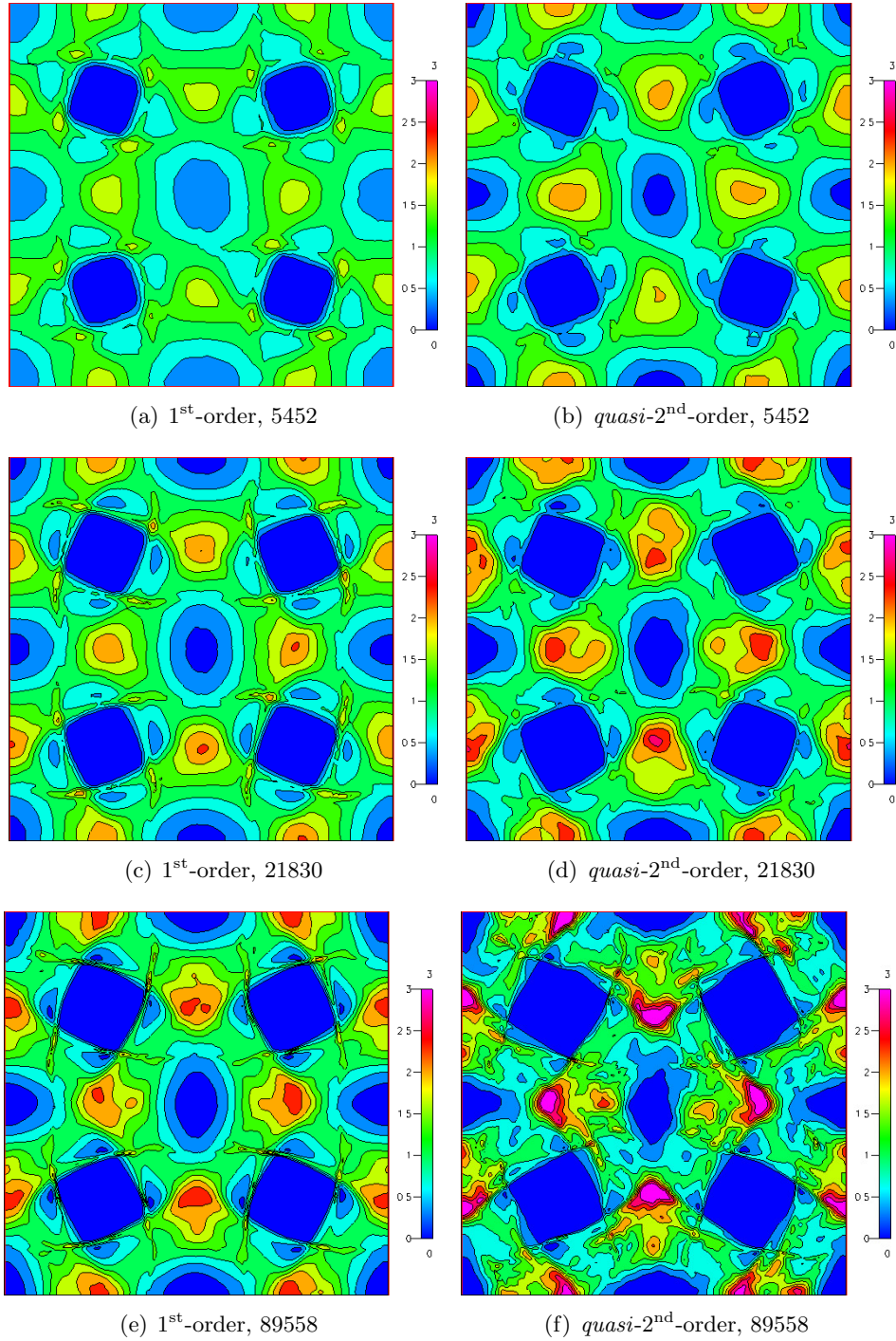


Figure 2.11 Mean particle density in 2-D Taylor-Green flow at $t = 4$ on triangular mesh with different schemes and cell numbers.

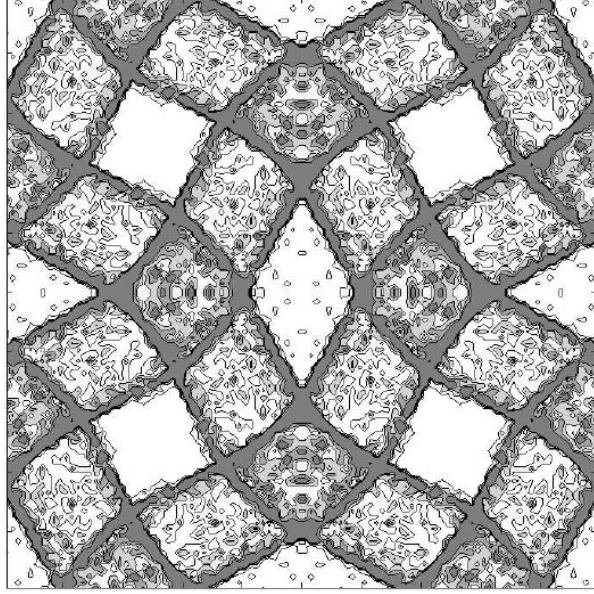


Figure 2.12 Particle number density in 2-D Taylor-Green flow obtained by Lostec et al. [64] using a Lagrangian simulation. Density is proportional to darkness.

density in our results. The results presented here clearly show that the *quasi-2nd*-order scheme fares much better compared to the 1st-order scheme in resolving the various features obtained in the Lagrangian simulation in [64]. The unstructured mesh consists of triangular cells. Three different grid resolutions are used with 5452, 21830 and 89558 triangular cells. The unstructured mesh results also confirm the improvement in the solutions when the *quasi-2nd*-order scheme is used.

2.6 Conclusions

Hitherto, the use of finite-volume schemes for quadrature-based moment methods was limited to the 1st-order scheme in order to guarantee realizability. Over the years, an extensive research effort has been spent on developing high-order finite-volume schemes in the field of computational fluid dynamics. However, the issue of non-realizability has often acted as a barrier, making these high-order finite-volume schemes inaccessible to models based on quadrature-based moment methods. Because of the non-realizability problem with *standard* high-order finite-volume schemes and the high numerical dissipation inherent in the first-order finite-

volume scheme, there is a need to develop schemes that can provide less-diffused results and guarantee realizability simultaneously.

In the present work, realizability of finite-volume schemes in both space and time has been discussed for the first time. A generalized idea has been proposed to develop high-order realizable finite-volume schemes. According to the new idea, a *quasi- p^{th}* -order realizable finite-volume scheme can be constructed using a p^{th} -order reconstruction for the weights and a 1st-order reconstruction for the abscissas along with a realizability criterion. These new schemes give remarkably improved solutions for a class of problems where the velocity field is constant or slowly varying over a range of cells. This marks a significant step as it makes all the high-order finite-volume schemes, developed over the years for fluid flows, automatically accessible to quadrature-based moment methods. It has also been shown that the standard Runge-Kutta time-integration schemes do not guarantee realizability. Instead, strong-stability-preserving Runge-Kutta schemes must be used. Numerical simulations have been carried out using both Cartesian and triangular meshes, and clearly demonstrate the increased accuracy and robustness of the proposed realizable high-order schemes.

Appendix. Realizable advection of velocity-independent density functions

For simplicity, only the one-dimensional case is discussed here. Discussion on two- and three-dimensional cases can be based by analogy on Sec. 2.3.3. If the density function does not include the velocity, v is not an independent variable. Denote the density function by $f \equiv f(b, x, t)$, where b is some scalar measure. For example, if b denotes the particle radius, then f is the density function for the particle size distribution. The population balance equation² with only the advection term can be written as:

$$\frac{\partial f}{\partial t} + \frac{\partial v f}{\partial x} = 0, \quad (2.78)$$

where $v \equiv v(x, t)$. The p^{th} -order moment of f can be defined as:

$$M^p = \int b^p f db. \quad (2.79)$$

²The transport equation for a velocity-independent density function is usually referred to as a population balance equation. In the aerosol literature, it is referred to as the general dynamic equation.

Applying the definition of moments to (2.78), the moment transport equations can be written as:

$$\frac{\partial M^p}{\partial t} + \frac{\partial v M^p}{\partial x} = 0 \quad \forall p \in \{0, 1, 2, \dots\}. \quad (2.80)$$

Define the set of conserved moments as $\mathbf{W} = [M^0 \ M^1 \ M^2 \ \dots]^T$ and the set of moment fluxes as $\mathbf{H}(v, \mathbf{W}) = v\mathbf{W} = v[M^0 \ M^1 \ M^2 \ \dots]^T$. Then the set of moment transport equations can be written as:

$$\frac{\partial \mathbf{W}}{\partial t} + \frac{\partial \mathbf{H}(v, \mathbf{W})}{\partial x} = 0. \quad (2.81)$$

The conserved moments and moment fluxes can be written in terms of the density function:

$$\mathbf{W} = \int \mathbf{K} f \, db, \quad \mathbf{H} = v \int \mathbf{K} f \, db, \quad (2.82)$$

where

$$\mathbf{K} = [1 \ b \ b^2 \ \dots]^T. \quad (2.83)$$

The moments can be advanced in time using a finite-volume scheme. If a single-stage Euler explicit time-integration scheme is used, the updated set of moments can be written as:

$$\begin{aligned} \mathbf{W}_i^{n+1} = \mathbf{W}_i^n - \lambda \left[\mathbf{G}(v_{i+1/2,l}^n, \mathbf{W}_{i+1/2,l}^n, v_{i+1/2,r}^n, \mathbf{W}_{i+1/2,r}^n) - \right. \\ \left. \mathbf{G}(v_{i-1/2,l}^n, \mathbf{W}_{i-1/2,l}^n, v_{i-1/2,r}^n, \mathbf{W}_{i-1/2,r}^n) \right], \end{aligned} \quad (2.84)$$

where $\lambda = \Delta t / \Delta x$. \mathbf{G} is the numerical flux function defined as:

$$\mathbf{G}(v_l^n, \mathbf{W}_l^n, v_r^n, \mathbf{W}_r^n) = v_l^+ \int \mathbf{K} f_l \, db + v_r^- \int \mathbf{K} f_r \, db, \quad (2.85)$$

where

$$v_l^+ = \frac{1}{2}(v_l + |v_l|) \quad \text{and} \quad v_r^- = \frac{1}{2}(v_r - |v_r|). \quad (2.86)$$

The updated set of moments can be written as:

$$\mathbf{W}^{n+1} = \int \mathbf{K} h \, db, \quad (2.87)$$

where

$$\begin{aligned} h = f_i^n - \lambda(v_{i+1/2,l}^{n+} f_{i+1/2,l}^n + v_{i+1/2,r}^{n-} f_{i+1/2,r}^n - v_{i-1/2,l}^{n+} f_{i-1/2,l}^n - v_{i-1/2,r}^{n-} f_{i-1/2,r}^n) \\ = f_i^n - \lambda v_{i+1/2,l}^{n+} f_{i+1/2,l}^n - \lambda v_{i+1/2,r}^{n-} f_{i+1/2,r}^n + \lambda v_{i-1/2,l}^{n+} f_{i-1/2,l}^n + \lambda v_{i-1/2,r}^{n-} f_{i-1/2,r}^n. \end{aligned} \quad (2.88)$$

Assuming that the moments at time level n correspond to a non-negative density function, three terms on the right-hand side of (2.88) – first, third, fourth – are non-negative and two terms – second, fifth – are non-positive. For the moments at time level $n+1$ to correspond to a non-negative density function, h should be non-negative for all b . The non-negativity of h can only be guaranteed for the first-order finite-volume scheme under a constraint on λ given by

$$(1 - \lambda|v_i^n|) \geq 0. \quad (2.89)$$

For second-order and, in general, any high-order finite-volume schemes, non-negativity of h cannot be guaranteed. However, if QMOM is used along with the *special* reconstruction discussed in Sec. 2.3, non-negativity of h can be guaranteed as shown below. For β -node QMOM, the density function can be written as:

$$f = \sum_{\alpha=1}^{\beta} n_{\alpha} \delta(b - B_{\alpha}), \quad (2.90)$$

where n_{α} are weights and B_{α} are abscissas.

Theorem 2. *Let $\beta, p \in \mathbb{N}$ and $\alpha \in \{1, 2, \dots, \beta\}$. Also let the cell-averaged and reconstructed values of the weights satisfy $n_{i,\alpha}^n > 0$ and $n_{i+1/2,\alpha,l}^n, n_{i-1/2,\alpha,r}^n \geq 0 \forall \alpha$. If a finite-volume scheme using a single-stage Euler explicit time-integration scheme is devised that uses a p^{th} -order reconstruction for the weights and 1^{st} -order reconstruction for the abscissas, the non-negativity of the effective density function (2.88) in the i^{th} cell can always be guaranteed under an explicit constraint on time-step size ($\Delta t \in \mathbb{R}^+$).*

Proof. *Using (2.88), the effective density function, regardless of the finite-volume scheme used, can be written as:*

$$h = f_i^n - \lambda v_{i+1/2,l}^{n+} f_{i+1/2,l}^n + \lambda v_{i-1/2,r}^{n-} f_{i-1/2,r}^n + \xi^+. \quad (2.91)$$

In the above expression, the third and fourth non-negative terms have been grouped under ξ^+ .

For a β -node quadrature, using (2.90), the expression for h becomes:

$$\begin{aligned} h = \sum_{\alpha=1}^{\beta} [n_{i,\alpha}^n \delta(b - B_{i,\alpha}^n) - \lambda v_{i+1/2,l}^{n+} n_{i+1/2,\alpha,l}^n \delta(b - B_{i+1/2,\alpha,l}^n) \\ + \lambda v_{i-1/2,r}^{n-} n_{i-1/2,\alpha,r}^n \delta(b - B_{i-1/2,\alpha,r}^n)] \\ + \xi^+. \end{aligned} \quad (2.92)$$

If a first-order reconstruction is used for the abscissas, then the interface values of the abscissas will be the same as the cell-averaged values:

$$B_{i,\alpha}^n = B_{i+1/2,\alpha,l}^n = B_{i-1/2,\alpha,r}^n. \quad (2.93)$$

Putting this in (2.92), the effective density function becomes:

$$h = \sum_{\alpha=1}^{\beta} \{n_{i,\alpha}^n - \lambda v_{i+1/2,l}^{n+} n_{i+1/2,\alpha,l}^n + \lambda v_{i-1/2,r}^{n-} n_{i-1/2,\alpha,r}^n\} \delta(b - B_{i,\alpha}^n) + \xi^+. \quad (2.94)$$

For $\Delta t \in \mathbb{R}^+$ satisfying the condition:

$$\lambda = \min_{\alpha \in \{1,2,\dots,\beta\}} \left(\frac{n_{i,\alpha}^n}{n_{i+1/2,\alpha,l}^n v_{i+1/2,l}^{n+} - n_{i-1/2,\alpha,r}^n v_{i-1/2,r}^{n-}} \right), \quad (2.95)$$

h is non-negative for all b . This concludes the proof. \square

The extension to realizable high-order time integration is analogous to the methods presented in Sec. 2.4.

CHAPTER 3. REALIZABLE HIGH-ORDER FINITE-VOLUME SCHEMES FOR QUADRATURE-BASED MOMENT METHODS APPLIED TO DIFFUSION POPULATION BALANCE EQUATIONS

A paper submitted to Journal of Computational Physics

Varun Vikas¹, Z. J. Wang, Rodney O. Fox

Abstract

Population balance equation (PBE) with convection and diffusion terms occurs in mesoscopic models for many physical phenomena. Direct numerical solution of these PBEs is often infeasible because of the large number of independent variables. An alternative is to reformulate the problem in terms of the moments of the distribution function. The moment transport equations are not closed and a quadrature-based moment method (QBMM) can be used for closure. The success of QBMM is based on a moment-inversion algorithm that is used to calculate non-negative weights and abscissas from the moments. The moment-inversion algorithm does not work if the moments are non-realizable, which might lead to negative weights. Moreover, realizability of the moments is needed for the abscissas to lie in the interior of support of the distribution function. Several researchers have discussed the realizability problems in the context of convection terms. Recently, new high-order realizable finite-volume schemes with appropriate realizability criteria have been derived for the convection terms. However, to the authors' knowledge, hitherto no work has been done with respect to the realizability problems for the diffusion terms. The current paper is focused on developing high-order realizable finite-volume schemes for the diffusion terms. The paper discusses the pitfalls of the already

¹Primary researcher and author.

existing finite-volume schemes for the diffusion terms, that are based on the reconstruction of moments. It is shown that when using the moment-based reconstruction, the realizability can be guaranteed only with 2nd-order scheme. It is also shown that the realizability criterion for the 2nd-order scheme is same as the stability criterion. The paper shows that the realizability of moments cannot be guaranteed when the high-order moment-based reconstruction schemes are used. New realizable high-order finite-volume schemes based on the reconstruction of weights and abscissas, instead of moments, are proposed and suitable realizability criteria are derived. The new schemes can achieve higher than 2nd-order accuracy for the problems with smoothly varying abscissas. In the worst case scenario of highly nonlinear abscissas, the new schemes are 2nd-order accurate. It is also shown that the results obtained using the new realizable high-order schemes are consistent with those obtained using the 2nd-order moment-based reconstruction scheme.

3.1 Introduction

Population balance equations occur in mesoscopic models for a wide range of physical phenomena [19, 76, 15, 122]. These PBEs include convection and diffusion terms among others. One of the approaches to solve the PBEs is to use a direct solver that discretizes the phase space of the distribution function. However, very often due to the high-dimensionality of the phase space, such a direct solver is infeasible. An alternative is to formulate the problem in terms of the moments of the distribution function. However, the moment transport equations are often unclosed and a closure model is needed. Quadrature-based moment method [25, 33, 34, 35, 65] can be used as a closure model. QBMM assumes a quadrature approximation of the distribution function. The key step of the approach is an inversion algorithm that allows one to uniquely determine a set of weights and abscissas from the set of transported moments. The condition for the inversion algorithm to be applied is that the set of moments is realizable, meaning it actually corresponds to a distribution function. This condition is not generally satisfied by the traditional high-order finite-volume schemes used in computational fluid dynamics (CFD) [5, 56, 60, 113, 118, 120].

Several researchers have discussed the treatment of convection terms in detail [72, 73, 85,

124]. Desjardins et al. [25] showed that the realizability of the moment transport equations with convection terms is guaranteed only for the 1st-order finite-volume scheme. The use of any other high-order finite-volume scheme may lead to non-realizable moments, thereby resulting in negative weights and abscissas that are outside the support of the distribution function. This limitation required the use of a highly refined mesh for computation as a first-order finite-volume scheme produces highly diffused solutions on a coarse mesh. Vikas et al. [115] developed high-order realizable finite-volume schemes for the convection terms. These schemes work better than the 1st-order scheme and guarantee realizability of the moments using an explicit constraint on the time-step size. This constraint is called the realizability criterion.

To the authors' knowledge, the issue of realizability for the diffusion terms has not yet been studied. The current paper studies the realizability issues when QBMM is applied to the PBEs with diffusion terms. Diffusion processes often appear in PBEs as a result of successive approximations, due to some phenomena that are not described in detail. These phenomena are typically modeled with a sort of sub-scale model and represented in an Eulerian framework as diffusion processes. They are generated by advection (in physical- or phase-space) processes characterized by a random chaotic nature and by time- and length-scales usually smaller than those of the dominant phenomena. Brownian forces, turbulent fluctuations, random lattice-defects in crystals are the most common sources of phase-, physical- and mixed phase- and physical-space diffusion processes.

The moment transport equations for the PBEs with diffusion terms can be closed using QBMM and a finite-volume approach can be applied to advance the moments in time. When a finite-volume scheme is used, the computation of diffusive flux at the faces requires the availability of moment derivatives at the faces. Hitherto, the moment derivatives were computed using a moment-based reconstruction without any proof of realizability. The moment-based reconstruction uses finite-volume reconstruction schemes to compute the derivatives by directly using the cell-averaged values of the moments. The current paper discusses the pitfalls of reconstruction schemes based on moments. It shows that when using moment-based reconstruction, the realizability cannot be guaranteed for higher than 2nd-order schemes. For the 2nd-order scheme, the realizability criterion and the stability criterion, also known as CFL condition, are

same. Hence, in the past when using 2nd-order scheme, no realizability problems have been encountered as stability criterion is always accounted for. The paper proposes new schemes based on the reconstruction of weights and abscissas, instead of moments, and derives realizability conditions for these schemes. The new schemes can achieve higher than 2nd-order accuracy for the problems with smoothly varying abscissas. Formal high-order of accuracy can be achieved for the problems with constant or linearly varying abscissas. In the worst case scenario of highly nonlinear abscissas, the new schemes are at least 2nd-order accurate. It is also shown that the results obtained using the new realizable high-order schemes are consistent with those obtained using the 2nd-order moment-based reconstruction scheme.

The remainder of this paper is organized as follows. In Sec. 3.2, QBMM is reviewed. Section 3.2 also discusses the finite-volume schemes and their realizability properties. Thereafter, in Sec. 3.3, new realizable high-order finite-volume schemes are presented for the one-dimensional cases. Section 3.4 deals with the new realizable schemes for the multidimensional cases. Section 3.5 presents some numerical results. Conclusions from the present study are summarized in Sec. 3.6.

3.2 Quadrature-based moment method

3.2.1 Diffusion PBE

The diffusion PBE can be written as

$$\frac{\partial f}{\partial t} = \nabla \cdot (\mu \nabla f), \quad (3.1)$$

where $f(b, \mathbf{x}, t)$ is the distribution function, $\mu(b, \mathbf{x}, t)$ is the diffusivity coefficient and the internal coordinate, b , is a scalar measure. For example, if b denotes the particle radius, then f is the particle size distribution function. Here, the case of only one internal coordinate is discussed. However, the same idea can be applied to the cases with multiple internal coordinates. For the sake of clarity, the first half of the paper will focus on the one-dimensional version of the above equation with $f = f(b, x, t)$ and $\mu = \mu(b)$:

$$\frac{\partial f}{\partial t} = \mu \frac{\partial^2 f}{\partial x^2}. \quad (3.2)$$

Towards the later half, the multidimensional version will also be discussed. For simplicity, the spatial dependence of μ has been removed but it is not a constraint. Spatial variations in the diffusivity coefficient can be included under the same framework.

3.2.2 Moment transport equations

The moment transport equations corresponding to (3.2) can be written as

$$\frac{\partial M^p}{\partial t} = \frac{\partial^2 S^p}{\partial x^2} \quad \forall p, \quad (3.3)$$

where

$$M^p = \int b^p f db \quad \text{and} \quad S^p = \int \mu(b) b^p f db \quad (3.4)$$

are the moments of the distribution function. Note that $M^p \equiv M^p(x, t)$ and $S^p \equiv S^p(x, t)$. In (3.4), the integrals are performed over the interval of support of the distribution function. In the moment method, a finite number of moments are tracked. The above system is not closed at any finite p . In order to close the system, a closure model is needed. In this paper, QBMM is used for closure.

3.2.3 Quadrature-based closures

In quadrature-based moment methods, quadrature formulas are used to provide closures to the unclosed terms in the moment transport equations, by introducing a set of weights and abscissas. The distribution function f is written in terms of the quadrature weights (w_α) and abscissas (B_α) using a Dirac delta representation:

$$f = \sum_{\alpha=1}^{\beta} w_\alpha \delta(b - B_\alpha), \quad (3.5)$$

where $w_\alpha \equiv w_\alpha(x, t)$ and $B_\alpha \equiv B_\alpha(x, t)$. The method based on (3.5) is called β -node quadrature method. The moments can be computed as a function of quadrature weights and abscissas by using the above definition of f in (3.4):

$$M^p = \sum_{\alpha=1}^{\beta} w_\alpha B_\alpha^p, \quad S^p = \sum_{\alpha=1}^{\beta} w_\alpha \mu(B_\alpha) B_\alpha^p. \quad (3.6)$$

Note that when using a β -node quadrature, at each time-step 2β unknowns (β weights and β abscissas) are to be determined from the tracked moments. Hence, it is necessary to track 2β moments ($p \in \{0, 1, \dots, 2\beta - 1\}$).

Often pointwise values of the distribution function are required but the quadrature-based closure mentioned above fails to provide these. To curb this problem, recently a new generation of QBMM has been introduced that provides an explicit form for the distribution function. This new method is referred to as extended quadrature method of moments (EQMOM) [127]. EQMOM approximates the distribution function by a sum of smooth non-negative functions. However, when evaluating fluxes using EQMOM, the smooth distribution function can be recast in the Dirac delta form. Hence, unless otherwise stated, all the discussion refers to the quadrature based closure that uses the Dirac delta representation.

3.2.4 Finite-volume method

For the p^{th} -order moment, the finite-volume expression using the single-stage Euler explicit time-integration can be written as

$$\overline{M}_i^{p,n+1} = \overline{M}_i^{p,n} + \frac{\Delta t}{\Delta x} \left[\left. \frac{\partial S^p}{\partial x} \right|_{i+1/2}^n - \left. \frac{\partial S^p}{\partial x} \right|_{i-1/2}^n \right], \quad (3.7)$$

where superscripts n and $n + 1$ denote time levels and $\left. \frac{\partial S^p}{\partial x} \right|_{i+1/2}^n$ is the diffusive flux evaluated at cell interfaces. Henceforth, the variables with overbars denote the cell-averaged values. The variables with $(i + 1/2)$ or $(i - 1/2)$ as subscript denote the reconstructed values at the faces. The cell-averaged values, $\overline{M}_i^{p,n}$, are known but the diffusive fluxes at the faces are not known. In order to compute the diffusive flux, $\left. \frac{\partial S^p}{\partial x} \right|_{i+1/2}^n$, at the face $i + 1/2$, a profile for S^p at time level n has to be reconstructed around this face and then this profile can be differentiated to get the required flux. The cell-averaged values of S^p are known in each cell using the expression in (3.6). These values can be used to reconstruct a profile for S^p around each face. A profile reconstruction with degree- $(k - 1)$ polynomial will lead to the k^{th} -order accurate finite-volume scheme. The following sections discuss second and fourth-order schemes respectively. For the sake of simplicity, only the 1st-order Euler explicit time-integration is discussed. However, for numerical tests in Sec. 3.5, a two-stage 2nd-order RK2SSP time-integration scheme [42] is used.

3.2.4.1 Second-order finite-volume scheme

For the 2nd-order finite-volume scheme, a linear profile (degree-1 polynomial) is reconstructed at the face $i + 1/2$:

$$S_{i+1/2}^{p,n}(x) = a_0 + a_1x, \quad (3.8)$$

where the unknowns a_0 and a_1 are computed using the following two conditions:

$$\frac{1}{\Delta x} \int_{x_{j-1/2}}^{x_{j+1/2}} S_{i+1/2}^{p,n}(x) dx = \bar{S}_j^{p,n} \text{ where } j \in \{i, i + 1\}. \quad (3.9)$$

The reconstructed profile can then be differentiated to get the flux at the face $i + 1/2$:

$$\left. \frac{\partial S^p}{\partial x} \right|_{i+1/2}^n = \frac{1}{\Delta x} [\bar{S}_{i+1}^{p,n} - \bar{S}_i^{p,n}]. \quad (3.10)$$

Using this, the updated moment for the second-order finite-volume scheme can be written as

$$\bar{M}_i^{p,n+1} = \bar{M}_i^{p,n} + \frac{\Delta t}{\Delta x^2} [\bar{S}_{i+1}^{p,n} - 2\bar{S}_i^{p,n} + \bar{S}_{i-1}^{p,n}]. \quad (3.11)$$

This is the standard second-order finite-volume scheme used in CFD for the diffusion problems. Later on it will be shown that this is a realizable scheme with the realizability criterion same as the stability criterion.

3.2.4.2 Fourth-order finite-volume scheme

For the 4th-order scheme, a cubic profile (degree-3 polynomial) is reconstructed at the face $i + 1/2$:

$$S_{i+1/2}^{p,n}(x) = a_0 + a_1x + a_2x^2 + a_3x^3, \quad (3.12)$$

where the unknowns a_0 , a_1 , a_2 and a_3 are computed using the following four conditions:

$$\frac{1}{\Delta x} \int_{x_{j-1/2}}^{x_{j+1/2}} S_{i+1/2}^{p,n}(x) dx = \bar{S}_j^{p,n} \text{ where } j \in \{i - 1, i, i + 1, i + 2\}. \quad (3.13)$$

The reconstructed profile can then be differentiated to get the flux at the face $i + 1/2$:

$$\left. \frac{\partial S^p}{\partial x} \right|_{i+1/2}^n = \frac{1}{\Delta x} \left[\frac{1}{12} \bar{S}_{i-1}^{p,n} - \frac{5}{4} \bar{S}_i^{p,n} + \frac{5}{4} \bar{S}_{i+1}^{p,n} - \frac{1}{12} \bar{S}_{i+2}^{p,n} \right] \quad (3.14)$$

Using this, the updated moment for the second-order finite-volume scheme can be written as

$$\bar{M}_i^{p,n+1} = \bar{M}_i^{p,n} + \frac{\Delta t}{\Delta x^2} \left[-\frac{1}{12} \bar{S}_{i-2}^{p,n} + \frac{4}{3} \bar{S}_{i-1}^{p,n} - \frac{5}{2} \bar{S}_i^{p,n} + \frac{4}{3} \bar{S}_{i+1}^{p,n} - \frac{1}{12} \bar{S}_{i+2}^{p,n} \right]. \quad (3.15)$$

Later on it will be shown that this is a non-realizable scheme.

The third-order finite-volume scheme is not discussed just for the sake of simplicity. The third-order finite-volume scheme needs a quadratic profile (degree-2 polynomial). To compute the unknown coefficients in the quadratic profile, three cells are needed. Three cells form an asymmetric stencil around the face $i + 1/2$. In order to avoid this asymmetry, two stencils are used for the face $i + 1/2$ ($\{i - 1, i, i + 1\}$ and $\{i, i + 1, i + 2\}$) and the computed derivatives are averaged. So, the effective stencil for the third-order finite-volume scheme is same as that for the fourth-order finite-volume scheme, although the coefficients will be different.

3.2.5 Non-realizability problem

At each time-step, the weights and abscissas are recovered from the moments. For univariate cases (single internal coordinate), the moment-inversion algorithm computes the set of weights and abscissas from the corresponding set of moments using the product-difference (PD) algorithm [71, 86, 121]. The discussion on moment-inversion algorithms for multivariate cases can be found in [33, 34, 126, 127]. The set of moments cannot be constituted by arbitrary values of each moment, but they have to conform to the definition of the *non-negative* distribution function. The application of the moment-inversion algorithm to a set of realizable moments leads to a set of non-negative weights. Moreover, the abscissas lie in the interior of support of f . Because of the non-linearity of the inversion problem, it is extremely difficult to determine in advance whether a given set of moments is realizable. However, Desjardins et al. [25] described that any finite-volume scheme that could guarantee non-negativity of the updated distribution function will always keep the moments in the realizable space. Vikas et al. [115] developed realizable high-order finite-volume schemes for the convection terms. This paper is concerned with the development of realizable high-order finite-volume schemes for the diffusion terms. But before presenting the new realizable high-order finite-volume schemes, the pitfalls of already existing finite-volume schemes based on the reconstruction of moments is discussed.

3.2.5.1 Unique update of distribution function

The finite-volume scheme in (3.7) can also be written as

$$\int b^p \left\{ \bar{f}_i^{n+1} = \bar{f}_i^n + \frac{\Delta t}{\Delta x} \mu(b) \left[\left. \frac{\partial f}{\partial x} \right|_{i+1/2}^n - \left. \frac{\partial f}{\partial x} \right|_{i-1/2}^n \right] \right\} db. \quad (3.16)$$

This implies that, although the different moments are evolved in time independent of each other, there is a unique update of the distribution function at each time step:

$$\bar{f}_i^{n+1} = \bar{f}_i^n + \frac{\Delta t}{\Delta x} \mu(b) \left[\left. \frac{\partial f}{\partial x} \right|_{i+1/2}^n - \left. \frac{\partial f}{\partial x} \right|_{i-1/2}^n \right]. \quad (3.17)$$

Any finite-volume scheme that can guarantee the non-negativity of $\bar{f}_i^{n+1} \forall b$ is called a realizable scheme.

It is worth reiterating that the unique update of f in (3.17) is possible only if all moments use the same stencil for computing the diffusive fluxes $\partial S^p / \partial x|_{i-1/2}^n$ and $\partial S^p / \partial x|_{i+1/2}^n$. For the diffusion problems, the profiles are always smooth and no limiter is required. Hence, for the diffusion problems all moments use the same stencil, thereby guaranteeing the unique update for f . However, for the convection problems some moments may have discontinuities while others may not. The convection problems are hyperbolic and allow the propagation of discontinuities. Hence, for the convection problems, while reconstructing the profiles for the moments, limiters may be required for some moments but not for others. This means that stencils may vary from one moment to another. In that case a moment-based reconstruction will not guarantee a unique update of f . This is one of the reasons as to why the realizability problem is more prevalent for the convection problems.

3.2.5.2 Second-order finite-volume scheme

For the second-order finite-volume scheme, (3.10) implies

$$\left. \frac{\partial f}{\partial x} \right|_{i+1/2}^n = \frac{1}{\Delta x} \left[\bar{f}_{i+1}^n - \bar{f}_i^n \right]. \quad (3.18)$$

Putting this into (3.17) and simplifying, the unique update of f can be written as

$$\bar{f}_i^{n+1} = \left[1 - 2\mu(b) \frac{\Delta t}{\Delta x^2} \right] \bar{f}_i^n + \mu(b) \frac{\Delta t}{\Delta x^2} \left[\bar{f}_{i+1}^n + \bar{f}_{i-1}^n \right]. \quad (3.19)$$

The non-negativity of \bar{f}_i^{n+1} will be guaranteed if

$$\left[1 - 2\mu(\bar{B}_{\alpha,i}^n) \frac{\Delta t}{\Delta x^2}\right] \geq 0 \quad \forall \alpha \in \{1, 2, \dots, \beta\}. \quad (3.20)$$

Note that this is same as the stability condition used for the diffusion problems. When performing numerical simulations, as Δt is always chosen on the basis of stability condition, realizability condition is automatically satisfied and hence realizability problems have never been encountered in the past for the 2nd-order scheme.

3.2.5.3 Fourth-order finite-volume scheme

For the fourth-order finite-volume scheme, (3.14) implies

$$\frac{\partial f}{\partial x} \Big|_{i+1/2}^n = \frac{1}{\Delta x} \left[\frac{1}{12} \bar{f}_{i-1}^n - \frac{5}{4} \bar{f}_i^n + \frac{5}{4} \bar{f}_{i+1}^n - \frac{1}{12} \bar{f}_{i+2}^n \right]. \quad (3.21)$$

Putting this into (3.17) and simplifying, the unique update of f can be written as

$$\bar{f}_i^{n+1} = \left[1 - \frac{5}{2}\mu(b) \frac{\Delta t}{\Delta x^2}\right] \bar{f}_i^n + \frac{4}{3}\mu(b) \frac{\Delta t}{\Delta x^2} [\bar{f}_{i+1}^n + \bar{f}_{i-1}^n] - \frac{1}{12}\mu(b) \frac{\Delta t}{\Delta x^2} [\bar{f}_{i+2}^n + \bar{f}_{i-2}^n]. \quad (3.22)$$

Note that regardless of what Δt is chosen, the non-negativity of the two terms on the right side, involving \bar{f}_{i-2}^n and \bar{f}_{i+2}^n , can never be guaranteed. Hence, this scheme cannot guarantee the realizability of the updated moment set.

3.3 Improved realizable finite-volume schemes

3.3.1 Basic idea

Putting (3.5) into the terms on right side (3.22) gives

$$\begin{aligned} \bar{f}_i^{n+1} = & \sum_{\alpha=1}^{\beta} \left\{ \left[1 - \frac{5}{2}\mu(b) \frac{\Delta t}{\Delta x^2}\right] \bar{w}_{\alpha,i}^n \delta(b - \bar{B}_{\alpha,i}^n) \right. \\ & + \frac{4}{3}\mu(b) \frac{\Delta t}{\Delta x^2} [\bar{w}_{\alpha,i+1}^n \delta(b - \bar{B}_{\alpha,i+1}^n) + \bar{w}_{\alpha,i-1}^n \delta(b - \bar{B}_{\alpha,i-1}^n)] \\ & \left. - \frac{1}{12}\mu(b) \frac{\Delta t}{\Delta x^2} [\bar{w}_{\alpha,i+2}^n \delta(b - \bar{B}_{\alpha,i+2}^n) + \bar{w}_{\alpha,i-2}^n \delta(b - \bar{B}_{\alpha,i-2}^n)] \right\}. \end{aligned} \quad (3.23)$$

The weights and abscissas with overbars in (3.23) are computed by inverting the cell-averaged moments. The two non-positive terms on the right-hand side, involving $\bar{B}_{\alpha,i-2}^n$ and $\bar{B}_{\alpha,i+2}^n$ may

lead to the non-realizability problem. To understand the cause of the non-realizability problem, it helps to think of the Dirac delta representation in terms of discrete particles. Thinking along these lines, it can be said that at time level n , cell i only contains particles with sizes $\overline{B}_{\alpha,i}^n$. This means that only particles with sizes $\overline{B}_{\alpha,i}^n$ can be moved out of cell i . But the last two terms mean that particles with sizes $\overline{B}_{\alpha,i-2}^n$ and $\overline{B}_{\alpha,i+2}^n$ are being moved out of cell i . Doing so turns the distribution function corresponding to these sizes, in cell i , negative as it did not contain particles with these sizes in the first place. The origin of this problem is inherent in the use of stencil $\{i-1, i, i+1, i+2\}$ at the face $i+1/2$ and $\{i-2, i-1, i, i+1\}$ at the face $i-1/2$. The problem can be solved by using smaller stencils: $\{i, i+1\}$ at the face $i+1/2$ and $\{i-1, i\}$ at the face $i-1/2$. But that would lead to the 2nd-order scheme. The purpose of this paper is to develop a scheme that does better than the 2nd-order scheme, at least for some problems, and simultaneously guarantees realizability. If instead of reconstructing the moments, the weights and abscissas are reconstructed separately, this purpose can be served. For the weights, any stencil, however large can be used. However, for the abscissas, if the 2nd-order stencils ($\{i, i+1\}$ at the face $i+1/2$ and $\{i-1, i\}$ at the face $i-1/2$) are used, the realizability problem can be solved as shown below. This approach means that reconstruction polynomials of different degrees have to be used for the weights and abscissas. In order to use the reconstruction polynomials of different degrees, the terms involving weights and abscissas should be separated using the chain rule:

$$\begin{aligned} \frac{\partial f}{\partial x} \Big|_{i+1/2}^n &= \sum_{\alpha=1}^{\beta} \left[\frac{\partial}{\partial x} (w_{\alpha} \delta(b - B_{\alpha})) \Big|_{i+1/2}^n \right] \\ &= \sum_{\alpha=1}^{\beta} \left[w_{\alpha,i+1/2}^n \frac{\partial \delta(b - B_{\alpha})}{\partial x} \Big|_{i+1/2}^n + \frac{\partial w_{\alpha}}{\partial x} \Big|_{i+1/2}^n \delta(b - B_{\alpha}) \Big|_{i+1/2}^n \right]. \end{aligned} \quad (3.24)$$

The high-order finite-volume schemes use degree- $(k-1)$ reconstruction ($k > 2$) for all the four terms on the right side. However, this leads to the non-realizability problem. In order to avoid this, consider a special scheme where degree- $(k-1)$ reconstruction ($k \geq 2$) is used for the terms involving weights ($w_{\alpha,i+1/2}^n$ and $\partial w_{\alpha} / \partial x \Big|_{i+1/2}^n$) but only degree-1 reconstruction is used for the terms involving abscissas ($\partial \delta(b - B_{\alpha}) / \partial x \Big|_{i+1/2}^n$ and $\delta(b - B_{\alpha}) \Big|_{i+1/2}^n$). For this special scheme, realizability can *often* be guaranteed with a suitable constraint on the time-step size. This is

the subject of the following theorem.

Theorem 1. *Let $\beta, k \in \mathbb{N}$ and $\alpha \in \{1, 2, \dots, \beta\}$. Also let the cell-averaged values of the weights and their reconstructed values and derivatives at the faces satisfy $\bar{w}_{\alpha,i}^n > 0$, $w_{\alpha,i-1/2}^n - \Delta x/2 \partial w_{\alpha}/\partial x|_{i-1/2}^n \geq 0$ and $w_{\alpha,i+1/2}^n + \Delta x/2 \partial w_{\alpha}/\partial x|_{i+1/2}^n \geq 0 \forall \alpha$. If a finite-volume scheme using the single-stage Euler explicit time-integration scheme is devised that uses degree- $(k-1)$ reconstruction ($k \geq 2$) for the weights and degree-1 reconstruction for the abscissas at the faces $i-1/2$ and $i+1/2$, the non-negativity of the updated distribution function (3.17) in the i^{th} cell can always be guaranteed under an explicit constraint on the time-step size ($\Delta t \in \mathbb{R}^+$).*

Proof. *Using degree-1 reconstruction, the terms in (3.24) involving abscissas can be written as*

$$\begin{aligned} \frac{\partial \delta(b - B_{\alpha})}{\partial x} \Big|_{i+1/2}^n &= \frac{1}{\Delta x} [\delta(b - \bar{B}_{\alpha,i+1}^n) - \delta(b - \bar{B}_{\alpha,i}^n)] \quad \text{and} \\ \delta(b - B_{\alpha}) \Big|_{i+1/2}^n &= \frac{1}{2} [\delta(b - \bar{B}_{\alpha,i+1}^n) + \delta(b - \bar{B}_{\alpha,i}^n)]. \end{aligned} \quad (3.25)$$

Putting (3.25) in (3.24) gives

$$\frac{\partial f}{\partial x} \Big|_{i+1/2}^n = \sum_{\alpha=1}^{\beta} \left\{ \left[\frac{1}{2} \frac{\partial w_{\alpha}}{\partial x} \Big|_{i+1/2}^n - \frac{w_{\alpha,i+1/2}^n}{\Delta x} \right] \delta(b - \bar{B}_{\alpha,i}^n) + \left[\frac{1}{2} \frac{\partial w_{\alpha}}{\partial x} \Big|_{i+1/2}^n + \frac{w_{\alpha,i+1/2}^n}{\Delta x} \right] \delta(b - \bar{B}_{\alpha,i+1}^n) \right\} \quad (3.26)$$

Substituting this into (3.17) and simplifying, an equation for the update of f can be obtained:

$$\begin{aligned} \bar{f}_i^{n+1} &= \sum_{\alpha=1}^{\beta} \left\{ \left[\bar{w}_{\alpha,i}^n + \mu(b) \frac{\Delta t}{\Delta x} \left(-\frac{w_{\alpha,i+1/2}^n}{\Delta x} + \frac{1}{2} \frac{\partial w_{\alpha}}{\partial x} \Big|_{i+1/2}^n - \frac{w_{\alpha,i-1/2}^n}{\Delta x} - \frac{1}{2} \frac{\partial w_{\alpha}}{\partial x} \Big|_{i-1/2}^n \right) \right] \delta(b - \bar{B}_{\alpha,i}^n) \right. \\ &\quad + \mu(b) \frac{\Delta t}{\Delta x} \left[\frac{w_{\alpha,i-1/2}^n}{\Delta x} - \frac{1}{2} \frac{\partial w_{\alpha}}{\partial x} \Big|_{i-1/2}^n \right] \delta(b - \bar{B}_{\alpha,i-1}^n) \\ &\quad \left. + \mu(b) \frac{\Delta t}{\Delta x} \left[\frac{w_{\alpha,i+1/2}^n}{\Delta x} + \frac{1}{2} \frac{\partial w_{\alpha}}{\partial x} \Big|_{i+1/2}^n \right] \delta(b - \bar{B}_{\alpha,i+1}^n) \right\}. \end{aligned} \quad (3.27)$$

If $w_{\alpha,i-1/2}^n - \Delta x/2 \partial w_{\alpha}/\partial x|_{i-1/2}^n \geq 0$ and $w_{\alpha,i+1/2}^n + \Delta x/2 \partial w_{\alpha}/\partial x|_{i+1/2}^n \geq 0 \forall \alpha$ then the last two terms on the right side are always non-negative. If $\bar{w}_{\alpha,i}^n > 0 \forall \alpha$, one can always choose a small enough time-step size that will make the first term on the right side non-negative. The value of this time-step size, $\Delta t \in \mathbb{R}^+$, for guaranteeing the realizability of \bar{f}_i^{n+1} can be written

as

$$\Delta t = \min_{\alpha \in \{1, 2, \dots, \beta\}} \left[\frac{\bar{w}_{\alpha, i}^n \Delta x^2}{\mu(\bar{B}_{\alpha, i}^n) \max \left(w_{\alpha, i+1/2}^n - \frac{\Delta x}{2} \frac{\partial w_{\alpha}}{\partial x} \Big|_{i+1/2}^n + w_{\alpha, i-1/2}^n + \frac{\Delta x}{2} \frac{\partial w_{\alpha}}{\partial x} \Big|_{i-1/2}^n, 0 \right)} \right]. \quad (3.28)$$

This concludes the proof. \square

Irrespective of the degree of reconstruction polynomial used for the weights, the new scheme always uses degree-1 reconstruction for the abscissas. For example, the degree- $(k-1)$ reconstruction ($k \geq 2$) for the weights can be combined with the degree-1 reconstruction for the abscissas. Due to the use of a lower degree polynomial for the abscissas, this scheme will be called the *quasi- k^{th}* -order scheme. The realizability of this new scheme is guaranteed by the constraints also known as the realizability conditions. These realizability conditions are discussed below in greater detail. The new schemes have two advantages over the schemes based on the reconstruction of moments. As shown earlier, any scheme based on the reconstruction of moments can be at most second-order accurate. Realizability cannot be guaranteed for a higher than second-order accurate scheme based on the reconstruction of moments. Hence, if one wants to use the moment-based reconstruction, second-order accuracy is the best that can be achieved for any class of problems. However, the proposed *quasi- k^{th}* -order scheme ($k > 2$) will always perform better than the second-order scheme for any general problem and for a special class of problems where the abscissas are constant or linearly varying, the formal order of accuracy equal to k will be achieved. This is a considerable improvement over the second-order moment-based reconstruction scheme.

3.3.2 Consistency

The 2nd-order version of the new scheme should be consistent with the 2nd-order scheme based on the moment reconstruction. The 2nd-order version corresponds to using the degree-1 reconstruction for weights:

$$\frac{\partial w_{\alpha}}{\partial x} \Big|_{i+1/2}^n = \frac{1}{\Delta x} [\bar{w}_{\alpha, i+1}^n - \bar{w}_{\alpha, i}^n] \quad \text{and} \quad w_{\alpha, i+1/2}^n = \frac{1}{2} [\bar{w}_{\alpha, i+1}^n + \bar{w}_{\alpha, i}^n] \quad \forall \alpha. \quad (3.29)$$

Putting these into (3.27) gives

$$\begin{aligned}
\bar{f}_i^{n+1} &= \sum_{\alpha=1}^N \left\{ \left[1 - 2\mu(b) \frac{\Delta t}{\Delta x^2} \right] \bar{w}_{\alpha,i}^n \delta(b - \bar{B}_{\alpha,i}^n) + \mu(b) \frac{\Delta t}{\Delta x^2} \bar{w}_{\alpha,i-1}^n \delta(b - \bar{B}_{\alpha,i-1}^n) \right. \\
&\quad \left. + \mu(b) \frac{\Delta t}{\Delta x^2} \bar{w}_{\alpha,i+1}^n \delta(b - \bar{B}_{\alpha,i+1}^n) \right\} \\
&= \left[1 - 2\mu(b) \frac{\Delta t}{\Delta x^2} \right] \bar{f}_i^n + \mu(b) \frac{\Delta t}{\Delta x^2} [\bar{f}_{i+1}^n + \bar{f}_{i-1}^n]
\end{aligned} \tag{3.30}$$

This is exactly same as the updated distribution function for the 2nd-order scheme based on the reconstruction of moments. This means that the 2nd-order version of the new scheme is exactly same as the 2nd-order scheme based on the moment reconstruction. Hence, the new scheme is consistent. For the one-dimensional cases, the *quasi*-2nd-order scheme will be simply referred to as the 2nd-order scheme.

3.3.3 Realizability conditions

The above theorem implies that if the special reconstruction is used, a set of four conditions need to be satisfied simultaneously to guarantee realizability in the i^{th} cell:

$$\bar{w}_{\alpha,i}^n > 0, \tag{3.31}$$

$$w_{\alpha,i-1/2}^n - \frac{\Delta x}{2} \frac{\partial w_{\alpha}}{\partial x} \Big|_{i-1/2}^n \geq 0, \tag{3.32}$$

$$w_{\alpha,i+1/2}^n + \frac{\Delta x}{2} \frac{\partial w_{\alpha}}{\partial x} \Big|_{i+1/2}^n \geq 0, \tag{3.33}$$

$$\bar{w}_{\alpha,i}^n + \mu(\bar{B}_{\alpha,i}^n) \frac{\Delta t}{\Delta x^2} \left[-w_{\alpha,i+1/2}^n + \frac{\Delta x}{2} \frac{\partial w_{\alpha}}{\partial x} \Big|_{i+1/2}^n - w_{\alpha,i-1/2}^n - \frac{\Delta x}{2} \frac{\partial w_{\alpha}}{\partial x} \Big|_{i-1/2}^n \right] \geq 0 \quad \forall \alpha. \tag{3.34}$$

The last condition (3.34) is the same as (3.28). The first condition (3.31) is needed because if $\bar{w}_{\alpha,i}^n = 0$ for some α , then it may not be possible to satisfy the last condition (3.34) for that α . These four conditions are called the realizability conditions. They guarantee the realizability of the moments in the i^{th} cell. Next the severity of these realizability conditions is discussed.

3.3.3.1 Second-order scheme

It is interesting to see that for the 2nd-order scheme

$$w_{\alpha,i-1/2}^n - \frac{\Delta x}{2} \frac{\partial w_{\alpha}}{\partial x} \Big|_{i-1/2}^n = \bar{w}_{\alpha,i-1}^n \geq 0 \quad \text{and} \quad w_{\alpha,i+1/2}^n + \frac{\Delta x}{2} \frac{\partial w_{\alpha}}{\partial x} \Big|_{i+1/2}^n = \bar{w}_{\alpha,i+1}^n \geq 0 \quad \forall \alpha. \tag{3.35}$$

Hence the conditions (3.32) and (3.33) are automatically satisfied. It is also interesting to see that condition (3.31) is not required. For the 2nd-order scheme, the last condition reduces to

$$\left[1 - 2\mu(\overline{B}_{\alpha,i}^n) \frac{\Delta t}{\Delta x^2}\right] \overline{w}_{\alpha,i}^n \geq 0 \quad \forall \alpha. \quad (3.36)$$

So, if $\overline{w}_{\alpha,i}^n = 0$ for some α , then the last condition is automatically satisfied for that α .

3.3.3.2 *Quasi-kth-order scheme* ($k > 2$)

When $k > 2$, for the *quasi-kth-order* scheme, all the four conditions need to be satisfied simultaneously in order to guarantee realizability. Only the last condition (3.34) has an adjustable parameter Δt . If the first condition (3.31) is satisfied, one can choose an appropriate value of the adjustable parameter Δt to satisfy the last condition (3.34). However, Δt does not appear in the conditions (3.31), (3.32) and (3.33). Hence, whether or not the first three conditions are satisfied depends upon the problem. If any of the first three conditions is not satisfied for a particular α , a lower order scheme is used for that α . However, a detailed look at these conditions can help in understanding that they are not too restrictive.

If $\partial w_{\alpha}/\partial x|_{i-1/2}^n \leq 0$, (3.32) will always be guaranteed. Problem may occur only if $\partial w_{\alpha}/\partial x|_{i-1/2}^n > 0$. It is easy to see that $w_{\alpha,i-1/2}^n - \Delta x/2 \partial w_{\alpha}/\partial x|_{i-1/2}^n$ is an approximation to $\overline{w}_{\alpha,i-1}^n$. Similarly, if $\partial w_{\alpha}/\partial x|_{i+1/2}^n \geq 0$, (3.33) will always be guaranteed. This condition may not be satisfied only if $\partial w_{\alpha}/\partial x|_{i+1/2}^n < 0$. Again it is evident that $w_{\alpha,i+1/2}^n + \Delta x/2 \partial w_{\alpha}/\partial x|_{i+1/2}^n$ is an approximation to $\overline{w}_{\alpha,i+1}^n$. So the conditions (3.31), (3.32) and (3.33) will almost always be satisfied simultaneously if the cell-averaged values of weights are not too close to zero. If the cell-averaged values of weights are almost null in some cells, these conditions may not be satisfied and a lower order scheme should be used for those cells. But this is not a very restrictive condition because using a lower order scheme for the cells with cell-averaged values of weights close to null does not have a large effect on the overall accuracy.

The diffusive flux for the new scheme can then be computed as

$$\begin{aligned}
\left. \frac{\partial S^p}{\partial x} \right|_{i+1/2}^n &= \int \mu(b) b^p \left. \frac{\partial f}{\partial x} \right|_{i+1/2}^n db \\
&= \sum_{\alpha=1}^{\beta} \int \mu(b) b^p \left\{ \left[\frac{1}{2} \left. \frac{\partial w_{\alpha}}{\partial x} \right|_{i+1/2}^n - \frac{w_{\alpha,i+1/2}^n}{\Delta x} \right] \delta(b - \overline{B}_{\alpha,i}^n) \right. \\
&\quad \left. + \left[\frac{1}{2} \left. \frac{\partial w_{\alpha}}{\partial x} \right|_{i+1/2}^n + \frac{w_{\alpha,i+1/2}^n}{\Delta x} \right] \delta(b - \overline{B}_{\alpha,i+1}^n) \right\} db \\
&= \sum_{\alpha=1}^{\beta} \left\{ \mu(\overline{B}_{\alpha,i}^n) \left[\frac{1}{2} \left. \frac{\partial w_{\alpha}}{\partial x} \right|_{i+1/2}^n - \frac{w_{\alpha,i+1/2}^n}{\Delta x} \right] (\overline{B}_{\alpha,i}^n)^p \right. \\
&\quad \left. + \mu(\overline{B}_{\alpha,i+1}^n) \left[\frac{1}{2} \left. \frac{\partial w_{\alpha}}{\partial x} \right|_{i+1/2}^n + \frac{w_{\alpha,i+1/2}^n}{\Delta x} \right] (\overline{B}_{\alpha,i+1}^n)^p \right\}.
\end{aligned} \tag{3.37}$$

The diffusive flux for the *quasi-k*th-order scheme can be obtained by inserting the expressions for the degree- $(k-1)$ reconstruction of weights and their derivatives into (3.37). When $k=2$, (3.29) can be used. For $k=4$, one can use

$$\begin{aligned}
\left. \frac{\partial w_{\alpha}}{\partial x} \right|_{i+1/2}^n &= \frac{1}{\Delta x} \left[\frac{1}{12} \overline{w}_{\alpha,i-1}^n - \frac{5}{4} \overline{w}_{\alpha,i}^n + \frac{5}{4} \overline{w}_{\alpha,i+1}^n - \frac{1}{12} \overline{w}_{\alpha,i+2}^n \right] \text{ and} \\
w_{\alpha,i+1/2}^n &= \left[-\frac{1}{12} \overline{w}_{\alpha,i-1}^n + \frac{7}{12} \overline{w}_{\alpha,i}^n + \frac{7}{12} \overline{w}_{\alpha,i+1}^n - \frac{1}{12} \overline{w}_{\alpha,i+2}^n \right] \forall \alpha.
\end{aligned} \tag{3.38}$$

3.3.4 Calculation of time-step size

The global time-step size (Δt) should satisfy both the CFL and the realizability criteria to guarantee stability and realizability simultaneously. Usually, the largest value of $\text{CFL} < 1/2$ that gives a stable solution is used to enforce the CFL criterion for the diffusion problems. The definition of the CFL for the diffusion problem varies, but a general form is

$$\text{CFL} = \text{diffusivity} \left(\frac{\Delta t}{(\text{cell length scale})^2} \right). \tag{3.39}$$

Let $\Delta t_{\text{CFL},i}$ and $\Delta t_{\text{realizable},i}$ be the time-step sizes in the i^{th} cell satisfying the CFL and realizability criteria, respectively. Suppose, the problem under consideration uses the *quasi-k*th-order finite-volume scheme. A value of the $\text{CFL} < 1/2$ is pre-specified and Δt is calculated as $\Delta t = \min_i (\Delta t_{\text{CFL},i})$. During each time step, this Δt is used as the global time-step size, and the realizability conditions corresponding to the *quasi-k*th-order finite-volume scheme are checked in each cell. For the cells in which the check succeeds, the degree- $(k-1)$ reconstruction

is used for the weights. And for the cells in which the check fails, successively lower degree reconstructions ($k-2, k-3, \dots, 1$) for the weights are tried. The first reconstruction that satisfies the corresponding realizability conditions is used.

3.4 Realizable schemes for multidimensional cases

The ideas explained above for the one-dimensional cases can also be applied to the multi-dimensional cases. For simplicity, in this section the framework will be extended to the 2-D cases, although similar framework can be developed for the 3-D cases as well. The framework will first be laid down for general unstructured meshes and then the special case of uniform Cartesian mesh will be discussed.

3.4.1 Unstructured mesh

The two-dimensional version of (3.1) with $f = f(b, x, y, t)$ and $\mu = \mu(b)$ can be written as

$$\frac{\partial f}{\partial t} = \mu \nabla \cdot (\nabla f), \quad (3.40)$$

where $\nabla = (\partial/\partial x)\hat{\mathbf{i}} + (\partial/\partial y)\hat{\mathbf{j}}$. The moment transport equations corresponding to (3.40) can be written as

$$\frac{\partial M^p}{\partial t} = \nabla \cdot (\nabla S^p) \quad \forall p, \quad (3.41)$$

where M^p and S^p are defined as in (3.4). Again QBMM is used to close the above system of moment transport equations. The distribution function is defined as in (3.5) with $w_\alpha \equiv w_\alpha(x, y, t)$ and $B_\alpha \equiv B_\alpha(x, y, t)$.

Consider a 2-D unstructured mesh. Let Ω_i and $\partial\Omega_i$ denote the i^{th} cell and its boundary respectively. Also let $e \in \partial\Omega_i$ be a face of the i^{th} cell, A_e be its area and $\hat{\mathbf{n}}_e = [n_{ex} \ n_{ey}]$ be the outward unit normal at this face. The finite-volume expression for the single-stage Euler explicit time-integration, analogous to (3.7) can be written as

$$\overline{M}_i^{p,n+1} = \overline{M}_i^{p,n} + \frac{\Delta t}{|\Omega|_i} \sum_{e \in \partial\Omega_i} \left\{ \nabla \hat{S}_e^{p,n} \cdot \hat{\mathbf{n}}_e A_e \right\}, \quad (3.42)$$

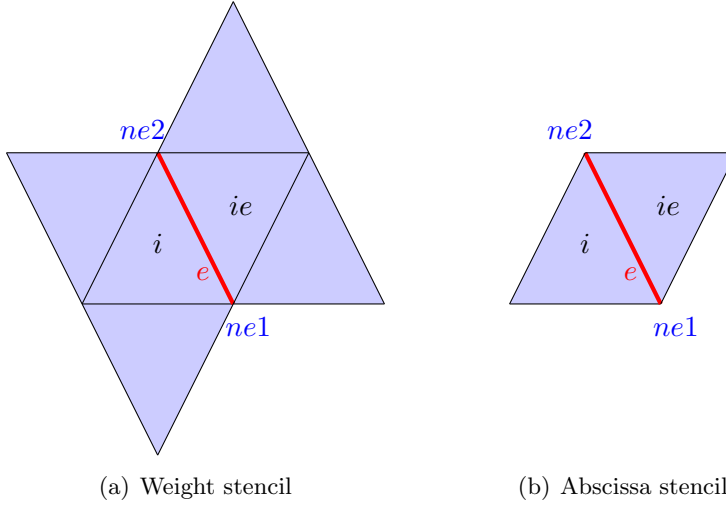


Figure 3.1 Second-order reconstruction stencils for the terms involving weights and abscissas at the face e of an unstructured mesh.

where $|\Omega|_i$ denotes the volume of the i^{th} cell. As earlier, the variables with overbars denote the cell-averaged values. The capped variables denote the face-averaged values. For example,

$$\nabla \hat{S}_e^{p,n} = \frac{1}{A_e} \int_e \nabla S^{p,n} dA \quad (3.43)$$

represents the face-averaged value of the moment gradient ($\nabla S^{p,n}$) on face e . Using an appropriate number (N_q) of Gaussian-quadrature points for the integration on face e , the face-averaged value can be written as

$$\nabla \hat{S}_e^{p,n} = \sum_{l=1}^{N_q} \left\{ q_l \nabla S_{e,l}^{p,n} \right\}, \quad (3.44)$$

where q_l is the l^{th} Gaussian-quadrature weight and $\nabla S_{e,l}^{p,n}$ is the value of the gradient evaluated at l^{th} Gaussian-quadrature point on face e . Using (3.44), (3.42) becomes

$$\bar{M}_i^{p,n+1} = \bar{M}_i^{p,n} + \frac{\Delta t}{|\Omega|_i} \sum_{e \in \partial\Omega_i} \sum_{l=1}^{N_q} \left\{ q_l \nabla S_{e,l}^{p,n} \cdot \hat{\mathbf{n}}_e A_e \right\}. \quad (3.45)$$

The finite-volume expression in (3.45) can also be written as

$$\int b^p \left[\bar{f}_i^{n+1} = \bar{f}_i^n + \mu(b) \frac{\Delta t}{|\Omega|_i} \sum_{e \in \partial\Omega_i} \sum_{l=1}^{N_q} \left\{ q_l \nabla f_{e,l}^n \cdot \hat{\mathbf{n}}_e A_e \right\} \right] db, \quad (3.46)$$

which implies that the unique update of the distribution function is given by

$$\bar{f}_i^{n+1} = \bar{f}_i^n + \mu(b) \frac{\Delta t}{|\Omega|_i} \sum_{e \in \partial\Omega_i} \sum_{l=1}^{N_q} \{q_l \nabla f_{e,l}^n \cdot \hat{\mathbf{n}}_e A_e\}. \quad (3.47)$$

The gradient of the distribution function at the face quadrature points are computed using the chain rule:

$$\nabla f_{e,l}^n = \sum_{\alpha=1}^{\beta} \left[\nabla w_{\alpha}|_{e,l}^n \delta(b - B_{\alpha})|_{e,l}^n + w_{\alpha}|_{e,l}^n \nabla \delta(b - B_{\alpha})|_{e,l}^n \right]. \quad (3.48)$$

As mentioned earlier, reconstruction polynomial of any degree ≥ 1 can be used for the terms involving the weights. However, for the terms involving the abscissas, the degree-1 reconstruction should be used. Before moving any further, it is extremely important to stress upon the fact that the degree-1 reconstruction of abscissas at face e using any arbitrary stencil will not work. A special stencil involving only the two cells adjacent to face e should be used. Although this special stencil may lose second-order accuracy on highly skewed meshes, this is the only viable option to guarantee realizability. The degree-1 reconstruction for abscissas using least-squares approach should be completely avoided as it cannot guarantee realizability. Using the values in the two cells adjacent to the face e , the terms involving abscissas in (3.48) can be written as

$$\begin{aligned} \delta(b - B_{\alpha})|_{e,l}^n &= \frac{1}{2} [\delta(b - \bar{B}_{\alpha,ie}^n) + \delta(b - \bar{B}_{\alpha,i}^n)] \quad \text{and} \\ \nabla \delta(b - B_{\alpha})|_{e,l}^n &= \frac{[\delta(b - \bar{B}_{\alpha,ie}^n) - \delta(b - \bar{B}_{\alpha,i}^n)]}{|\mathbf{r}_{ie} - \mathbf{r}_i|^2} (\mathbf{r}_{ie} - \mathbf{r}_i). \end{aligned} \quad (3.49)$$

In (3.49), ie denotes the neighbor of the i^{th} cell, adjacent to face e . Also, \mathbf{r}_i and \mathbf{r}_{ie} denote the cell-center position vectors of the i^{th} cell and its neighbor respectively. Note that the expressions in (3.49) will be second-order accurate only if the mesh-skewness is small in magnitude. If the mesh is considerably skewed, the accuracy will degrade. But this is the best that can be done to guarantee realizability. Putting (3.49) in (3.48) gives

$$\nabla f_{e,l}^n = \sum_{\alpha=1}^{\beta} \left\{ \nabla w_{\alpha}|_{e,l}^n \frac{1}{2} [\delta(b - \bar{B}_{\alpha,ie}^n) + \delta(b - \bar{B}_{\alpha,i}^n)] + w_{\alpha}|_{e,l}^n \frac{[\delta(b - \bar{B}_{\alpha,ie}^n) - \delta(b - \bar{B}_{\alpha,i}^n)]}{|\mathbf{r}_{ie} - \mathbf{r}_i|^2} (\mathbf{r}_{ie} - \mathbf{r}_i) \right\}. \quad (3.50)$$

Using this, the updated distribution function can be written as

$$\begin{aligned} \bar{f}_i^{n+1} &= \sum_{\alpha=1}^{\beta} \left\{ \bar{w}_{\alpha,i}^n + \mu(b) \frac{\Delta t}{|\Omega|_i} \sum_{e \in \partial\Omega_i} \sum_{l=1}^{N_q} A_e q_l \left[\frac{1}{2} \nabla w_{\alpha|e,l}^n \cdot \hat{\mathbf{n}}_e - w_{\alpha|e,l}^n \frac{(\mathbf{r}_{ie} - \mathbf{r}_i) \cdot \hat{\mathbf{n}}_e}{|\mathbf{r}_{ie} - \mathbf{r}_i|^2} \right] \right\} \delta(b - \bar{B}_{\alpha,i}^n) \\ &+ \mu(b) \frac{\Delta t}{|\Omega|_i} \sum_{\alpha=1}^{\beta} \sum_{e \in \partial\Omega_i} \sum_{l=1}^{N_q} \left\{ A_e q_l \left[\frac{1}{2} \nabla w_{\alpha|e,l}^n \cdot \hat{\mathbf{n}}_e + w_{\alpha|e,l}^n \frac{(\mathbf{r}_{ie} - \mathbf{r}_i) \cdot \hat{\mathbf{n}}_e}{|\mathbf{r}_{ie} - \mathbf{r}_i|^2} \right] \right\} \delta(b - \bar{B}_{\alpha,ie}^n). \end{aligned} \quad (3.51)$$

This corresponds to the following realizability conditions:

$$\bar{w}_{\alpha,i}^n > 0, \quad (3.52)$$

$$w_{\alpha|e,l}^n + \frac{1}{2} \nabla w_{\alpha|e,l}^n \cdot \hat{\mathbf{n}}_e \frac{|\mathbf{r}_{ie} - \mathbf{r}_i|^2}{(\mathbf{r}_{ie} - \mathbf{r}_i) \cdot \hat{\mathbf{n}}_e} \geq 0, \quad (3.53)$$

$$\bar{w}_{\alpha,i}^n + \mu(\bar{B}_{\alpha,i}^n) \frac{\Delta t}{|\Omega|_i} \sum_{e \in \partial\Omega_i} \sum_{l=1}^{N_q} A_e q_l \left[\frac{1}{2} \nabla w_{\alpha|e,l}^n \cdot \hat{\mathbf{n}}_e - w_{\alpha|e,l}^n \frac{(\mathbf{r}_{ie} - \mathbf{r}_i) \cdot \hat{\mathbf{n}}_e}{|\mathbf{r}_{ie} - \mathbf{r}_i|^2} \right] \geq 0 \quad \forall \alpha. \quad (3.54)$$

The condition (3.53) must be satisfied for each face $e \in \partial\Omega_i$ individually.

For the unstructured meshes, using higher than degree-1 reconstruction is not advisable as it is memory intensive because of extra storage requirements for connectivity information and reconstruction parameters. Hence, in Sec. 3.5, numerical results on the unstructured mesh are presented only for the degree-1 reconstruction of weights. For the degree-1 reconstruction, $N_q = 1$ and the only quadrature point is located at the face center. A linear profile is reconstructed at the face for each weight. However, instead of reconstructing the linear profile at the face directly, linear profiles are reconstructed in the cells and then the information from the adjacent cells is used to compute the values of the weights and their derivatives at the faces. This is computationally more efficient on unstructured meshes. The values of the weights at the only quadrature point at the face e is given by a simple averaging of the values reconstructed from the adjacent cells:

$$w_{\alpha|e,l}^n = \frac{1}{2} [\bar{w}_{\alpha,i}^n + \nabla w_{\alpha|i}^n \cdot (\mathbf{r}_e - \mathbf{r}_i)] + \frac{1}{2} [\bar{w}_{\alpha,ie}^n + \nabla w_{\alpha|ie}^n \cdot (\mathbf{r}_e - \mathbf{r}_{ie})], \quad (3.55)$$

where $\mathbf{r}_e \equiv [x_e \ y_e]$ denotes the position vector of the face center. The gradients for the weights in (3.55) are computed at the cell centers using the least-squares reconstruction. For example,

the gradient at the cell center of the i^{th} cell is computed using

$$\nabla w_\alpha|_i^n = \left\{ \frac{\|dy, dy\| \|dx, dw_\alpha^n\| - \|dx, dy\| \|dy, dw_\alpha^n\|}{\|dx, dx\| \|dy, dy\| - \|dx, dy\| \|dx, dy\|} \right\} \hat{\mathbf{i}} + \left\{ \frac{\|dx, dx\| \|dy, dw_\alpha^n\| - \|dx, dy\| \|dx, dw_\alpha^n\|}{\|dx, dx\| \|dy, dy\| - \|dx, dy\| \|dx, dy\|} \right\} \hat{\mathbf{j}}, \quad (3.56)$$

where

$$\begin{aligned} \|dy, dy\| &= \sum_{e \in \partial\Omega_i} (y_{ie} - y_i)(y_{ie} - y_i), \\ \|dx, dx\| &= \sum_{e \in \partial\Omega_i} (x_{ie} - x_i)(x_{ie} - x_i), \\ \|dx, dy\| &= \sum_{e \in \partial\Omega_i} (x_{ie} - x_i)(y_{ie} - y_i), \\ \|dx, dw_\alpha^n\| &= \sum_{e \in \partial\Omega_i} (x_{ie} - x_i)(w_{\alpha,ie}^n - w_{\alpha,i}^n), \\ \|dy, dw_\alpha^n\| &= \sum_{e \in \partial\Omega_i} (y_{ie} - y_i)(w_{\alpha,ie}^n - w_{\alpha,i}^n). \end{aligned} \quad (3.57)$$

The gradients of the weights at the face center can be computed by simply averaging the gradients from the adjacent cell centers. However, a better option is to split the gradients into two contributions - tangential to the face ($\partial w_\alpha / \partial \tau$) and along the direction joining the two adjacent cell centers ($\partial w_\alpha / \partial \xi$). The two derivatives are computed differently and then added to give

$$\begin{aligned} \nabla w_\alpha|_e^n &= \frac{\partial w_\alpha}{\partial x} \Big|_e^n \hat{\mathbf{i}} + \frac{\partial w_\alpha}{\partial y} \Big|_e^n \hat{\mathbf{j}} \\ &= \frac{1}{\Delta_e} \left[\frac{\partial w_\alpha}{\partial \xi} \Big|_e^n \tau_{ey} - \frac{\partial w_\alpha}{\partial \tau} \Big|_e^n \xi_{ey} \right] \hat{\mathbf{i}} + \frac{1}{\Delta_e} \left[-\frac{\partial w_\alpha}{\partial \xi} \Big|_e^n \tau_{ex} + \frac{\partial w_\alpha}{\partial \tau} \Big|_e^n \xi_{ex} \right] \hat{\mathbf{j}}, \end{aligned} \quad (3.58)$$

where

$$\frac{\partial w_\alpha}{\partial \xi} \Big|_e^n = \frac{\bar{w}_{\alpha,ie}^n - \bar{w}_{\alpha,i}^n}{|\mathbf{r}_{ie} - \mathbf{r}_i|}, \quad \frac{\partial w_\alpha}{\partial \tau} \Big|_e^n = \frac{1}{2} (\nabla w_\alpha|_i^n + \nabla w_\alpha|_{ie}^n) \cdot \hat{\boldsymbol{\tau}}_e, \quad (3.59)$$

and

$$\Delta_e = (\xi_{ex} \tau_{ey} - \xi_{ey} \tau_{ex}), \quad \hat{\boldsymbol{\xi}}_e \equiv [\xi_{ex} \ \xi_{ey}] = \frac{\mathbf{r}_{ie} - \mathbf{r}_i}{|\mathbf{r}_{ie} - \mathbf{r}_i|}, \quad \hat{\boldsymbol{\tau}}_e \equiv [\tau_{ex} \ \tau_{ey}] = \frac{\mathbf{r}_{ne2} - \mathbf{r}_{ne1}}{|\mathbf{r}_{ne2} - \mathbf{r}_{ne1}|}. \quad (3.60)$$

In (3.60), \mathbf{r}_{ne1} and \mathbf{r}_{ne2} denote the position vectors of the two nodes connected to the face e . It is worth reiterating that although both the weights and abscissas use the degree-1 reconstruction, each of them uses a different stencil. Figure 3.1 shows the different stencils used for the degree-1 reconstruction of the weights and abscissas at face e . It is very important to remember that

regardless of the stencil used for the weights, the stencil for the abscissas should only include the two cells adjacent to the face under consideration.

Before moving further, it is worth discussing the second-order scheme using moment-based reconstruction on unstructured meshes. For the second-order moment-based reconstruction, values of the moment gradients (∇S^p) have to be computed at the face centers. There are two ways to compute these gradients. One approach is to follow the reconstruction of weights in (3.58). This approach inherently uses the stencil shown in Figure 3.1(a) for both the weights and abscissas. However, as mentioned earlier, any reconstruction at a face that uses cells other than the adjacent ones will never guarantee realizability. Hence, following the approach in (3.58) is not a viable option. Another approach is to follow the reconstruction of abscissas in the second equation of (3.49). This approach inherently uses the stencil shown in Figure 3.1(b) for both the weights and abscissas. This leads to a realizable second-order scheme based on moment reconstruction. As mentioned earlier any reconstruction using this stencil will lose accuracy when mesh-skewness is not negligible. However, this is the only viable option for the second-order moment-based reconstruction to be realizable. Note that the new realizable scheme, presented above, based on the reconstruction of weights and abscissas will always perform better than the second-order moment-based reconstruction as it decouples the reconstruction of weights from the reconstruction of abscissas, thereby allowing the usage of a better stencil for the terms involving weights.

3.4.2 Uniform Cartesian mesh

Unlike the unstructured mesh, using a higher than degree-1 reconstruction is feasible for the Cartesian mesh as the connectivity information is readily available through the cell indices. All the analysis done above for the unstructured mesh can also be applied for the Cartesian mesh with some minor notational changes. Only the case of uniform Cartesian mesh with the same cell size (Δs) along X - and Y -directions is discussed here. Each cell is identified by a pair of indices (i, j) . The right and left faces of the cell (i, j) are denoted by $(i + 1/2, j)$ and $(i - 1/2, j)$ respectively while its top and bottom faces are denoted by $(i, j + 1/2)$ and $(i, j - 1/2)$ respectively. For the uniform Cartesian mesh, one dimensional schemes can be applied direction

by direction and only one quadrature point is needed at each face. The moments are updated as

$$\overline{M}_{i,j}^{p,n+1} = \overline{M}_{i,j}^{p,n} + \frac{\Delta t}{\Delta s} \left\{ \frac{\partial S^p}{\partial x} \Big|_{i+\frac{1}{2},j}^n + \frac{\partial S^p}{\partial y} \Big|_{i,j+\frac{1}{2}}^n - \frac{\partial S^p}{\partial x} \Big|_{i-\frac{1}{2},j}^n - \frac{\partial S^p}{\partial y} \Big|_{i,j-\frac{1}{2}}^n \right\} \quad (3.61)$$

and the derivatives at the face centers are computed using the chain rule:

$$\begin{aligned} \frac{\partial S^p}{\partial x} \Big|_{i+\frac{1}{2},j}^n &= \int \mu(b) b^p \frac{\partial f}{\partial x} \Big|_{i+\frac{1}{2},j}^n db \\ &= \int \mu(b) b^p \sum_{\alpha=1}^{\beta} \left[\frac{\partial w_{\alpha}}{\partial x} \Big|_{i+\frac{1}{2},j}^n \delta(b - B_{\alpha}) \Big|_{i+\frac{1}{2},j}^n + w_{\alpha} \Big|_{i+\frac{1}{2},j}^n \frac{\partial \delta(b - B_{\alpha})}{\partial x} \Big|_{i+\frac{1}{2},j}^n \right] db. \end{aligned} \quad (3.62)$$

The terms involving abscissas use degree-1 reconstruction and are given by

$$\begin{aligned} \delta(b - B_{\alpha}) \Big|_{i+\frac{1}{2},j}^n &= \frac{\delta(b - \overline{B}_{\alpha,i+1,j}^n) + \delta(b - \overline{B}_{\alpha,i,j}^n)}{2}, \\ \frac{\partial \delta(b - B_{\alpha})}{\partial x} \Big|_{i+\frac{1}{2},j}^n &= \frac{\delta(b - \overline{B}_{\alpha,i+1,j}^n) - \delta(b - \overline{B}_{\alpha,i,j}^n)}{\Delta s}. \end{aligned} \quad (3.63)$$

For the terms involving weights, reconstruction polynomial of degree ≥ 1 can be used. For example, for the degree-3 reconstruction of weights, formula analogous to (3.38) can be applied direction by direction. Figure 3.2 shows the stencils used for the *quasi*-4th-order scheme on uniform Cartesian mesh. The realizability conditions can be written as

$$\overline{w}_{\alpha,i,j}^n > 0, \quad (3.64)$$

$$\begin{aligned} w_{\alpha} \Big|_{i+\frac{1}{2},j}^n + \frac{\Delta s}{2} \frac{\partial w_{\alpha}}{\partial x} \Big|_{i+\frac{1}{2},j}^n &\geq 0, & w_{\alpha} \Big|_{i,j+\frac{1}{2}}^n + \frac{\Delta s}{2} \frac{\partial w_{\alpha}}{\partial y} \Big|_{i,j+\frac{1}{2}}^n &\geq 0, \\ w_{\alpha} \Big|_{i-\frac{1}{2},j}^n - \frac{\Delta s}{2} \frac{\partial w_{\alpha}}{\partial x} \Big|_{i-\frac{1}{2},j}^n &\geq 0, & w_{\alpha} \Big|_{i,j-\frac{1}{2}}^n - \frac{\Delta s}{2} \frac{\partial w_{\alpha}}{\partial y} \Big|_{i,j-\frac{1}{2}}^n &\geq 0, \end{aligned} \quad (3.65)$$

$$\begin{aligned} \overline{w}_{\alpha,i,j}^n + \mu(\overline{B}_{\alpha,i,j}^n) \frac{\Delta t}{\Delta s^2} &\left[\left\{ \frac{\Delta s}{2} \frac{\partial w_{\alpha}}{\partial x} \Big|_{i+\frac{1}{2},j}^n - w_{\alpha} \Big|_{i+\frac{1}{2},j}^n \right\} + \left\{ \frac{\Delta s}{2} \frac{\partial w_{\alpha}}{\partial y} \Big|_{i,j+\frac{1}{2}}^n - w_{\alpha} \Big|_{i,j+\frac{1}{2}}^n \right\} - \right. \\ &\left. \left\{ \frac{\Delta s}{2} \frac{\partial w_{\alpha}}{\partial x} \Big|_{i-\frac{1}{2},j}^n + w_{\alpha} \Big|_{i-\frac{1}{2},j}^n \right\} - \left\{ \frac{\Delta s}{2} \frac{\partial w_{\alpha}}{\partial y} \Big|_{i,j-\frac{1}{2}}^n + w_{\alpha} \Big|_{i,j-\frac{1}{2}}^n \right\} \right] \geq 0 \quad \forall \alpha. \end{aligned} \quad (3.66)$$

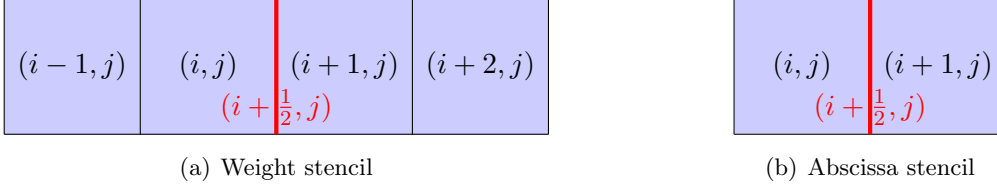


Figure 3.2 *Quasi-fourth-order reconstruction stencils for the terms involving weights and abscissas at the face $(i + \frac{1}{2}, j)$ of a uniform Cartesian mesh.*

3.5 Numerical results

In this section, numerical results are presented for 1-D and 2-D cases. For the 1-D cases, problems with both constant and non-linearly varying abscissas are considered. It is shown that for the problems with constant abscissas, formal high-order of accuracy is achieved. For the problems with non-linearly varying abscissas, formal high-order of accuracy cannot be achieved but these schemes still perform much better than the second-order moment-based reconstruction scheme. Note that the direct extension of the moment-based reconstruction to higher than second-order is not possible due to the non-realizability problem. For the 2-D cases, only the problems with constant abscissas are considered and results are presented for an unstructured triangular mesh and a uniform Cartesian mesh. Two-stage second-order RK2SSP time-integration scheme [42] is used for all the cases. For all the problems, the diffusivity coefficient is given by $\mu(b) = 0.1/(b + 1.0)$. The first three problems are one-dimensional with domain defined by $x \in [-3, 3]$ while the last two problems are two-dimensional with the domain defined by $(x, y) \in [-3, 3] \times [-3, 3]$.

3.5.1 Problem I

This is a two-node quadrature case with constant abscissas. The moment transport equations for the first four moments (M^0, M^1, M^2, M^3) are solved. The analytical solution is given

by

$$\begin{aligned} w_1(x, t) &= 0.1 + \sqrt{\frac{t_0}{t}} \exp\left(\frac{-(x + 1.0)^2}{4\mu(B_1)t}\right), & B_1(x, t) &= 1.0, \\ w_2(x, t) &= 0.2 + \sqrt{\frac{t_0}{t}} \exp\left(\frac{-(x - 1.0)^2}{4\mu(B_2)t}\right), & B_2(x, t) &= 1.5, \end{aligned} \quad (3.67)$$

where $t_0 = 1.0$. The *quasi-4th*-order scheme is used to solve this problem. Table 3.1 shows the orders of accuracy for the four moments based on the L_1 errors. Note that the numerical orders converge towards the formal order.

Table 3.1 Orders of accuracy based on L_1 errors for Problem I.

Grid size	M^0	M^1	M^2	M^3
40	-	-	-	-
80	3.89	3.89	3.89	3.89
160	3.97	3.97	3.97	3.97
320	3.98	3.99	3.99	3.99

3.5.2 Problem II

The problem mentioned in the previous section (Sec. 3.5.1) has two distinct abscissas and hence can be solved exactly (minus the errors introduced by the numerical scheme) using two-node quadrature. Here, one-node quadrature is used to solve the same problem and the results for the second-order moment-based reconstruction scheme are compared to those obtained from the *quasi-4th*-order scheme. The abscissa is not constant in this problem. It varies non-linearly between B_1 and B_2 in (3.67). For one-node quadrature, two moment (M^0, M^1) are tracked. The initial values of the two moments are computed using (3.67). Errors are computed against a reference solution that is obtained using the second-order moment-based reconstruction on a fine mesh with 2400 cells. Figure 3.3 compares the L_1 errors in M^0 and M^1 for the two schemes while Table 3.2 shows the corresponding orders of accuracy obtained by the two schemes. Clearly, the *quasi-4th*-order scheme performs much better compared to the second-order moment-based reconstruction scheme even for the variable abscissa case. On coarse meshes, the *quasi-4th*-order scheme gives numerical orders of accuracy close to 3 and reduces to 2 as the mesh is refined. However on the finest mesh, the errors obtained by the

quasi-4th-order scheme are still an order of magnitude lower than those obtained by the second-order moment-based reconstruction scheme. As mentioned earlier, the reference solution is computed on a fine mesh using the second-order moment-based reconstruction scheme. Hence, the reduction in order of accuracy of the *quasi-4th*-order scheme may be due to the reason that the numerical solution is already close to the reference solution and temporal errors start dominating

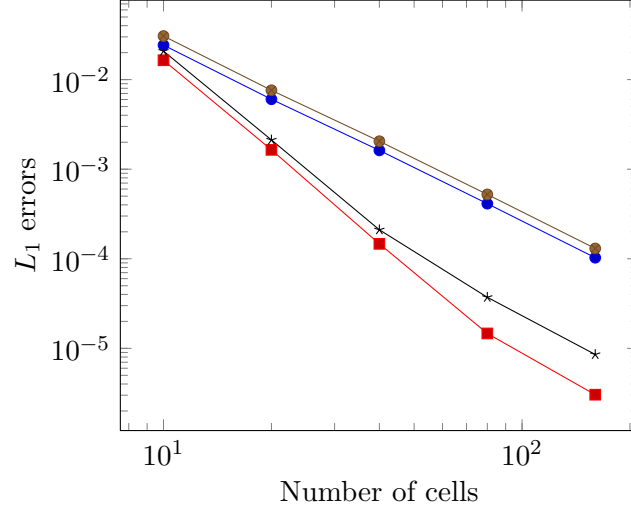


Figure 3.3 L_1 errors for Problem II: M^0 {2nd-order} (—●—), M^0 {quasi-4th-order} (—■—), M^1 {2nd-order} (—●—), M^1 {quasi-4th-order} (—*—).

Table 3.2 Orders of accuracy based on L_1 errors for Problem II.

Grid size	Second-order scheme		<i>Quasi-fourth-order</i> scheme	
	M^0	M^1	M^0	M^1
10	-	-	-	-
20	2.01	2.01	3.32	3.29
40	1.90	1.89	3.48	3.33
80	1.98	1.97	3.29	2.50
160	2.00	2.00	2.30	2.11

3.5.3 Problem III

This problem also demonstrates the performance of the new realizable schemes when abscissas are not constant. However, this problem uses EQMOM. As mentioned earlier, the new *quasi*-high-order schemes can be more efficient if the abscissas are nearly constant. When very few abscissas are used, the spatial variation in each abscissa from one cell to another may be large. However, if the number of abscissas is increased, the spatial variation in each abscissa will be relatively smaller. This is where EQMOM helps. Using EQMOM, one can increase the number of abscissas without increasing the number of tracked moments. In EQMOM, the number of primary quadrature nodes decides the number of moments tracked and the number of secondary quadrature nodes decides the number of abscissas resolved. The number of secondary quadrature nodes can be increased independent of the number of primary quadrature nodes, thereby reducing the spatial variation of each abscissa over a range of cells. For this problem beta-EQMOM is used with 1 node for primary quadrature and three different number of nodes (2, 10 and 50) for secondary quadrature. The beta-EQMOM assumes that at each time step the distribution function can be written in the form of a beta distribution. The shape parameters of this beta distribution are obtained using the primary quadrature and then the secondary quadrature is used to express the distribution function in the Dirac delta representation with 2, 10 and 50 nodes respectively. More details about EQMOM can be found in [127]. The first three moments (M^0, M^1, M^2) are tracked and their initial values are given by

$$M^0(x, 0) = 1.0, M^1(x, 0) = \xi(x), M^2(x, 0) = \frac{1}{2} ((\xi(x))^2 + \xi(x)) \text{ where } \xi(x) = \frac{1}{2} + \frac{1}{4} \sin\left(\frac{2\pi x}{3}\right). \quad (3.68)$$

These moments correspond to the initial beta distribution function given by

$$f(x, b, 0) = \frac{b^{\xi(x)-1} (1-b)^{-\xi(x)}}{B(\xi(x), 1-\xi(x))}, \quad (3.69)$$

where $B(\xi(x), 1-\xi(x))$ denotes the beta function. For this problem, the function $\xi(x)$ denotes the initial variation of mean abscissa. Figure 3.4 compares the L_1 errors in M^0 , M^1 and M^2 for the two schemes while Table 3.3 shows the corresponding orders of accuracy obtained by the two schemes. For this problem, errors are computed against the reference solutions obtained using the second-order moment-based reconstruction on a fine mesh with 600 cells. The reference

Table 3.3 Orders of accuracy based on L_1 errors for Problem III.

Grid size	2 nd -order scheme			<i>Quasi-4th</i> -order scheme		
	M^0	M^1	M^2	M^0	M^1	M^2
2 nodes for secondary quadrature						
15	-	-	-	-	-	-
20	1.82	1.84	1.94	1.88	1.82	1.78
25	1.93	1.97	1.82	2.06	2.10	1.87
30	1.91	1.94	1.95	1.93	1.89	1.94
10 nodes for secondary quadrature						
15	-	-	-	-	-	-
20	1.83	1.84	1.95	2.67	2.80	3.03
25	1.91	1.95	1.84	2.59	2.95	2.76
30	1.90	1.94	1.97	1.97	2.45	2.65
50 nodes for secondary quadrature						
15	-	-	-	-	-	-
20	1.83	1.84	1.95	3.14	3.36	3.55
25	1.91	1.95	1.84	2.98	3.50	3.41
30	1.90	1.94	1.97	2.34	3.27	3.69

solutions for 2, 10 and 50 secondary quadrature nodes are different. Note that only first four cell resolutions are used in Table 3.3 as the solutions using *quasi-4th*-order have already converged to the reference solution. As the number of nodes for the secondary quadrature is increased, the error magnitude for the *quasi-4th*-order scheme decreases and the numerical order or accuracy improves. The *quasi-4th*-order always performs better than the second-order moment-based reconstruction scheme.

3.5.4 Problem IV

Table 3.4 Orders of accuracy based on L_1 errors for Problem IV.

Grid size	Moment-based				Weight/abscissa-based			
	M^0	M^1	M^2	M^3	M^0	M^1	M^2	M^3
3676	-	-	-	-	-	-	-	-
5700	0.38	0.25	0.13	0.02	1.35	1.56	1.75	1.91
8394	0.26	0.31	0.12	-0.01	1.63	1.60	1.57	1.54

This is a two-node quadrature case with constant abscissas. The moment transport equations for the first four moments (M^0, M^1, M^2, M^3) are solved on unstructured triangular meshes. The analytical solution is given by

$$\begin{aligned} w_1(x, y, t) &= 0.1 + \frac{t_0}{4\pi\mu(B_1)t} \exp\left(\frac{-(x+0.5)^2 - (y+0.5)^2}{4\mu(B_1)t}\right), & B_1(x, y, t) &= 1.0, \\ w_2(x, y, t) &= 0.2 + \frac{t_0}{4\pi\mu(B_2)t} \exp\left(\frac{-(x-0.5)^2 - (y-0.5)^2}{4\mu(B_2)t}\right), & B_2(x, y, t) &= 1.5, \end{aligned} \quad (3.70)$$

where $t_0 = 1.0$. The second-order schemes based on both the reconstruction of moments and the reconstruction of weights and abscissas is used to solve this problem. It is worth reiterating that the second-order scheme based on the reconstruction of moments uses the stencil shown in Figure 3.1(b) for both the weights and abscissas while the new second-order scheme decouples the reconstruction of weights and abscissas, thereby using the stencil shown in Figure 3.1(a) for weights and the one shown in Figure 3.1(b) for the abscissas. Figure 3.5 compares the L_1 errors in M^0, M^1, M^2 and M^3 for the two schemes while Table 3.4 shows the corresponding orders of accuracy obtained by the two schemes. None of the schemes achieve the formal order of accuracy equal to 2, but the scheme based on the reconstruction of weights and abscissas performs tremendously better compared to the one based on the reconstruction of moments. The combination of skewed cells and the stencil in Figure 3.1(b) for both the weights and abscissas proves to be disastrous for the moment-based reconstruction. It is not even first-order accurate. On the other hand, the stencil in Figure 3.1(a) for the weights, saves the day for the newly proposed scheme.

3.5.5 Problem V

Here, the problem described in the previous section (Sec. 3.5.4) is solved on a uniform Cartesian mesh using *quasi*-4th-order scheme. As the abscissas are constant, formal order of accuracy is achieved as shown in Table 3.5. On unstructured meshes, using a polynomial of degree higher than 1 is inefficient because the storage of connectivity information requires additional memory. However, as the connectivity information is readily available for Cartesian meshes, polynomial reconstruction of arbitrarily high degree can be used for the weights.

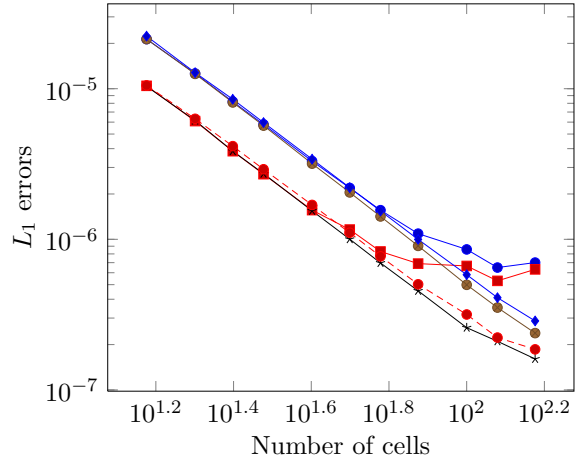
Table 3.5 Orders of accuracy based on L_1 errors for Problem V.

Grid size	M^0	M^1	M^2	M^3
20x20	-	-	-	-
40x40	3.56	3.55	3.55	3.55
80x80	3.84	3.84	3.84	3.84
160x160	3.92	3.92	3.92	3.92

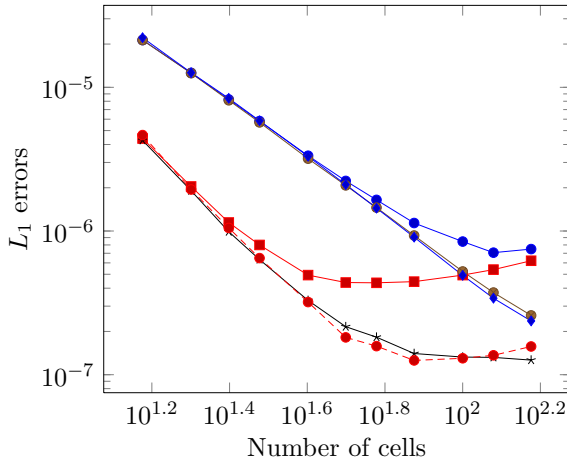
3.6 Conclusions

Hitherto, the moment-based reconstruction schemes were used with QBMM for diffusion problems without any proof of realizability. In the present work it has been shown that any scheme based on the reconstruction of moments can be at most second-order accurate. Realizability cannot be guaranteed for a higher than second-order scheme based on the reconstruction of moments. Hence, if one wants to use moment-based reconstruction, second-order accuracy is the best that can be achieved for any class of problems. For one-dimensional cases, it is also shown that the realizability condition for the second-order moment-based reconstruction scheme is same as the stability condition. In the past realizability problems have never been encountered with the second-order scheme based on the reconstruction of moments because the stability condition was always accounted for, thereby satisfying the realizability condition as well.

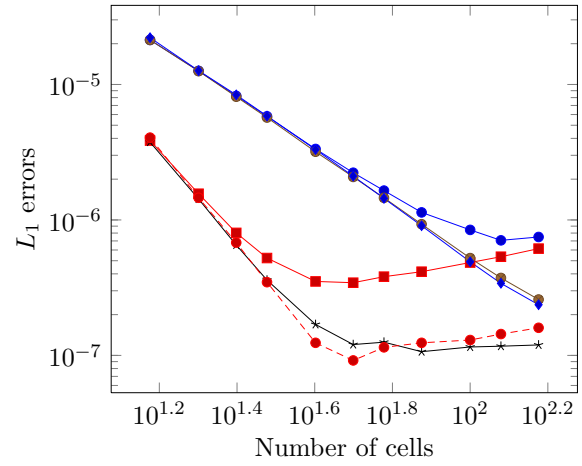
A new class of schemes based on the reconstruction of weights and abscissas is proposed. These schemes always guarantee realizability under an explicit constraint on the time-step size. According to the proposed idea, the *quasi- k^{th}* -order scheme uses degree- $(k-1)$ reconstruction for the weights and degree-1 reconstruction for the abscissas. The proposed *quasi- k^{th}* -order scheme ($k > 2$) always performs better than the second-order scheme for any general problem and for the special class of problems where the abscissas are constant or linearly varying, the formal order k is achieved. This is a considerable improvement over the second-order moment-based reconstruction scheme.



(a) 2 nodes for secondary quadrature



(b) 10 nodes for secondary quadrature



(c) 50 nodes for secondary quadrature

Figure 3.4 L_1 errors for Problem III: M^0 {2nd-order} (—●—), M^0 {quasi-4th-order} (—■—), M^1 {2nd-order} (—●—), M^1 {quasi-4th-order} (—*—), M^2 {2nd-order} (—●—), M^2 {quasi-4th-order} (—●—).

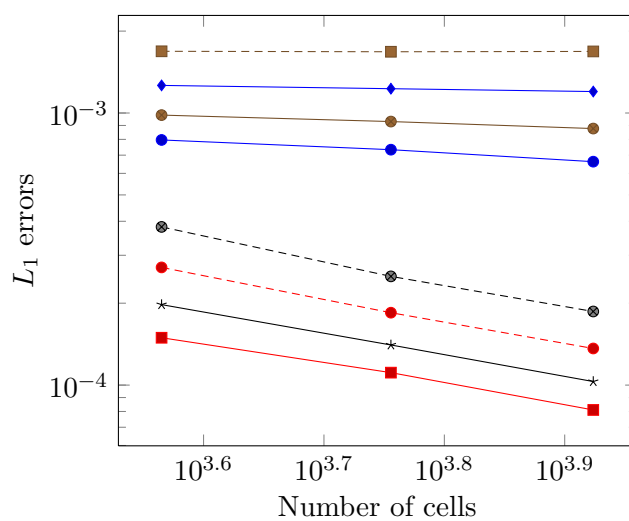


Figure 3.5 L_1 errors for Problem IV: M^0 {moment-based} ($- \bullet -$), M^0 {weight/abscissa-based} ($- \blacksquare -$), M^1 {moment-based} ($- \bullet -$), M^1 {weight/abscissa-based} ($- * -$), M^2 {moment-based} ($- \bullet -$), M^2 {weight/abscissa-based} ($- \bullet -$), M^3 {moment-based} ($- \blacksquare -$), M^3 {weight/abscissa-based} ($- \bullet -$).

CHAPTER 4. MODELING OF BUBBLE-COLUMN FLOWS WITH QUADRATURE-BASED MOMENT METHODS

A paper published in Chemical Engineering Science

Varun Vikas¹, C. Yuan, Z. J. Wang, Rodney O. Fox

Abstract

Bubble-column reactors are frequently employed in the biological, chemical and petrochemical industries. This paper presents a novel approach to model bubble-column flows using quadrature-based moment methods (QBMM²). A fully two-way coupled flow solver is developed that solves the incompressible Navier-Stokes equation for the liquid phase and moment transport equations for the dispersed bubble phase. The moment transport equations for the dispersed bubble phase are solved using a kinetic theory approach. Contributions from the liquid-phase pressure gradient, vorticity, drag, virtual mass and gravity are accounted for in the bubble-phase force balance. The solution algorithm and coupling procedure are described in detail, and results are presented for a 2-D bubble column with two different gas flow rates (1.6 and 8.0 l/min).

4.1 Introduction

Bubble-column reactors are widely used in the biological, chemical and petrochemical industries. The accurate design of these reactors depends largely on the complex fluid dynamics of gas-liquid two-phase flows that still remains inadequately understood. Modeling of the

¹Primary researcher and author.

²Throughout this chapter, QBMM refers to QMOM.

fluid dynamics of gas-liquid bubble columns is therefore a challenging task. There are two well-known approaches to model gas-liquid two-phase flows. One approach is based on the mixture formulation in which effective (transport) properties are used to describe the overall flow. This approach is relatively simple but cannot account for the detailed interactions between the two phases in an accurate manner. Another approach is to treat the two phases separately such that the dynamic interactions between the phases can be accounted for using a separate momentum balance for each phase. Within this approach, one can distinguish between Euler-Euler and Euler-Lagrange models. Euler-Euler models are based on the concept of inter-penetrating continua, while Euler-Lagrange models treat the liquid phase as a continuum and track each individual bubble using the Newtonian equations of motion containing correlations for the force terms acting on each bubble. Both Euler-Euler and Euler-Lagrange models have been used by researchers to model bubble-column flows. For example, Torvik & Svendsen [110], Ranade [88], Grienberger & Hofman [44], Sokolichin & Eigenberger [101], Hjertager & Morud [48] have used Euler-Euler gas-fluid models to simulate gas-liquid bubble columns, while Trapp & Mortensen [111], Lapin & Lubbert [58], Devanathan *et al.* [26], Delnoij *et al.* [22], Wu *et al.* [125] have used Euler-Lagrange models.

The closures used in Euler-Euler two-fluid models are obtained with strong assumptions on the nature of the flow, assuming that the phases can be described by a mean momentum equation with gradient-viscosity models. In the context of a kinetic theory description of the bubble phase, this type of model corresponds to considering a dispersed-phase Knudsen number (defined in Sec. 4.4.2) close to zero, meaning that the bubble velocity distribution function is determined by bubble-bubble interactions. This assumption leads to inconsistencies and erroneous or missing predictions of physical phenomena when these models are applied to dilute bubbly flows wherein bubble-bubble interactions are relatively small. For example, as shown in Passalacqua & Fox [80], it is not possible to obtain grid-independent solutions to Euler-Euler two-fluid models when the dispersed-phase Knudsen number is not small. On the other hand Euler-Lagrange methods, although more accurate, are still too expensive to be applied to real-life scenarios. In this work, a novel approach for modeling gas-liquid flows is presented using quadrature-based moment methods (QBMM) and a kinetic theory representation of the

bubble phase. Our model is based on an Euler-Euler approach in the sense that the bubble phase is treated as continuum, but it does not make assumptions of nearly equilibrium flows as done implicitly in two-fluid models. With QBMM, it is possible to resolve several velocities (depending upon the number of quadrature nodes used) in each control volume, thereby avoiding delta shocks and thus making it possible to attain a grid-independent solution to the moment transport equations [80]. The multi-velocity property lends a Lagrange essence to the QBMM approach. A fully two-way coupled solver that uses the incompressible Navier-Stokes equation for the liquid phase, and moment transport equations for the dispersed bubble phase is developed in this work. Contributions from liquid-phase pressure gradient, vorticity, drag, virtual mass and gravity are accounted for in the bubble-phase force balance. The solution algorithm and coupling procedure are described in detail, and results are presented for a 2-D bubble column at two different gas flow rates (1.6 and 8.0 l/min). For clarity, in this paper we describe a 2-D flow solver and corresponding results. The 3-D flow solver will be presented in future work.

The remainder of this paper is organized as follows. The bubbly flow model is described in Sec. 4.2. In Sec. 4.2.1, the liquid-phase governing equations are presented, while in Sec. 4.2.2 the bubble-phase governing equations are discussed. In Sec. 4.3, the numerical implementation of the bubbly flow model is described. Section 4.3.1 presents the solution strategy for the liquid-phase equations, while Sec. 4.3.2 does the same for the bubble-phase equations. Section 4.3.3 briefly discusses the coupling algorithm between the solvers for the individual phases. Finally, numerical results are presented in Sec. 4.4 for a 2-D bubble column, and a summary of major conclusions is given in Sec. 4.5.

4.2 Description of Model

In this section, we describe the bubbly flow model in its simplest form: constant density, monodisperse in a Newtonian liquid. Bubble-bubble interactions are not modeled as only dilute flows are considered. The liquid-phase governing equations are the same as those used in most Euler-Euler and Euler-Lagrange models, and thus will be presented without detailed discussion. In contrast, the dispersed bubble phase is described by a kinetic theory model,

which is similar, but not exactly the same, as the dispersed bubble model (DBM) used in Euler-Lagrange simulations [22]. We will thus provide more details on the bubble-phase model.

4.2.1 Liquid-phase governing equations

The behavior of the liquid phase is described by the classical continuity and momentum equations solved in multi-fluid models [27]. The liquid-phase continuity equation has the form

$$\frac{\partial}{\partial t} (\varepsilon_1 \rho_1) + \nabla \cdot (\varepsilon_1 \rho_1 \mathbf{U}_1) = 0, \quad (4.1)$$

and the liquid-phase momentum equation is given by

$$\frac{\partial}{\partial t} (\varepsilon_1 \rho_1 \mathbf{U}_1) + \nabla \cdot (\varepsilon_1 \rho_1 \mathbf{U}_1 \mathbf{U}_1) = \nabla \cdot (\varepsilon_1 \boldsymbol{\tau}) - \nabla p + \varepsilon_1 \rho_1 \mathbf{g} + \mathbf{M}_{1b}, \quad (4.2)$$

where ε_1 , ρ_1 , \mathbf{U}_1 , p are, respectively, the liquid-phase volume fraction, density, velocity and pressure, and \mathbf{M}_{1b} is the momentum-exchange term between the liquid and bubble phases (which includes the liquid-pressure force on the bubbles equal to $(1 - \varepsilon_1)\nabla p$). In this work, the liquid phase is treated as an incompressible fluid and hence ρ_1 is a constant. Also, the liquid phase is assumed to be Newtonian, and its stress tensor $\boldsymbol{\tau}$ is given by

$$\boldsymbol{\tau} = \mu_1 \left[\left(\nabla \mathbf{U}_1 + (\nabla \mathbf{U}_1)^T \right) - \frac{2}{3} (\nabla \cdot \mathbf{U}_1) \mathbf{I} \right], \quad (4.3)$$

where μ_1 is the liquid-phase dynamic viscosity, \mathbf{g} is the gravitational acceleration vector and \mathbf{I} is the unit tensor.

The models for the force terms appearing in \mathbf{M}_{1b} are discussed in Sec. 4.2.2. The reader should note that Eq. 4.1 is coupled to the bubble-phase governing equations through the constraint $\varepsilon_1 + \varepsilon_b = 1$, where ε_b is the bubble-phase volume fraction. Hence, the liquid-phase governing equations must be solved in a fully coupled manner with those for the bubble phase. Finally, we should note that the viscosity μ_1 appearing in Eq. 4.3 can be extended by adding to it a bubble-induced turbulent (BIT) viscosity [97] of the form $\mu_{bit} = C_{bit} \varepsilon_b \text{Re}_b \mu_1$ where the bubble Reynolds number is defined by

$$\text{Re}_b = \frac{\rho_1 d_b |\mathbf{U}_1 - \mathbf{U}_b|}{\mu_1},$$

U_b is the mean bubble velocity, and d_b is the bubble diameter. The BIT viscosity is the result of pseudo-turbulence in the liquid phase caused by the wakes behind rising bubbles [92]. C_{bit} is a constant of order one that depends on the bubble Reynolds number and on ε_b (e.g., as ε_b approaches its maximum value the bubble wakes are screened by neighboring bubbles so that C_{bit} decreases to zero – the simplest such model is $C_{\text{bit}} \propto \varepsilon_1$). In this work, we will neglect the BIT viscosity, but in most bubble-column flows $\text{Re}_b \gg 1$ so that finer grids are required to resolve the liquid-phase velocity when the BIT viscosity is neglected.

4.2.2 Bubble-phase governing equations

The bubble phase is described assuming that bubbles are smooth, monodisperse, non-coalescing spheres. Each bubble has its own velocity and position. As a consequence, the bubble-phase governing equation is represented by a kinetic equation for the bubble number density function $f(t, \mathbf{x}, \mathbf{v})$, defined so that $f d\mathbf{x} d\mathbf{v}$ is the average number of bubbles with velocity between \mathbf{v} and $\mathbf{v} + d\mathbf{v}$ and position between \mathbf{x} and $\mathbf{x} + d\mathbf{x}$, at time t . The general form of the kinetic equation is [17]

$$\frac{\partial f}{\partial t} + \mathbf{v} \cdot \frac{\partial f}{\partial \mathbf{x}} + \frac{\partial}{\partial \mathbf{v}} \cdot \left(f \frac{\mathbf{F}}{m_b} \right) = 0. \quad (4.4)$$

Note that the terms corresponding to bubble-bubble interactions have been omitted. In Eq. 4.4, \mathbf{F} is the force acting on each bubble of mass m_b , which includes the terms involving the force applied by the liquid phase and gravity. The terms involving the force applied by the liquid phase are computed using empirical relations obtained from DNS simulations. These empirical relations are discussed later. Some of the empirical relations depend on the volume fraction of the bubble phase, thereby making the above kinetic equation a complex-integro differential equation.

In comparison to the DBM used in some Euler-Lagrange simulations [22], the principle difference in the kinetic theory model in Eq. 4.4 is that the bubble-bubble interaction term is not modeled. In the DBM simulations of Delnoij *et al.* [22], finite-size bubbles are tracked and bubble-bubble interactions are treated as binary hard-sphere collisions. The bubble-bubble interactions are not dominant in the flows that we will consider here. Hence, neglecting the bubble-bubble interaction terms is reasonable.

The kinetic equation in Eq. 4.4 is coupled to the liquid-phase governing equations through the moments of f (e.g., the zero- and first-order moments). A direct solution of the kinetic equation to find f [8, 15] is prohibitively expensive because it would require the discretization of a seven dimensional space, in which three dimensions are the physical-space dimensions, three are the dimensions of the velocity phase space, and one is time. An alternative method to the direct discretization of Eq. 4.4 is represented by direct simulation Monte Carlo (DSMC) [10], which becomes expensive when the interaction time scale is small, limiting its application to relatively dilute flows. Another alternative, more convenient, approach is to consider a set of moments of the distribution function f [104], and track their evolution in space and time, instead of aiming at reconstructing the exact shape of f . This leads to an approximate solution of the kinetic equation, which is however satisfactory for many engineering applications, like the simulation of fluid-particle and gas-liquid flows. As mentioned earlier, it is the moments of f that are needed for coupling with liquid-phase model, so that the accuracy of the fully coupled model is not compromised by using moment methods.

In this work, the following set of ten moments up to the third order (in 2-D phase space) is considered:

$$\mathbf{W} = [M^0 \ M_1^1 \ M_2^1 \ M_{11}^2 \ M_{12}^2 \ M_{22}^2 \ M_{111}^3 \ M_{112}^3 \ M_{122}^3 \ M_{222}^3], \quad (4.5)$$

where the superscripts represent the order of the corresponding moment [33]. Each moment is defined through integrals of the distribution function as

$$\begin{aligned} M^0 &= \int f d\mathbf{v}, & M_i^1 &= \int v_i f d\mathbf{v}, \\ M_{ij}^2 &= \int v_i v_j f d\mathbf{v}, & M_{ijk}^3 &= \int v_i v_j v_k f d\mathbf{v}. \end{aligned} \quad (4.6)$$

Note that the bubble-phase volume fraction ε_b and mean bubble velocity \mathbf{U}_b are related to these moments by

$$\varepsilon_b = V_b M^0 \quad (4.7)$$

and

$$\rho_b \varepsilon_b U_{b,i} = m_b M_i^1, \quad (4.8)$$

where $m_b = \rho_b V_b$ is the mass of a bubble with density ρ_b and volume $V_b = \pi d_b^3/6$. In this work,

m_b is constant because d_b and ρ_b are constant. By definition, $\varepsilon_1 = 1 - \varepsilon_b$ and this relation must be accounted for when solving a fully coupled system for the liquid and bubble phases.

The application of the definition of the moments to both sides of Eq. 4.4 allows the moment transport equations to be derived. The set of ten transport equations, one for each moment in \mathbf{W} , is given by

$$\begin{aligned} \frac{\partial M^0}{\partial t} + \frac{\partial M_i^1}{\partial x_i} &= 0, \\ \frac{\partial M_i^1}{\partial t} + \frac{\partial M_{ij}^2}{\partial x_j} &= F_i^1, \\ \frac{\partial M_{ij}^2}{\partial t} + \frac{\partial M_{ijk}^3}{\partial x_k} &= F_{ij}^2, \\ \frac{\partial M_{ijk}^3}{\partial t} + \frac{\partial M_{ijkl}^4}{\partial x_l} &= F_{ijk}^3, \end{aligned} \tag{4.9}$$

where F_i^1 , F_{ij}^2 and F_{ijk}^3 are the source terms due to the forces acting on each bubble. It is worth noting that the force term only affects the moments of order higher than zero, because it is assumed that the number density of the bubbles is conserved. In general, the conservative equations for the bubble phase needed for coupling with the liquid phase are found by multiplying the expressions in Eq. 4.9 by m_b . For simplicity, hereinafter it will be assumed that all of the velocity moments have been multiplied by V_b (e.g., $M^0 = \varepsilon_b$).

The set of Eqs. 4.9 is not closed, because each equation contains the spatial fluxes of the moments of order immediately higher, and the source terms due to force. As a consequence, closures have to be provided for these terms. In this work, QBMM that use quadrature-based closures are applied. QBMM for dispersed-phase flows [33, 34, 35] are based on the idea of tracking a set of velocity moments of arbitrarily high order, providing closures to the source terms and the moment spatial fluxes in the moment transport equations by means of a quadrature approximation of the number density function. Passalacqua *et al.* [79] used this method to simulate dilute and moderately dilute fluid-particle flows. The key step of the approach is an inversion algorithm that allows one to uniquely determine a set of weights and abscissas from the set of transported moments. The condition for the inversion algorithm to be applied is that the set of moments is realizable, meaning it actually corresponds to a velocity distribution. This condition is not generally satisfied by traditional finite-volume methods used in computational fluid dynamics. Desjardins *et al.* [25] derived the realizability criterion (constraint on

timestep size) for the 1st-order finite-volume scheme. Vikas [115] derived realizability criteria for high-order finite-volume schemes and solved moment transport equations using QBMM on unstructured meshes. Recently, Yuan [126] have introduced the conditional quadrature method of moments (CQMOM), which guarantees a realizable representation of the distribution function under highly non-equilibrium conditions. Although for simplicity the present work does not use CQMOM, this will be done in our future work on gas-liquid flows.

In QBMM, quadrature formulas are used to provide closures to the source terms in the moment transport equations by introducing a set of β weights n_α and abscissas \mathbf{U}_α , which are determined from the moments of the distribution function using an inversion algorithm, and approximating the distribution function with a sum of Dirac delta functions:

$$f(\mathbf{v}) = \sum_{\alpha=1}^{\beta} n_\alpha \delta(\mathbf{v} - \mathbf{U}_\alpha). \quad (4.10)$$

In this work, a set of $\beta = 4$ weights and abscissas per velocity component will be considered, which are obtained by considering two quadrature nodes in each direction of 2-D velocity phase space. The inversion algorithm to obtain the weights and abscissas from the set of moments \mathbf{W} is explained in detail in Fox [33]. Once the weights and abscissas are known, the moments can be computed as a function of the quadrature weights and abscissas by approximating the integrals in Eq. 4.6 with summations:

$$\begin{aligned} M^0 &= \sum_{\alpha=1}^4 n_\alpha, & M_i^1 &= \sum_{\alpha=1}^4 n_\alpha U_{i\alpha}, \\ M_{ij}^2 &= \sum_{\alpha=1}^4 n_\alpha U_{i\alpha} U_{j\alpha}, & M_{ijk}^3 &= \sum_{\alpha=1}^4 n_\alpha U_{i\alpha} U_{j\alpha} U_{k\alpha}. \end{aligned} \quad (4.11)$$

The source terms in Eq. 4.9 due to forces are computed in terms of the abscissas as

$$\begin{aligned} F_i^1 &= \sum_{\alpha=1}^4 n_\alpha \left(\frac{F_{i\alpha}}{m_b} + g_i \right), \\ F_{ij}^2 &= \sum_{\alpha=1}^4 n_\alpha \left[\left(\frac{F_{i\alpha}}{m_b} + g_i \right) U_{j\alpha} + \left(\frac{F_{j\alpha}}{m_b} + g_j \right) U_{i\alpha} \right], \\ F_{ijk}^3 &= \sum_{\alpha=1}^4 n_\alpha \left[\left(\frac{F_{i\alpha}}{m_b} + g_i \right) U_{j\alpha} U_{k\alpha} + \left(\frac{F_{j\alpha}}{m_b} + g_j \right) U_{k\alpha} U_{i\alpha} + \left(\frac{F_{k\alpha}}{m_b} + g_k \right) U_{i\alpha} U_{j\alpha} \right]. \end{aligned} \quad (4.12)$$

As a consequence, the momentum exchange term \mathbf{M}_{lb} in Eq. 4.2 can be written in terms of the forces for each abscissa as

$$\mathbf{M}_{\text{lb}} = -\frac{1}{V_b} \sum_{\alpha=1}^4 n_{\alpha} F_{i\alpha}. \quad (4.13)$$

In Eqs. 4.12 and 4.13, the overall force term $F_{i\alpha}$ is defined by

$$F_{i\alpha} = F_{i\alpha}^{\text{P}} + F_{i\alpha}^{\text{D}} + F_{i\alpha}^{\text{VM}} + F_{i\alpha}^{\text{L}}, \quad (4.14)$$

where $F_{i\alpha}^{\text{P}}$, $F_{i\alpha}^{\text{D}}$, $F_{i\alpha}^{\text{VM}}$ and $F_{i\alpha}^{\text{L}}$ refer to the pressure, drag, virtual mass and lift forces, respectively.

The pressure force term is computed as

$$\mathbf{F}_{\alpha}^{\text{P}} = -V_b \nabla p, \quad (4.15)$$

and the drag force term is given by

$$\mathbf{F}_{\alpha}^{\text{D}} = \Upsilon_{\text{lb},\alpha} (\mathbf{U}_1 - \mathbf{U}_{\alpha}), \quad (4.16)$$

where $\Upsilon_{\text{lb},\alpha} = m_b/\tau_{\alpha}^{\text{D}}$ and the expression for drag time τ_{α}^{D} can be written as

$$\tau_{\alpha}^{\text{D}} = \frac{4d_b\rho_b}{3\varepsilon_1\rho_1 C_{\text{D}} |\mathbf{U}_1 - \mathbf{U}_{\alpha}|}. \quad (4.17)$$

In this work, the drag coefficient C_{D} is provided by the Schiller & Naumann [98] correlation:

$$C_{\text{D}} = \begin{cases} \frac{24}{\text{Re}_{b\alpha}} [1 + 0.15(\text{Re}_{b\alpha})^{0.687}], & \text{if } \text{Re}_{b\alpha} \leq 1000 \\ 0.44, & \text{otherwise.} \end{cases} \quad (4.18)$$

However, more sophisticated bubble drag correlations can easily be used in place of Eq. 4.18 [108].

The bubble Reynolds number for each abscissa is defined by

$$\text{Re}_{b\alpha} = \frac{\rho_1 d_b |\mathbf{U}_1 - \mathbf{U}_{\alpha}|}{\mu_1}. \quad (4.19)$$

It is worth underlining that in the evaluation of the force term, the relative velocity vector $\mathbf{U}_1 - \mathbf{U}_{\alpha}$ is defined as a function of the quadrature abscissas \mathbf{U}_{α} , instead of the mean bubble velocity. As a consequence, the drag force has different values for each quadrature node.

The lift force term [3] is given by

$$\mathbf{F}_{\alpha}^{\text{L}} = C_{\text{L}}\rho_1 V_b (\mathbf{U}_1 - \mathbf{U}_{\alpha}) \times (\nabla \times \mathbf{U}_1), \quad (4.20)$$

while the virtual mass force term [3] is given by

$$\mathbf{F}_\alpha^{\text{VM}} = -C'_{\text{VM}}\rho_1V_b \left(\frac{d\mathbf{U}_\alpha}{dt} - \frac{D_1\mathbf{U}_1}{Dt} \right) \quad (4.21)$$

where

$$C'_{\text{VM}} = C_{\text{VM}} [1 + 2.78 (1 - \varepsilon_1)]. \quad (4.22)$$

In Eq. 4.22, $\frac{d}{dt}$ and $\frac{D_1}{Dt}$ refer to total time derivatives for bubble and liquid phases, respectively. In the present work, $C_{\text{VM}} = 0.5$ and $C_{\text{L}} = 0.53$ are used. The reader should note that it is straightforward to add other forces acting on an individual bubbles through the liquid phase (e.g. the wall force introduced by Tomiyama *et al.* [107]). In fact, one advantage of formulating the model in terms of a mesoscopic kinetic equation is that the connection to the microscopic force balances is retained, thereby allowing for a high-fidelity physical model for the dispersed phase.

An important point for obtaining a stable solution to the moment transport equations is represented by the closure provided for the moment spatial fluxes appearing in Eq. 4.9. These fluxes are represented by the second term on the left-hand side of Eq. 4.9, and are computed according to their kinetic definition [82, 25, 33]. First each moment involved in the expression for the fluxes is decomposed into two contributions. For example, the zero-order moment has a spatial flux involving the first-order moments:

$$M_i^1 = M_i^- + M_i^+ = \int_{-\infty}^0 v_i \left(\int f dv_j dv_k \right) dv_i + \int_0^{+\infty} v_i \left(\int f dv_j dv_k \right) dv_i. \quad (4.23)$$

Using QBMM, the integrals in Eq. 4.23 are approximated by a Dirac-delta representation as discussed in detail in Sec. 4.3. This procedure to evaluate the spatial fluxes is essential to ensure the realizability of the set of moments by means of the quadrature approximation, or, in other words, that the set of weights and abscissas actually represent a real distribution function. At this point, all of the terms in the moment transport equations have been closed using QBMM. We will now describe our numerical implementation of the fully coupled flow solver.

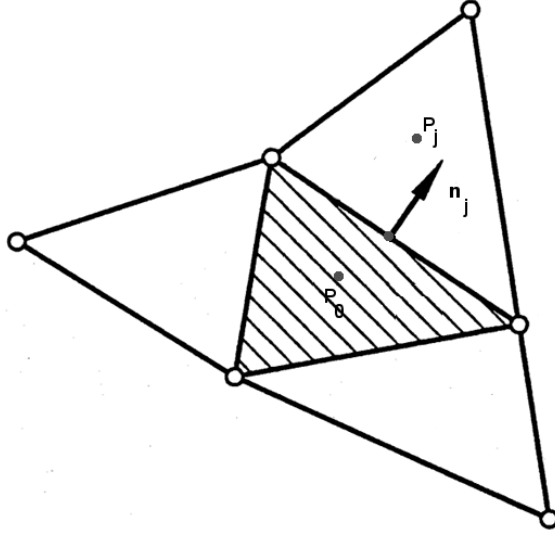


Figure 4.1 Control volume and its neighbors for an unstructured mesh.

4.3 Description of Flow Solver

This section is devoted to a detailed presentation of the numerical methods used to solve the bubbly flow model. An unstructured finite-volume approach is used to solve the governing equations for both the liquid and bubble phases. The same collocated grid arrangement is used for both phases. A sample unstructured control volume (cell) and its neighbors are shown in Fig. 4.1. P_0 denotes both the central cell and its cell center, P_j denotes both the neighbor cell and the cell center of the neighbor cell and j represents both the face and the face center. The outward unit-normal vector is denoted by \mathbf{n}_j . Let Ω_{P_0} be the volume of the cell P_0 and S_j be the area of the face j . In the remainder of this section, we first describe the liquid-phase flow solver in Sec. 4.3.1, followed by the bubble-phase flow solver in Sec. 4.3.2. Finally, details on the coupling between the two solvers are provided in Sec. 4.3.3.

4.3.1 Liquid-phase solution strategy

In this section details of the liquid-phase solver are presented. The liquid-phase equations are solved using the SIMPLE algorithm [81, 24, 68].

4.3.1.1 Liquid-phase velocity equations

The momentum equations (Eq. 4.2) are discretized to form a linear system for the liquid-phase velocities. The discretized velocity equations can be written as

$$A_0^\phi \phi_{P_0} + \sum_j A_j^\phi \phi_{P_j} = b^\phi \quad (4.24)$$

where $\phi = \{U_l, V_l\}$ in 2-D and summation is over all the faces of cell P_0 . The coefficients in Eq. 4.24 can be written as

$$\begin{aligned} A_j^\phi &= \min(\dot{m}_j, 0) + \frac{\mu_l \varepsilon_{1,j} S_j \delta_{sj}}{|\mathbf{r}_{P_j} - \mathbf{r}_{P_0}|} \\ A_0^\phi &= \left[1 + \frac{\gamma_t}{2}\right] \frac{\rho_l \varepsilon_{1,P_0} \Omega_{P_0}}{\Delta t} + \sum_j \left[\max(\dot{m}_j, 0) + \frac{\mu_l \varepsilon_{1,j} S_j \delta_{sj}}{|\mathbf{r}_{P_j} - \mathbf{r}_{P_0}|} \right] \\ &\quad - \frac{\Omega_{P_0}}{V_b} \sum_{\alpha=1}^4 n_{\alpha,P_0} \Upsilon_{lb,\alpha,P_0} + \frac{1}{\Delta t} \left[1 + \frac{\gamma_t}{2}\right] \sum_{\alpha=1}^4 n_{\alpha,P_0} \rho_l \Omega_{P_0} C'_{VM,P_0} \\ b^\phi &= \frac{1}{\Delta t} [1 + \gamma_t] \rho_l \Omega_{P_0} \varepsilon_{P_0}^n \phi_{P_0}^n - \frac{\gamma_t}{2\Delta t} \rho_l \Omega_{P_0} \varepsilon_{P_0}^{n-1} \phi_{P_0}^{n-1} \\ &\quad + \gamma_s \left[\max(\dot{m}_j, 0) \nabla \phi_{P_0} \cdot (\mathbf{r}_j - \mathbf{r}_{P_0}) + \sum_j \min(\dot{m}_j, 0) \nabla \phi_{P_j} \cdot (\mathbf{r}_j - \mathbf{r}_{P_j}) \right] \\ &\quad + q^\phi. \end{aligned} \quad (4.25)$$

In Eq. 4.25, \dot{m}_j is the outgoing mass flux at face j , the superscripts n and $n - 1$ denote the previous two time levels and the term δ_{sj} is defined such that

$$\mathbf{n}_j = \delta_{sj} \mathbf{s}_j + \delta_{tj} \mathbf{t}_j, \quad (4.26)$$

where $\mathbf{s}_j = \frac{\mathbf{r}_{P_j} - \mathbf{r}_{P_0}}{|\mathbf{r}_{P_j} - \mathbf{r}_{P_0}|}$, is the unit vector from P_0 to P_j and \mathbf{t}_j is the unit vector tangential to the face. The two parameters γ_t and γ_s control the temporal and spatial schemes, respectively. If $\gamma_t = 0$ then 1st-order Euler implicit time-integration is used, while if $\gamma_t = 1$ then 2nd-order two-level backward implicit time-integration is used. Similarly, if $\gamma_s = 0$, 1st-order spatial reconstruction is used and if $\gamma_s = 1$, 2nd-order spatial reconstruction is used.

The liquid-phase volume fraction at the face j is computed as

$$\varepsilon_{1,j} = \frac{1}{2} [\varepsilon_{1,P_0} + \varepsilon_{1,P_j}] + \frac{\gamma_s}{2} [\nabla \varepsilon_{1,P_0} \cdot (\mathbf{r}_j - \mathbf{r}_{P_0}) + \nabla \varepsilon_{1,P_j} \cdot (\mathbf{r}_j - \mathbf{r}_{P_j})]. \quad (4.27)$$

All other variables at the faces are computed in the same way. The gradients are computed using least-squares reconstruction [4, 118] combined with Venkatkrishnan limiter [114].

It is worth noting that in Eq. 4.25, some of the momentum exchange terms are treated implicitly. A_0^ϕ contains contributions from the drag and virtual mass terms. This adds to the robustness of the solver. On the right-hand side of the third equation in Eq. 4.25, q^ϕ refers to all the remaining sources coming from pressure, diffusion and the momentum exchange terms that are not treated implicitly. Also, note that $A_0^{U_1} = A_0^{V_1}$.

4.3.1.2 Rhie-Chow interpolation

Its very well known that a collocated grid arrangement may lead to a pressure-velocity decoupling problem. In order to get rid of this problem, Rhie-Chow interpolation [91] is employed to compute the mass flux at cell faces:

$$\dot{m}_j = \varepsilon_{1,j} \rho_1 \mathbf{U}_{1,j}^* \cdot \mathbf{n}_j S_j. \quad (4.28)$$

In the above equation, $\mathbf{U}_{1,j}^* = \mathbf{U}_{1,j} + \delta \mathbf{U}_{1,j}^{\text{RC}}$, where

$$\mathbf{U}_{1,j} = \frac{1}{2} [\mathbf{U}_{1,P_0} + \mathbf{U}_{1,P_j}] + \frac{\gamma_s}{2} [\nabla \mathbf{U}_{1,P_0} \cdot (\mathbf{r}_j - \mathbf{r}_{P_0}) + \nabla \mathbf{U}_{1,P_j} \cdot (\mathbf{r}_j - \mathbf{r}_{P_j})], \quad (4.29)$$

and

$$\delta \mathbf{U}_{1,j}^{\text{RC}} = \left(\frac{\Omega_{P_0} \varepsilon_{1,P_0}}{A_0^{U_1}} \right)_j \left[\overline{\nabla p_j} \cdot \frac{(\mathbf{r}_{P_j} - \mathbf{r}_{P_0})}{|\mathbf{r}_{P_j} - \mathbf{r}_{P_0}|} - \frac{(p_{P_j} - p_{P_0})}{|\mathbf{r}_{P_j} - \mathbf{r}_{P_0}|} \right] \mathbf{n}_j. \quad (4.30)$$

In Eq. 4.30, the overbar denotes an averaged value at the face and $A_0^{U_1} = A_0^{U_1} = A_0^{V_1}$.

4.3.1.3 Pressure-correction equation

The velocities obtained after solving Eq. 4.24 do not satisfy the continuity equation. In order to satisfy the continuity equation, the pressure needs to be adjusted. Instead of solving for pressure, an equation for the pressure-correction (\dot{p}) is solved:

$$A_0^{\dot{p}} \dot{p}_{P_0} + \sum_j A_j^{\dot{p}} \dot{p}_{P_j} = b^{\dot{p}}, \quad (4.31)$$

where

$$\begin{aligned}
A_j^{\dot{p}} &= -\frac{\rho_l \varepsilon_{1,j} S_j}{|\mathbf{r}_{P_0} - \mathbf{r}_{P_j}|} \overline{\left(\frac{\Omega_{P_0} \varepsilon_{1,P_0}}{A_0^{\mathbf{U}_1}} \right)}_j, \\
A_0^{\dot{p}} &= -\sum_j A_{P_j}^{\dot{p}}, \\
b^{\dot{p}} &= -\frac{\rho_l \Omega_{P_0}}{\Delta t} \left[\left(1 + \frac{\gamma t}{2}\right) \varepsilon_{1,P_0} - (1 + \gamma t) \varepsilon_{1,P_0}^n + \frac{\gamma t}{2} \varepsilon_{1,P_0}^{n-1} \right] - \sum_j \dot{m}_j.
\end{aligned} \tag{4.32}$$

In Eq. 4.32, ε_{1,P_0} is the latest liquid-phase volume fraction in cell P_0 , while ε_{1,P_0}^n and $\varepsilon_{1,P_0}^{n-1}$ are the volume fractions from the two previous time levels.

4.3.1.4 Boundary conditions for liquid phase

In the present work, two kinds of boundaries are used: no-slip wall and pressure boundary. At a no-slip wall, both tangential and normal components of the velocity are zero. The mass flux at a no-slip wall is zero. This boundary condition is easy to implement. Imposing the boundary condition at a pressure boundary is a little bit more involved. At a pressure boundary, the flow can be into the domain or out of the domain. If the flow is out of the domain, the static pressure is specified and the velocity is interpolated from the interior cell. If the flow is into the domain, the total pressure is specified and the velocity is computed using Bernoulli's equation by using the interior cell static pressure. Implementation details for both types of boundary conditions can be found in Mathur & Murthy [69].

4.3.1.5 Solution algorithm for liquid phase

At each time level the following algorithm is followed to solve the liquid-phase equations:

1. Setup and solve the velocity equations (Eq. 4.25) using the pressure from the previous time level or the previous iteration. The liquid-phase volume fraction is computed as $\varepsilon_l = 1 - \varepsilon_b$, where ε_b is obtained from the bubble-phase solver.
2. Recompute the mass flux at cell faces using Rhie-Chow interpolation.
3. Setup and solve the pressure-correction equation.

4. Correct pressure and velocities in the cells and mass fluxes at cell faces using the pressure correction.
5. Check for convergence. If converged go to the next time level, else repeat steps 1 through 5.

To compute the momentum exchange terms in the liquid-phase equations, the latest available bubble-phase properties are used. For solving the velocity and pressure-correction equations, bi-conjugate-gradient and conjugate-gradient methods are used, respectively. In step 1, the velocity equations are under-relaxed before solving. Details about the under-relaxation in step 1 and the computations in step 4 can be found in Demirdzic & Muzaferija [24]. The convergence criterion in step 5 is based either on a prescribed maximum number of iterations or on the momentum and continuity residuals converging to a prescribed value, whichever is achieved first.

4.3.2 Bubble-phase solution strategy

The moment transport equations (Eqs. 4.9) are discretized using a finite-volume approach using the same mesh as the liquid-phase equations. Before proceeding with the description of the QBMM solver, it is worth reiterating that the moment transport equations are rescaled so that the zero-order moment M^0 represents the bubble-phase volume fraction instead of the number density. This operation is important to ensure the stability and accuracy of the quadrature-inversion algorithm, which could be compromised by the high round-off error caused by the computation in terms of the number density. As noted earlier, the scaling of the equations is simply performed by multiplying them by the bubble volume V_b , and by modifying the bubble-bubble interaction and drag terms accordingly. After this rescaling, the drag time τ_α^D is unchanged. The rescaled weights n_α can then be interpreted as representing the volume fractions of the corresponding abscissas.

The moment transport equations contain convection and force terms. These terms are treated in a sequential manner using an operator-splitting approach. For clarity, treatment of these terms is discussed below using a 1st-order, single-stage Euler explicit time-integration

scheme. Details about 2nd-order, two-stage RK2SSP time integration can be found in Vikas [115]. In the following description, the convection terms are treated first, followed by the force terms. This order, however, can be changed without loss of accuracy.

4.3.2.1 Contribution of moment convection terms

The contribution of the convection terms in the moment transport equations is accounted for using a finite-volume approach. Let $\mathbf{U}_\alpha = [U_\alpha \ V_\alpha]$, $\mathbf{N}_\alpha = [n_\alpha \ \mathbf{U}_\alpha]$ and $\mathbf{N} = [\mathbf{N}_\alpha : \alpha = \{1, 2, 3, 4\}]$. The evolution equation for the set of moments (\mathbf{W}) using a single-stage Euler explicit time-integration scheme can be written as

$$\mathbf{W}_{P_0}^* = \mathbf{W}_{P_0}^n - \frac{\Delta t}{\Omega_{P_0}} \sum_j \{ \mathbf{G}(\mathbf{N}_{j,L}^n, \mathbf{N}_{j,R}^n, \mathbf{n}_j) S_j \}, \quad (4.33)$$

where $\mathbf{N}_{j,L}^n = [\mathbf{N}_{\alpha,j,L}^n : \alpha = \{1, 2, 3, 4\}]$ and $\mathbf{N}_{j,R}^n = [\mathbf{N}_{\alpha,j,R}^n : \alpha = \{1, 2, 3, 4\}]$, respectively, represent the reconstructed weights and abscissas (\mathbf{N}^n) on the left (L) and right (R) sides of face j . The outward normal vector $\mathbf{n}_j = [n_{j1} \ n_{j2}]$ points from the left side to the right side of face j . For reconstruction at the left and right sides of the faces, a 1st-order or *quasi*-2nd-order scheme can be used. For the 1st-order scheme, 1st-order reconstruction is used for both the weights and abscissas. For the *quasi*-2nd-order scheme, 2nd-order least-squares reconstruction with a Venkatkrishnan limiter is used for the weights and 1st-order reconstruction is used for the abscissas. For both the 1st and *quasi*-2nd-order schemes, the time step size must satisfy the realizability constraint. More details about the reconstructions and realizability criteria can be found in Vikas [115]. The numerical flux (\mathbf{G}) is computed as

$$\mathbf{G}(\mathbf{N}_{j,L}^n, \mathbf{N}_{j,R}^n, \mathbf{n}_j) = \sum_{\alpha=1}^4 [\max(\mathbf{n}_j \cdot \mathbf{U}_{\alpha,j,L}, 0) \mathbf{W}_{\alpha,j,L}^n + \min(\mathbf{n}_j \cdot \mathbf{U}_{\alpha,j,R}, 0) \mathbf{W}_{\alpha,j,R}^n], \quad (4.34)$$

where $\mathbf{W}_{\alpha,j,L}^n$ and $\mathbf{W}_{\alpha,j,R}^n$ are computed using $\mathbf{N}_{\alpha,j,L}^n$ and $\mathbf{N}_{\alpha,j,R}^n$, respectively.

4.3.2.2 Contribution of force terms

The contribution of the force terms is computed by acting on the weights and abscissas directly. The following two ordinary differential equations are solved:

$$\begin{aligned} \frac{dn_\alpha}{dt} &= 0, \\ \frac{d\mathbf{U}_\alpha}{dt} &= \frac{\mathbf{F}_\alpha^P + \mathbf{F}_\alpha^D + \mathbf{F}_\alpha^L + \mathbf{F}_\alpha^{\text{VM}}}{m_b} + \mathbf{g}. \end{aligned} \quad (4.35)$$

These equations are written considering that the forces do not affect the quadrature weights because they do not change the number of the bubbles, but only influence the abscissas. The last equation is modified to treat the $\frac{d\mathbf{U}_\alpha}{dt}$ term in $\mathbf{F}_\alpha^{\text{VM}}$ implicitly:

$$\frac{d\mathbf{U}_\alpha}{dt} = \frac{\mathbf{F}_\alpha^P + \mathbf{F}_\alpha^D + \mathbf{F}_\alpha^L + \tilde{\mathbf{F}}_\alpha^{\text{VM}} + m_b \mathbf{g}}{\tilde{m}_b} \quad (4.36)$$

where $\tilde{m}_b = m_b + \rho_l V_b C'_{\text{VM}}$ and $\tilde{\mathbf{F}}_\alpha^{\text{VM}} = \rho_l V_b C'_{\text{VM}} \frac{D_l \mathbf{U}_l}{Dt}$. This adds to the stability of the solver.

Using single-stage, Euler-explicit time integration the weights and abscissas in cell P_0 can be updated as

$$\begin{aligned} n_{\alpha, P_0}^{n+1} &= n_{\alpha, P_0}^* \\ \mathbf{U}_{\alpha, P_0}^{n+1} &= \mathbf{U}_{\alpha, P_0}^* + \Delta t \left(\frac{\mathbf{F}_{\alpha, P_0}^{P,*} + \mathbf{F}_{\alpha, P_0}^{D,*} + \mathbf{F}_{\alpha, P_0}^{L,*} + \tilde{\mathbf{F}}_{\alpha, P_0}^{\text{VM},*} + m_b \mathbf{g}}{\tilde{m}_{b, P_0}^*} \right), \end{aligned} \quad (4.37)$$

where n_{α, P_0}^* and $\mathbf{U}_{\alpha, P_0}^*$ are computed from the moments in $\mathbf{W}_{P_0}^*$. As is done for the interaction terms below, another alternative to handle the stiffness of the force terms is to linearize the ordinary differential equation (ODE) in Eq. 4.36 and then directly use the analytical solution of this linearized ODE. Although not used here, this alternative would allow for a larger time step than is possible with Eq. 4.37. The moments at time step $n + 1$ ($\mathbf{W}_{P_0}^{n+1}$) are computed using n_{α, P_0}^{n+1} and $\mathbf{U}_{\alpha, P_0}^{n+1}$.

4.3.2.3 Boundary conditions for bubble phase

During the convection step mentioned in Sec. 4.3.2.1, boundary conditions are needed. These boundary conditions can be specified either in terms of the moments or in terms of the weights and abscissas. The latter approach is more convenient and is followed in the present work. In this work, three types of boundary conditions are used: Dirichlet, outflow, and

specular wall. At a Dirichlet boundary, the weights and abscissas are specified. At an outflow boundary, the weights and abscissas are extrapolated from the interior, i.e. given the left-side weights and abscissas ($\mathbf{N}_{j,L}$) on boundary face j , the right-side weights and abscissas ($\mathbf{N}_{j,R}$) are computed using $\mathbf{N}_{j,R} = \mathbf{N}_{j,L}$. At a specular-wall boundary, the right-side weights and abscissas are computed using

$$n_{\alpha,j,R} = n_{\alpha,j,L}/e_{bw}, \quad (4.38)$$

$$\mathbf{U}_{\alpha,j,R} = \mathbf{U}_{\alpha,j,L} - (1 + e_{bw}) (\mathbf{n}_j \cdot \mathbf{U}_{\alpha,j,L}) \mathbf{n}_j,$$

where e_{bw} is the bubble-wall restitution coefficient. For the simulations in the present work, $e_{bw} = 1$. It should be noted that the unit-normal vector, \mathbf{n}_j , points out of the domain at boundary faces.

4.3.2.4 Solution algorithm for bubble phase

A detailed solution algorithm for the moment equations can be found in Fox [34] and Vikas [115]. Here a brief overview of the steps involved in the solution procedure at each time step is presented, assuming a single-stage, Euler explicit time-integration scheme:

1. Apply boundary conditions to weights and abscissas.
2. Compute moments using weights and abscissas.
3. Reconstruct weights and abscissas at cell faces.
4. Compute spatial flux terms at cell faces.
5. Advance moments by Δt due to spatial flux terms using a finite-volume approach.
6. Compute weights and abscissas from moments using the moment-inversion algorithm.
7. Advance weights by Δt due to force terms.
8. Compute moments using weights and abscissas.

To compute the force terms in step 7, the latest available liquid-phase properties are used.

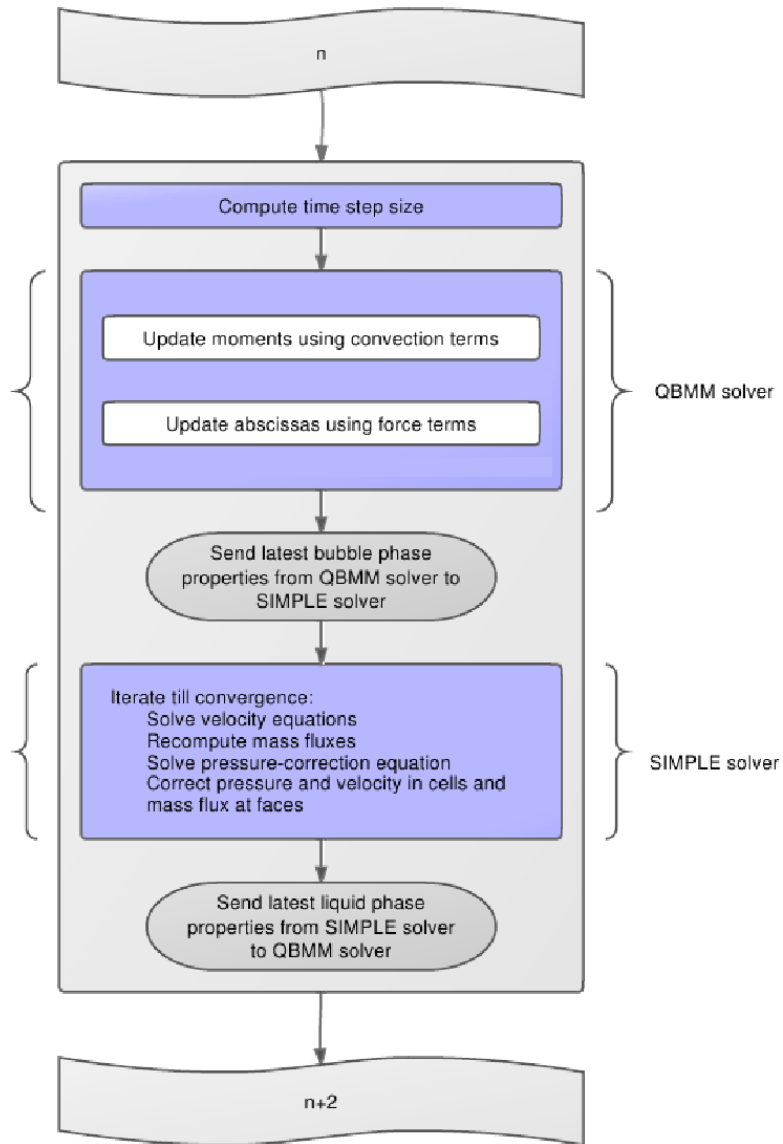


Figure 4.2 Schematic of the control flow for the coupled bubbly flow solver.

4.3.3 Coupling algorithm

A schematic of the control flow for the coupled bubbly flow solver is shown in Fig. 4.2. Both solvers use the same time step size Δt , which is calculated as $\Delta t = \min(\Delta t_1^{\text{CFL}}, \Delta t_b^{\text{CFL}}, \tilde{\tau}_\alpha^{\text{D}})$, where Δt_1^{CFL} and Δt_b^{CFL} are the time step sizes computed on the basis of the convection terms in liquid and bubble phases, respectively, using a specified CFL number and the modified drag time, $\tilde{\tau}_\alpha^{\text{D}}$, is defined as

$$\tilde{\tau}_\alpha^{\text{D}} = \frac{\tilde{m}_b}{m_b} \tau_\alpha^{\text{D}}, \quad (4.39)$$

to include the affect of added mass. In the present work, $\text{CFL} = 1$ is used to compute Δt_1^{CFL} and Δt_b^{CFL} .

At each time step, first the bubble-phase equations are solved using the QBMM solver and then the liquid-phase equations are solved using the SIMPLE solver. There exists a two-way coupling since the bubble-phase solver needs the liquid-phase properties to compute the force terms. As mentioned earlier and also shown in the schematic in Fig. 4.2, the latest available liquid-phase properties are used by the bubble-phase solver. Once the bubble-phase equations are solved and the bubble-phase volume fraction is known, the liquid-phase volume fraction is calculated. The liquid-phase solver also needs the bubble-phase properties. Here again, the latest available bubble-phase properties are used.

4.4 Numerical Results

4.4.1 Description of 2-D test case

The 2-D domain used for simulations is shown in Fig. 4.3. The width (D) and height (H) of the domain are 0.5 m and 1.5 m, respectively. The opening at the lower boundary is 0.04 m wide and its center is located at a distance of 0.15 m from the lower-left corner of the domain. A Cartesian mesh with 50 grid points along the horizontal direction and 100 grid points along the vertical direction is used. The properties of gas (bubble) and liquid phases used in simulations are given in Table 4.1. Results are presented for two different gas flow rates: 1.6 l/min (lower gas flow rate) and 8.0 l/min (higher gas flow rate).

The boundary conditions (BC) are given in Table 4.2. For the liquid-phase solver, the

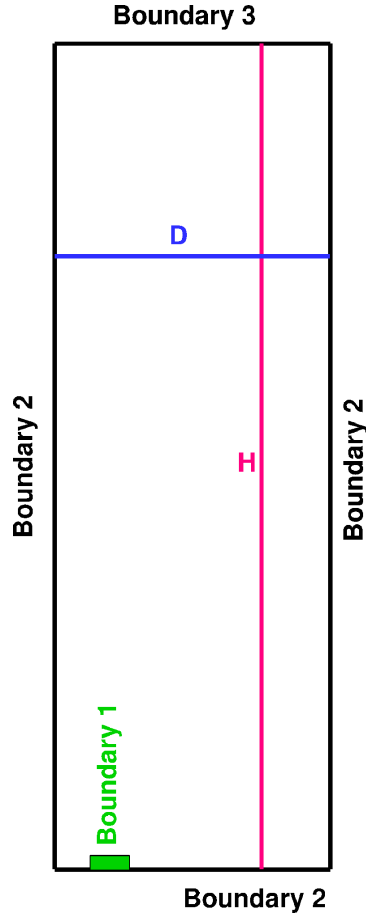


Figure 4.3 Schematic of the 2-D domain used for simulations.

Table 4.1 Gas (bubble) and liquid properties.

Property	Value
Bubble diameter (d_b)	2 mm
Gas density (ρ_b)	1.2 kg m^{-3}
Liquid density (ρ_l)	1000 kg m^{-3}
Liquid dynamic viscosity (μ_l)	$0.001 \text{ kg m}^{-1} \text{ s}^{-1}$
Gas flow rate	$1.6 \text{ l min}^{-1} / 8.0 \text{ l min}^{-1}$

Table 4.2 Boundary conditions.

Boundary	BC for bubble phase	BC for liquid phase
1	Dirichlet	Pressure BC
2	Specular wall	No-slip wall
3	Outflow	Pressure BC

same pressure is specified at the two pressure boundaries. A more accurate approach would be to capture the interface between the liquid and the bubble phases near the top boundary. In that case, liquid-phase boundary condition would not be needed at the top boundary. However, such an approach is left to future work as the main aim of the present work is to demonstrate the implementation of the new model. Initially the domain only contains the liquid phase. The bubble phase is injected through the opening at the bottom surface.

In the present work, a 2nd-order two-stage RK2SSP time-integration is used for the bubble-phase QBMM solver, while a 2nd-order two-level backward implicit time-integration is used for the liquid-phase SIMPLE solver. For the spatial reconstruction, a 2nd-order scheme is used for the liquid-phase equations, while a quasi-2nd-order scheme is used for the bubble-phase equations.

As a verification test case for our model, the terminal rise velocity of a single bubble as calculated from a force balance is compared to the bubble velocity predicted by the flow solver. For a bubble rising with a steady velocity through a quiescent liquid the buoyancy force just equals the sum of the gravity and drag forces. The bubble's terminal rise velocity is given by

$$|\mathbf{U}_{b,\text{rise}}| = \sqrt{\frac{8(\rho_l - \rho_b) d_b g}{6C_D \rho_l}}, \quad (4.40)$$

where $g = 9.81 \text{ m s}^{-2}$ is the gravitational acceleration and C_D is calculated from Eq. 4.18. This gives a terminal rise velocity of 0.208 m s^{-1} for the properties given in Table 4.1. Our 2-D flow solver was also used to determine the terminal velocity. Only one-way coupling from the liquid to the bubble phase was considered. Our flow code predicted the same terminal rise velocity as mentioned above, thereby verifying that the force terms are correctly implemented in the bubble-phase solver. Next, results for the two gas flow rates are discussed.

4.4.2 Lower gas flow rate

For the case with gas flow rate equal to 1.6 l/min, the weights and abscissas at the Dirichlet boundary are specified as

$$\begin{aligned} n_1 = 0.25, \quad n_2 = 0.25, \quad n_3 = 0.25, \quad n_4 = 0.25, \\ U_1 = 0.0000001, \quad U_2 = -0.0000001, \quad U_3 = 0.0000001, \quad U_4 = -0.0000001, \\ V_1 = 0.0006667, \quad V_2 = 0.0006667, \quad V_3 = 0.0006665, \quad V_4 = 0.0006665. \end{aligned} \quad (4.41)$$

A small fluctuation in the abscissas in Eq. 4.41 is necessary for the inversion algorithm to work properly. Figure 4.4 shows the instantaneous contour plots of the bubble-phase volume fraction (ε_b) obtained using QBMM and Eulerian-Lagrangian simulation by Delnoij *et al.* [22] at $t = 60$ s. The QBMM results agree qualitatively with the Eulerian-Lagrangian results. Figure 4.5 shows the instantaneous plots for liquid-phase velocity magnitude and velocity vectors respectively at the same time as above. Note that the velocity vectors are not drawn to scale. The instantaneous contour plots of the bubble-phase granular temperature (Θ_b), along with the bubble-phase Mach number (Ma_b), and the Stokes number (St_b) at $t = 60$ s are shown in Fig. 4.6. The granular temperature (Θ_b) is defined in terms of the moments by

$$\Theta_b = \frac{1}{2} (\sigma_{11} + \sigma_{22}), \quad (4.42)$$

where

$$\sigma_{11} = \frac{M_{11}^2}{M^0} - \left(\frac{M_1^1}{M^0} \right)^2 \quad \text{and} \quad \sigma_{22} = \frac{M_{22}^2}{M^0} - \left(\frac{M_2^1}{M^0} \right)^2. \quad (4.43)$$

The Mach number is defined as

$$\text{Ma}_b = \frac{|\mathbf{U}_b|}{\sqrt{\Theta_b}}, \quad \text{Kn}_b = \sqrt{\frac{\pi}{2}} \frac{\tau_c |\mathbf{U}_b|}{D}, \quad (4.44)$$

while the Stokes number is defined as

$$\text{St}_b = \frac{\tilde{\tau}^D}{\tau^F}, \quad (4.45)$$

where $\tilde{\tau}^D$ is the modified drag time based on mean bubble velocity and $\tau^F = \frac{|\mathbf{U}_1|}{D}$ is the flow time. Physically, $\text{Ma}_b > 1$ implies that bubble transport is dominated by mean convection, as opposed to random bubble-velocity fluctuations, while the small St_b implies that the bubble-phase mean velocity will be very close to the liquid-phase velocity since the drag force is

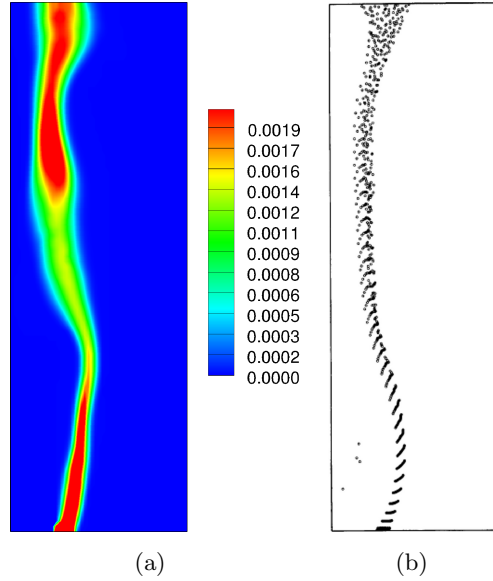


Figure 4.4 Instantaneous contour plots of bubble-phase volume fraction (ε_b) for gas flow rate equal to 1.6 l/min at $t = 60$ s (a) using QBMM, (b) using Eulerian-Lagrangian approach.

inversely proportional to St_b . The instantaneous contours show that the bubble-phase granular temperature is very small throughout the domain, while the bubble-phase Mach number is large, both of which are a result of the dominance of the drag term (very small St_b) in the bubble-phase model. Figure 4.7 shows the instantaneous contour plots of the bubble-phase volume fraction (ε_b) at four different times. The meandering behavior of the bubble plume due to the dynamic interaction between the two phases can be clearly seen. As the bubble phase is injected into the quiescent liquid column, the liquid phase near the opening is dragged along, creating small vortices. These vortices in turn deflect the bubbles from their path due to the lift and drag forces. As time progresses, the vortices grow larger, leading to a meandering bubble plume.

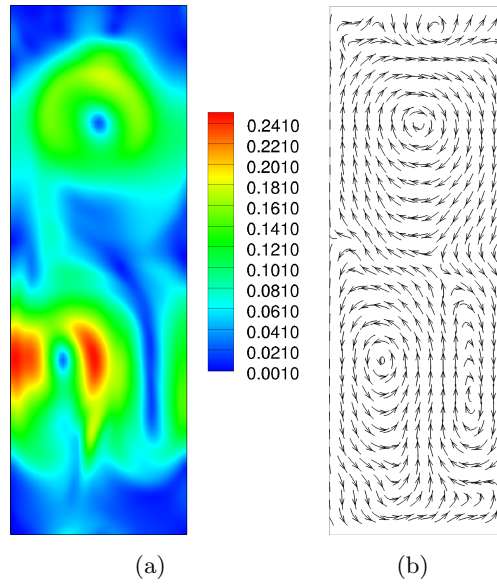


Figure 4.5 Instantaneous contour plots for gas flow rate equal to 1.6 l/min at $t = 60$ s for liquid-phase (a) velocity magnitude ($|\mathbf{U}_1|$, m s^{-1}), (b) velocity vectors.

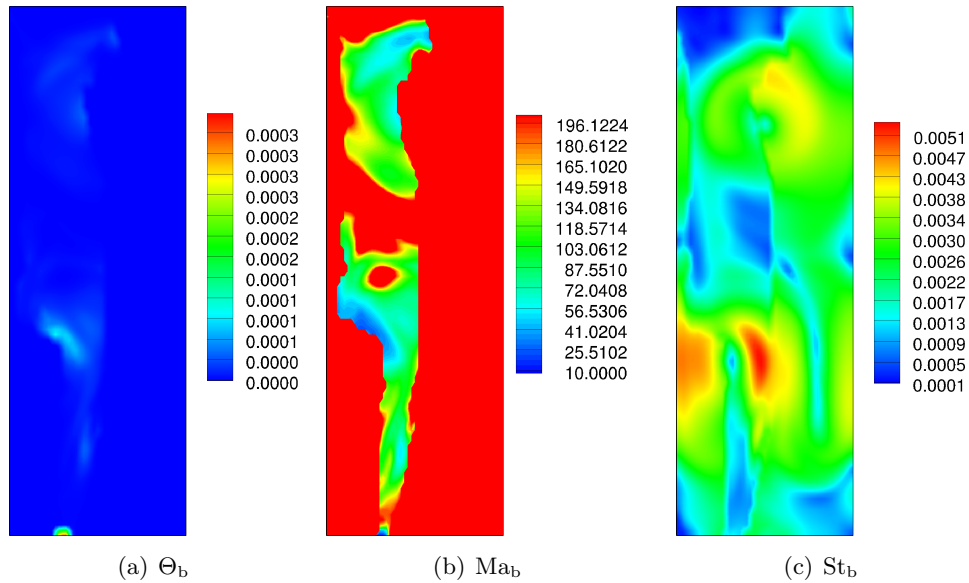


Figure 4.6 Instantaneous contour plots of bubble-phase (a) granular temperature (m s^{-1}), (b) Mach number, (c) Stokes number for gas flow rate equal to 1.6 l/min at $t = 60$ s.

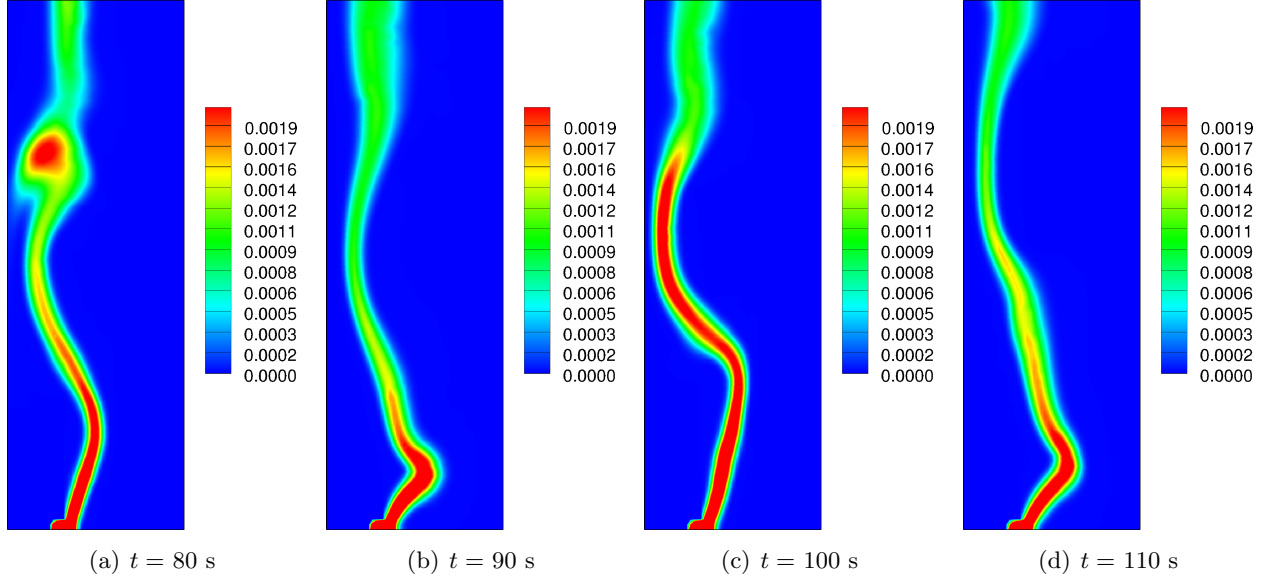


Figure 4.7 Instantaneous contour plots of bubble-phase volume fraction (ε_b) for gas flow rate equal to 1.6 l/min.

4.4.3 Higher gas flow rate

For the case with gas flow rate equal to 8.0 l/min, the weights and abscissas at the Dirichlet boundary are specified as

$$\begin{aligned}
 n_1 &= 0.25, \quad n_2 = 0.25, \quad n_3 = 0.25, \quad n_4 = 0.25, \\
 U_1 &= 0.0000001, \quad U_2 = -0.0000001, \quad U_3 = 0.0000001, \quad U_4 = -0.0000001, \\
 V_1 &= 0.0033334, \quad V_2 = 0.0033334, \quad V_3 = 0.0033332, \quad V_4 = 0.0033332.
 \end{aligned} \tag{4.46}$$

Figure 4.8 shows the instantaneous contour plots of the bubble-phase volume fraction (ε_b) obtained using QBMM and Eulerian-Lagrangian simulation by Delnoij *et al.* [22] at $t = 60$ s. Again, the QBMM results agree qualitatively with the Eulerian-Lagrangian results. Figure 4.9 shows the instantaneous plots for liquid-phase velocity magnitude and velocity vectors respectively at the same time as above. The velocity vectors are not drawn to scale. The instantaneous contour plots of the bubble-phase granular temperature (Θ_b), along with the bubble-phase Mach number (Ma_b), and the Stokes number (St_b) at $t = 60$ s are shown in Fig. 4.10. As seen for the lower gas flow rate, the bubble-phase velocity in the higher gas flow rate is dominated by the drag force, leading to a very small Stokes number. In contrast, due

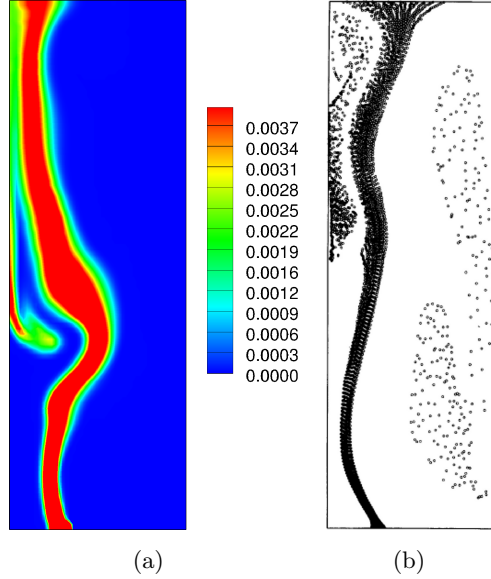


Figure 4.8 Instantaneous contour plots of bubble-phase volume fraction (ε_b) for gas flow rate equal to 8.0 l/min at $t = 60$ s (a) using QBMM, (b) using Eulerian-Lagrangian approach.

to the small ratio between ρ_b and ρ_l , the liquid-phase velocity is mainly determined by the bubble-phase volume fraction through the liquid-phase continuity equation. In other words, the change of ε_b due to moment convection in the bubble-phase solver drives the liquid-phase acceleration through the pressure-correction term in the liquid-phase solver. Figure 4.11 shows the instantaneous contour plots of the bubble-phase volume fraction (ε_b) at four different times. The meandering behavior of the bubble plume is much more significant for the higher gas flow rate. As demonstrated by the results presented in this section, our fully coupled flow solver successfully captures this strong coupling between the two phases.

4.5 Conclusions

We have presented a novel approach to model bubble-column flows using quadrature-based moment methods (QBMM). A fully two-way coupled flow solver has been developed that solves the incompressible Navier-Stokes equation for the liquid phase and moment transport equations for the dispersed bubble phase. The moment transport equations for the dispersed bubble phase are solved using a kinetic theory approach. Contributions from the liquid-phase pressure

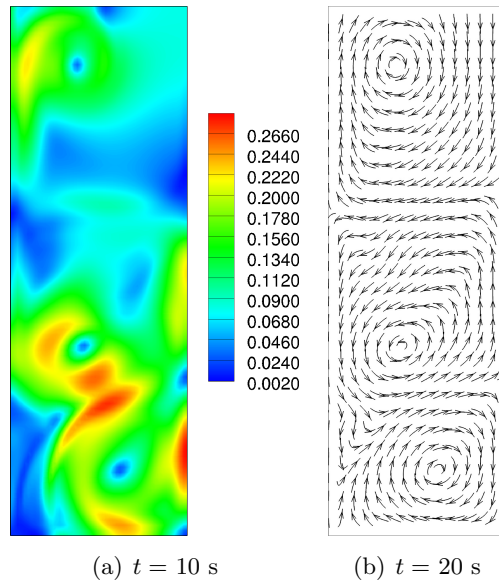


Figure 4.9 Instantaneous contour plots for gas flow rate equal to 8.0 l/min at $t = 60$ s for liquid-phase (a) velocity magnitude ($|\mathbf{U}_1|$, m s^{-1}), (b) velocity vectors.

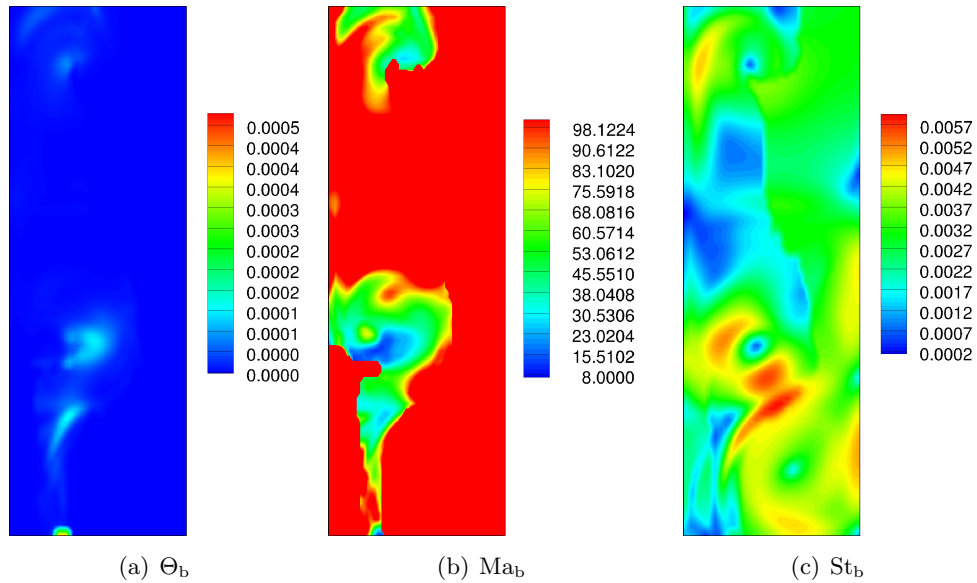


Figure 4.10 Instantaneous contour plots of bubble-phase (a) granular temperature (m s^{-1}), (b) Mach number, (c) Stokes number for gas flow rate equal to 8.0 l/min at $t = 60$ s.

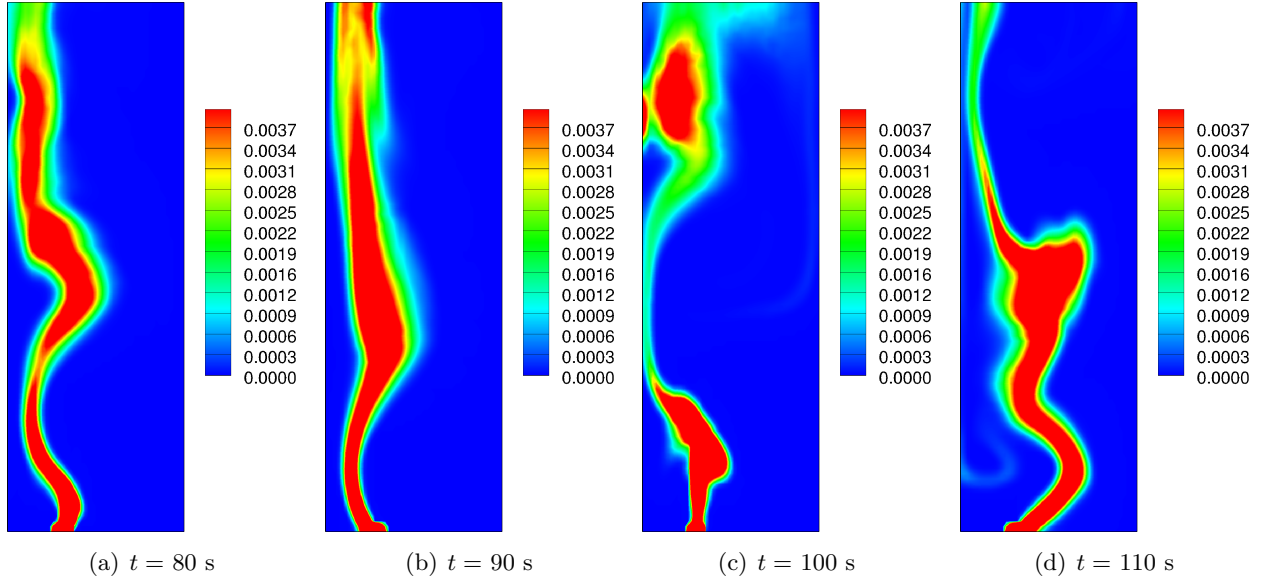


Figure 4.11 Instantaneous contour plots of bubble-phase volume fraction (ε_b) for gas flow rate equal to 8.0 l/min.

gradient, vorticity, drag, virtual mass and gravity are accounted for in the bubble-phase force balance. In this paper, the solution algorithm and coupling procedure are described in detail, and results are presented for a pseudo 2-D bubble column with two different gas flow rates (1.6 and 8.0 l/min). The meandering behavior of the bubble plumes caused by the dynamic interaction between the liquid and bubble phases is observed. Overall, we have demonstrated that the proposed bubbly flow solver is robust and performs satisfactorily under conditions where the two phases are tightly coupled.

Although the main aim of the present work was to demonstrate the implementation of the new model, many improvements and changes can be made to optimize the simulation time as suggested in the paper. Moreover, additional force models can be implemented in a straightforward manner due to the kinetic formulation of the bubble-phase model. Likewise, different boundary conditions can be added to the flow solver in order to simulate more complex flows. For example, a more accurate approach for bubble columns would be to capture the interface between the two phases at the top of the column. These and other improvements, along with the 3-D implementation, will be the subject of future work.

CHAPTER 5. RADIATION TRANSPORT MODELING USING EXTENDED QUADRATURE METHOD OF MOMENTS

A paper submitted to Journal of Computational Physics

Varun Vikas¹, C. D. Hauck, Z. J. Wang, Rodney O. Fox

Abstract

Radiation transport modeling describes the interaction of radiation with scattering and absorbing media. It occurs in a wide variety of phenomena ranging from stellar to terrestrial applications. Over the past few decades, a lot of effort has gone into developing accurate approximation methods for radiation transport modeling. Although, these models give highly accurate results for some systems, they fail to accurately predict the physics for other systems. Almost all of the approximation methods, barring the Monte Carlo method, have some inherent weaknesses as far as the physics is concerned. Recently, an extended quadrature method of moments (EQMOM) was developed to solve uni-variate population balance equations. EQMOM has many favorable properties that makes it suitable for radiation transport modeling. The goal of the current paper is to discuss these properties and demonstrate the successful implementation of EQMOM for radiation transport modeling. The equations governing radiation transport are formulated using EQMOM with special attention to realizability and a set of standard one-dimensional benchmark problems encompassing optically thin, thick and transition regimes is solved. The results look very promising and lay the foundation for extending the same framework to multiple dimensions.

¹Primary researcher and author.

5.1 Introduction

Radiation transport modeling finds application in a wide variety of phenomena ranging from stellar to terrestrial [13, 18, 75, 84]. A very general application is to solar radiation, the most important source of energy for the earth. Another common application is in weather or climate models, where the radiative forcing is calculated for greenhouse gases, aerosols or clouds. Radiation transport modeling for supernovae has been a topic of great interest for astrophysicists. With future interests in space travel, it finds another application in planetary reentry problems. In biomedical sciences, the development of photon radiotherapy techniques and related equipment rely heavily on radiation transport modeling. For the development of bio-renewable fuels, the design of photobioreactors needs accurate radiation transport models for light absorption and scattering by microorganisms such as algae. In the environmental context, radiation transport modeling is important for the efficient design of furnaces to minimize energy loss and pollution emissions.

Radiation transport modeling involves solving two coupled equations. One is a complex integro-differential kinetic transport equation for the specific intensity of radiation and the other is an evolution equation describing the change in internal energy of the material through which the radiation is propagating. The transport equation is extremely difficult to solve because of the high-dimensionality of the independent variable space. A variety of different models [13, 75, 84] have been proposed to numerically solve the transport equation, but there are essentially four major approaches: diffusion approximations, Monte Carlo, discrete-ordinates and moment methods.

In optically thick systems, that are nearly opaque and allow very little light to pass through, the emission/absorption processes drive the radiation intensity to an isotropic distribution, that is, constant in angular space. The constant depends on the material temperature which, in turn, over long time scales satisfies a nonlinear diffusion equation up to an error that is proportional to the ratio of the photon mean free path to the macroscopic length scale. In optically thick systems, this ratio is small and the diffusion approximation [6, 13, 75, 78, 84, 93] provides an accurate representation of the radiation field. However, in optically thin regimes, in which

very little material is present and most of the light passes through, this ratio can be very large. As a result, in optically thin regimes, the diffusion approximation is highly inaccurate. Several extensions have been designed to push the validity of the diffusion approximation into the transition regime, where collisions are frequent enough to give structure to the radiation field, but not enough to validate the diffusion limit. These extensions [1, 12, 53, 61, 62, 106] include non-equilibrium diffusion and flux-limited diffusion. The latter is derived by enforcing the physical property that the radiation flux be bounded by the radiation energy density times the speed of light. The effect is to lessen the diffusion coefficient near steep spatial gradients. Even with these extensions, the validity of the diffusion approximation does not extend much beyond optically thick regimes.

Monte Carlo methods [32, 49] are the community standard-bearer with respect to accuracy. But with that accuracy comes a significant increase in both computational and memory requirements. Individual photons are simulated and then a statistical average is taken to determine the intensity. Due to the finite number of photons, statistical noise is an important issue in determining the accuracy of the computed moments.

The discrete-ordinates model [52, 57, 84], also referred to as the S_N model is the most deterministic method for solving the transport equation numerically. It solves the transport equation along a discrete set of angular directions. These directions are taken from a quadrature set which is used to compute the angular integrals as needed for the moments. The main drawback of the method is the existence of the so called *ray effects*, which are numerical artifacts that arise because the photons move only along directions in the quadrature set. These effects are most pronounced in optically thin materials with localized sources or sharp material discontinuities.

Moment methods track the evolution of a finite number of weighted angular averages of the specific intensity, also known as moments. They require a closure which approximates the specific intensity as a function of the tracked moments. The most common closures are based on spherical harmonic expansions, which are often referred to as the P_N models [66, 90]. These closures result in systems of linear hyperbolic equations for the expansion coefficients. As such this approximation method often leads to negative radiation energy densities, which

are unphysical. However, they do preserve the rotational symmetry of the transport operator. It is this lack of symmetry which leads to ray effects in the discrete-ordinates model.

Defects in the P_N models have led the researchers to look for better closure models [28, 29, 36, 45, 46, 47, 99, 102, 103]. The best performing models are usually nonlinear and are based on closure strategies that, except at very low order (usually the first two moments), involve orders of magnitude increase in the computational overhead. Thus, the search for relatively simple closures which reproduce basic features of the kinetic equations still continues. This is because, in spite of the challenges, moment methods are extremely flexible. Indeed they can be used as stand-alone models, as members of an adaptive hierarchy, as components of a hybrid description and as preconditioners for higher resolution models.

Recently, an extended quadrature method of moments (EQMOM) [127] has been developed to solve uni-variate population balance equations in the context of particle transport in dispersed-phase flows. EQMOM is a moment method that uses quadrature-based closures. EQMOM has certain desirable properties that makes it suitable for radiation transport modeling. The aim of the current paper is to lay a foundation for solving radiation transport problems using EQMOM. The paper formulates the radiation transport problem using EQMOM framework and tests it using a series of one-dimensional benchmark test problems. The current paper only discusses grey (frequency-independent) radiation transport. Non-grey cases will be considered in future work. The results, as discussed later in the paper, look very promising. The remainder of this paper is organized as follows. In Sec. 5.2, the equations of radiative transfer are discussed. Section 5.4 deals with EQMOM. Thereafter, in Sec. 5.4, the solution algorithm is presented. Section 5.5 presents the numerical results for several benchmark test problems. Conclusions from the present study are summarized in Sec. 5.6.

5.2 Equations of radiative transfer

The equation for time-dependent grey radiative transfer [13, 70] in a one-dimensional planar geometry medium with space and temperature dependent opacities is given by

$$\frac{1}{c} \frac{\partial I}{\partial t} + \mu \frac{\partial I}{\partial z} + \sigma_t I = \frac{1}{2} a c \sigma_a T^4 + \frac{1}{2} \sigma_s M^0 + \frac{1}{2} S, \quad (5.1)$$

where $I \equiv I(z, \mu, t)$ is the specific intensity of radiation, $\mu = \cos \theta$ is the internal coordinate associated with the angle (θ) between a photon's direction of flight and the z -axis, $\sigma_a \equiv \sigma_a(z, T)$, $\sigma_s \equiv \sigma_s(z, T)$ and $\sigma_t \equiv \sigma_t(z, T)$ are the absorption, scattering and total opacities respectively, $T \equiv T(z, t)$ is the material temperature and $S \equiv S(z)$ is an isotropic external source of radiation. Note that $\theta \in [0, \pi]$ and $\mu \in [-1, 1]$. The total opacity is the sum of the absorption and the scattering opacities ($\sigma_t = \sigma_a + \sigma_s$). In (5.1), $M^0 \equiv M^0(z, t)$ is the zeroth-order moment of the specific intensity. The p^{th} -order moment of the specific intensity is defined as

$$M^p = \int_{-1}^{+1} \mu^p I d\mu. \quad (5.2)$$

The evolution equation for the internal energy density (e) [13, 70] of the material is given by

$$\frac{\partial e}{\partial t} = \sigma_a M^0 - ac\sigma_a T^4. \quad (5.3)$$

If the material is stationary, as will be assumed in this work, then $e \equiv e(T)$ and $\partial e/\partial t = C_v \partial T/\partial t$ where $C_v \equiv C_v(T) \equiv \partial e/\partial T$ is the heat capacity at constant volume. Applying the definition of moments in (5.2) to (5.1), the moment transport equation for the p^{th} -order moment can be written as

$$\frac{1}{c} \frac{\partial M^p}{\partial t} + \frac{\partial M^{p+1}}{\partial z} + \sigma_t M^p = \left\{ \frac{1}{2} ac\sigma_a T^4 + \frac{1}{2} \sigma_s M^0 + \frac{1}{2} S \right\} \left[\frac{1 - (-1)^{p+1}}{p+1} \right]. \quad (5.4)$$

Putting $p = 0$ gives the transport equation for the zeroth-order moment:

$$\frac{1}{c} \frac{\partial M^0}{\partial t} + \frac{\partial M^1}{\partial z} = ac\sigma_a T^4 - \sigma_a M^0 + S. \quad (5.5)$$

M^0/c and M^1 are often referred to as the radiation energy density and the radiation flux respectively. Note that in the absence of any external source of radiation ($S = 0$),

$$\frac{\partial e}{\partial t} + \frac{1}{c} \frac{\partial M^0}{\partial t} + \frac{\partial M^1}{\partial z} = 0, \quad (5.6)$$

meaning that the net energy in the system is due to the energy crossing the system boundaries.

The discretized equations should also satisfy this property.

The moment transport equations are not closed. The convection term in the evolution equation for each moment involves a higher-order moment. To solve a finite set of moment transport equations, a closure model is needed. In the current work, EQMOM is used for closure. The details of EQMOM are discussed in the next section.

5.3 Extended quadrature method of moments

EQMOM is a moment method that uses quadrature-based closures for reconstructing the specific intensity from the tracked moments. EQMOM combines the most desirable properties of quadrature method of moments (QMOM) [25, 71, 34] and kernel density element method (KDEM) [2], while eliminating their weaknesses. Unlike QMOM that represents the specific intensity as a weighted sum of delta functions, EQMOM uses a weighted sum of known non-negative kernel density functions which is similar to the representation used for KDEM. However, KDEM is more expensive as it solves a multivariate constrained least-squares problem to compute the multiple unknown parameters whereas EQMOM uses a one-dimensional root-finding method. Moreover only a few of the lowest-order moments are exactly reproduced by KDEM. EQMOM also holds an upper hand over the entropy-based closure models [45, 47, 74]. Just like KDEM, entropy-based closure models have to solve a multivariate constrained least-squares problem. In addition, the extension of the entropy-based closure models to the boundary of moment space is ill-conditioned [67]. At the boundary of the moment space, EQMOM reduces to QMOM in a well-conditioned manner, making it possible to easily reconstruct the specific intensity all the way to the boundary of the moment space.

EQMOM uses two successive quadrature approximations to reconstruct the specific intensity from the tracked moments. These successive approximations are referred to as *primary* and *secondary* quadratures. In the discussion below, N nodes are used for primary quadrature and M nodes are used for secondary quadrature per primary node. The number of secondary quadrature nodes should always be greater than the number of primary quadrature nodes ($M > N$). For the N -node primary quadrature, the specific intensity is represented as a weighted sum of N smooth kernel density functions:

$$I = \sum_{\alpha=1}^N w_{\alpha} \delta_{\sigma}(\mu, \mu_{\alpha}). \quad (5.7)$$

Note that in the discrete-ordinates model (just like QMOM), the smooth kernel density functions are replaced by the delta functions, thereby allowing radiation transport only in a finite number of pre-specified directions. In EQMOM, the smooth kernel density functions allow radiation transport in all directions. In (5.7), w_{α} and μ_{α} ($\alpha \in [1, 2, \dots, N]$) are called the primary

quadrature weights and abscissas respectively and σ is a measure of the spread of the individual smooth kernel density functions. Note that the same σ is used for each of the N kernel density functions. The kernel density functions $\delta_\sigma(\mu, \mu_\alpha)$ should be defined over $[-1, 1]$. In this work, each smooth kernel density function is chosen to be a beta distribution function:

$$\delta_\sigma(\mu, \mu_\alpha) = \frac{1}{2B(\xi_\alpha, \eta_\alpha)} \left(\frac{\mu+1}{2}\right)^{\xi_\alpha-1} \left(\frac{1-\mu}{2}\right)^{\eta_\alpha-1}, \quad (5.8)$$

where $B(\xi_\alpha, \eta_\alpha)$ is the beta function and the two parameters are $\xi_\alpha = (\mu_\alpha + 1)/(2\sigma)$ and $\eta_\alpha = (1 - \mu_\alpha)/(2\sigma)$. This form of EQMOM is called beta-EQMOM, but in the current paper it will simply be referred to as EQMOM. Note that a uniform distribution in the θ -space leads to a beta distribution in the μ -space. As EQMOM uses beta distribution as the kernel density function, it can easily recover a uniform distribution in the θ -space. Moreover, with appropriate choice of parameters ($\xi_\alpha = 1$ and $\eta_\alpha = 1$), a uniform distribution in the μ -space can also be recovered. In order to reconstruct I , $2N + 1$ parameters ($[w_\alpha \mu_\alpha] \forall \alpha \in [1, 2, \dots, N]$ and σ) are needed. To find these $2N + 1$ unknowns, the first $2N + 1$ moments ($M^p \forall p \in [0, 1, \dots, 2N]$) are tracked. A very efficient and robust inversion algorithm to compute the unknown parameters from the tracked moments has already been developed in [127]. This inversion algorithm combines the moment inversion algorithm for QMOM with a one dimensional root finding algorithm that solves for σ . As only a finite number of moments is tracked, multiple solutions are possible for primary quadrature. The current approach is to find the solution with the smallest value of σ .

Another important advantage of EQMOM is the ability to construct a second Gaussian quadrature [38] with respect to the kernel density function. For the secondary quadrature, each kernel density function is written as a weighted sum of delta functions:

$$\delta_\sigma(\mu, \mu_\alpha) = \sum_{\beta=1}^M \rho_{\alpha\beta} \delta(\mu - \mu_{\alpha\beta}). \quad (5.9)$$

This form changes all the integrals in the μ -space to summations thereby simplifying the flux calculations, when using the finite-volume approach. Moreover, this form is essential for the use of realizable schemes in [115]. In (5.9), $\rho_{\alpha\beta}$ and $\mu_{\alpha\beta}$ are obtained from the weights and abscissas of the Gauss-Jacobi quadrature. Substituting (5.9) in (5.7) gives the final form of the

specific intensity:

$$I = \sum_{\alpha=1}^N \sum_{\beta=1}^M w_{\alpha\beta} \delta(\mu - \mu_{\alpha\beta}), \quad (5.10)$$

where $w_{\alpha\beta} = w_{\alpha} \rho_{\alpha\beta}$ and $\mu_{\alpha\beta}$ ($\alpha \in [1, 2, \dots, N]$ and $\beta \in [1, 2, \dots, M]$) are called secondary weights and abscissas respectively. It is important to understand that although the final form (5.10) expresses the specific intensity as a weighted sum of delta functions, this is not same as the discrete-ordinates model. This form is just used to facilitate the flux computation and guarantee realizability. If $M > N$, values of the tracked moments computed with the smooth formulation (5.7) are the same as those computed using the final delta formulation (5.10).

To summarize, the moment-inversion algorithm for EQMOM involves two stages. In the first stage, the primary quadrature information is obtained from the tracked moments and in the second stage, the secondary quadrature information is obtained from the primary quadrature information. This can be depicted as:

$$[M^0, M^1, \dots, M^{2N}] \xrightarrow{\text{Primary quadrature}} [w_{\alpha}, \mu_{\alpha}, \sigma] \xrightarrow{\text{Secondary quadrature}} [w_{\alpha\beta}, \mu_{\alpha\beta}] \quad (5.11)$$

where $\alpha \in [1, 2, \dots, N]$ and $\beta \in [1, 2, \dots, M]$. A detailed description of EQMOM can be found in [127].

Before moving onto the next section, here is a brief summary of the properties that make EQMOM a better option compared to the already existing models. As mentioned earlier, unlike the discrete-ordinates model, EQMOM allows radiation transport in all directions. Unlike KDEM and entropy-based closure models, EQMOM has a robust inversion algorithm that avoids the computational cost of solving a multivariate constrained least-squares problem. EQMOM can easily reconstruct the specific intensity all the way to the boundary of the moment space which is not often possible with the entropy-based closure models. When EQMOM is used in conjugation with the realizable discretization schemes, the non-negativity of the specific intensity is guaranteed, thereby avoiding the negative radiation energy density problem encountered by the spherical harmonics model. EQMOM can achieve the maximum radiation transport speed of c even with a single primary node. This property does not hold for the low order spherical harmonics models, in particular the P_1 model. The system of evolutions equations for EQMOM have distinct eigenvalues that preserve the hyperbolic nature of radiation

transport. Also, EQMOM is much less expensive compared to the Monte Carlo simulations and is not be subject to statistical noise. More discussion on the comparison of EQMOM with other models is given in Sec. 5.5.

5.4 Solution algorithm

The aim of the current paper is to demonstrate the effectiveness of EQMOM for radiation transport modeling. Development of efficient spatial and temporal discretization schemes for EQMOM applied to radiation transport modeling will be considered as a part of future work. In the current work, the equations are discretized using the finite-volume approach [60]. A semi-implicit time-integration scheme, adapted from [70] is used. The convection and the external source terms are treated explicitly while the material coupling terms are linearized and treated implicitly. The conservation of the net energy is satisfied in discrete form. In addition, the realizability of the moment set is guaranteed at each step using appropriate realizable schemes and realizability criteria. This is essential for the success of the moment-inversion algorithm. With a non-realizable moment set, the moment-inversion algorithm may lead to the weights that are negative and the abscissas that lie outside the support interval $([-1, 1])$, which are unphysical. A realizable moment set always guarantees a non-negative specific intensity thereby leading to a non-negative radiation energy density. The details of the treatment of different terms are given below. First the convection term is treated, followed by the external source term and eventually the effect of the material coupling terms is included:

$$M_i^{p,n} \xrightarrow{\text{Convection term}} M_i^{p,(1)} \xrightarrow{\text{External source term}} M_i^{p,(2)} \xrightarrow{\text{Material coupling terms}} M_i^{p,n+1}. \quad (5.12)$$

5.4.1 Convection term

For the convection term, the first-order Euler explicit time-integration is used. The discretized equation can be written as

$$M_i^{p,(1)} = M_i^{p,n} - \frac{c\Delta t}{\Delta z} \left[G_{i+1/2}^{p,n} - G_{i-1/2}^{p,n} \right], \quad (5.13)$$

where $M_i^{p,n}$ is the p^{th} -order cell-averaged moment in the i^{th} cell at time level n , Δt is the time step size and Δz is the cell size. $G_{i+1/2}^{p,n}$ and $G_{i-1/2}^{p,n}$ are the numerical fluxes at the faces $i+1/2$

and $i - 1/2$ respectively. The numerical flux is evaluated using a kinetic approach:

$$G_{i+1/2}^{p,n} = \int_{-1}^{+1} \min(\mu, 0) \mu^p I_{i+1/2,r}^n d\mu + \int_{-1}^{+1} \max(\mu, 0) \mu^p I_{i+1/2,l}^n d\mu, \quad (5.14)$$

where $I_{i+1/2,l}^n$ and $I_{i+1/2,r}^n$ are the reconstructed specific intensities at the left and right sides of the face $i + 1/2$ respectively. This kinetic treatment of numerical flux is essential to allow for a two-way radiation transport across the face. The specific intensity in the i^{th} cell can be written as

$$I_i^n = \sum_{\alpha=1}^N \sum_{\beta=1}^M w_{\alpha\beta,i}^n \delta(\mu - \mu_{\alpha\beta,i}^n), \quad (5.15)$$

where $w_{\alpha\beta,i}^n$ and $\mu_{\alpha\beta,i}^n$ are the secondary weights and abscissas in the i^{th} cell respectively. The reconstructed specific intensities at the left and right sides of the face $i + 1/2$ can be written as

$$\begin{aligned} I_{i+1/2,l}^n &= \sum_{\alpha=1}^N \sum_{\beta=1}^M w_{\alpha\beta,i+1/2,l}^n \delta(\mu - \mu_{\alpha\beta,i+1/2,l}^n) \quad \text{and} \\ I_{i+1/2,r}^n &= \sum_{\alpha=1}^N \sum_{\beta=1}^M w_{\alpha\beta,i+1/2,r}^n \delta(\mu - \mu_{\alpha\beta,i+1/2,r}^n) \end{aligned} \quad (5.16)$$

respectively. Using (5.16), the numerical flux at the face $i + 1/2$ is written as

$$\begin{aligned} G_{i+1/2}^{p,n} &= \sum_{\alpha=1}^N \sum_{\beta=1}^M w_{\alpha\beta,i+1/2,r}^n \min(\mu_{\alpha\beta,i+1/2,r}^n, 0) (\mu_{\alpha\beta,i+1/2,r}^n)^p \\ &+ \sum_{\alpha=1}^N \sum_{\beta=1}^M w_{\alpha\beta,i+1/2,l}^n \max(\mu_{\alpha\beta,i+1/2,l}^n, 0) (\mu_{\alpha\beta,i+1/2,l}^n)^p. \end{aligned} \quad (5.17)$$

The weights and abscissas at the left and right sides of the faces are reconstructed using the cell values. To guarantee the realizability of the moment set, only piecewise constant reconstruction of abscissas is allowed [115]:

$$\mu_{\alpha\beta,i+1/2,l}^n = \mu_{\alpha\beta,i}^n \quad \text{and} \quad \mu_{\alpha\beta,i+1/2,r}^n = \mu_{\alpha\beta,i+1}^n. \quad (5.18)$$

For the weights, any high-order reconstruction can be used. In the current paper, piecewise linear reconstruction is employed for the weights, leading to the *quasi-2nd*-order scheme in [115]. The minmod limiter [56] is used while computing the slope of the linear profile to avoid any spurious oscillations. Note that all the moments updated using (5.13) correspond to a unique

update of the specific intensity:

$$\begin{aligned}
I_i^{(1)} &= \sum_{\alpha=1}^N \sum_{\beta=1}^M \left[w_{\alpha\beta,i}^n - \frac{c\Delta t}{\Delta z} \left(w_{\alpha\beta,i+1/2,l}^n \max(\mu_{\alpha\beta,i}^n, 0) - w_{\alpha\beta,i-1/2,r}^n \min(\mu_{\alpha\beta,i}^n, 0) \right) \right] \delta(\mu - \mu_{\alpha\beta,i}^n) \\
&\quad - \frac{c\Delta t}{\Delta z} \sum_{\alpha=1}^N \sum_{\beta=1}^M w_{\alpha\beta,i+1/2,r}^n \min(\mu_{\alpha\beta,i+1}^n, 0) \delta(\mu - \mu_{\alpha\beta,i+1}^n) \\
&\quad + \frac{c\Delta t}{\Delta z} \sum_{\alpha=1}^N \sum_{\beta=1}^M w_{\alpha\beta,i-1/2,l}^n \max(\mu_{\alpha\beta,i-1}^n, 0) \delta(\mu - \mu_{\alpha\beta,i-1}^n).
\end{aligned} \tag{5.19}$$

The non-negativity of the updated specific intensity can be guaranteed if the time step size satisfies the realizability criterion given by

$$\Delta t \leq \frac{w_{\alpha\beta,i}^n \Delta z}{c \left(w_{\alpha\beta,i+1/2,l}^n \max(\mu_{\alpha\beta,i}^n, 0) - w_{\alpha\beta,i-1/2,r}^n \min(\mu_{\alpha\beta,i}^n, 0) \right)} \tag{5.20}$$

$\forall \alpha \in [1, 2, \dots, N]$ and $\beta \in [1, 2, \dots, M]$. More details about the realizability criterion can be found in [115]. In addition to the realizability criterion, the time step size should also satisfy the CFL condition for stability:

$$\Delta t \leq \text{CFL} \frac{\Delta z}{c |\mu_{\alpha\beta,i}^n|} \tag{5.21}$$

$\forall \alpha \in [1, 2, \dots, N]$ and $\beta \in [1, 2, \dots, M]$. Note that (5.20) is exactly same as (5.21) if piecewise constant reconstruction is used for weights instead of piecewise linear reconstruction. In the current work, CFL = 0.3 is used for all the numerical simulations, unless otherwise stated.

5.4.2 External source term

In the current work, the external source is only a function of spatial coordinate. It is treated using the first-order Euler explicit time-integration scheme:

$$M_i^{p,(2)} = M_i^{p,(1)} + \frac{c\Delta t}{2} S_i \left[\frac{1 - (-1)^{p+1}}{p+1} \right]. \tag{5.22}$$

The updated moment set corresponds to the following unique update of the specific intensity:

$$I_i^{(2)} = I_i^{(1)} + \frac{c\Delta t}{2} S_i. \tag{5.23}$$

The non-negativity of the updated specific intensity is guaranteed as long as the external source is non-negative.

5.4.3 Material coupling terms

The algorithm for the implicit treatment of the material coupling terms is adapted from [70]. The moment transport equation in (5.4), without the convection and the external source terms, and the material energy equation in (5.3) are discretized using the first-order Euler implicit time-integration scheme:

$$\frac{M_i^{p,n+1} - M_i^{p,(2)}}{c\Delta t} = -\sigma_{t,i}^n M_i^{p,n+1} + \left\{ \frac{1}{2} ac\sigma_{a,i}^n (T_i^{n+1})^4 + \frac{1}{2} \sigma_{s,i}^n M_i^{0,n+1} \right\} \left[\frac{1 - (-1)^{p+1}}{p+1} \right], \quad (5.24)$$

$$\frac{e_i^{n+1} - e_i^n}{\Delta t} = \sigma_{a,i}^n M_i^{0,n+1} - ac\sigma_{a,i}^n (T_i^{n+1})^4. \quad (5.25)$$

Note that the opacities are treated explicitly. For $p = 0$, (5.24) becomes

$$\frac{M_i^{0,n+1} - M_i^{0,(2)}}{c\Delta t} = -\sigma_{a,i}^n M_i^{0,n+1} + ac\sigma_{a,i}^n (T_i^{n+1})^4. \quad (5.26)$$

The nonlinearities in the T^4 terms are treated using the equivalent of one Newton iteration. To perform this linearization, $(T_i^{n+1})^4$ and e_i^{n+1} are expanded using Taylor series:

$$(T_i^{n+1})^4 \approx (T_i^n)^4 + 4(T_i^n)^3(T_i^{n+1} - T_i^n), \quad (5.27)$$

$$e_i^{n+1} \approx e_i^n + C_v^n (T_i^{n+1} - T_i^n). \quad (5.28)$$

Substituting (5.27) in (5.28) and then putting the result in (5.25) yields

$$(T_i^{n+1})^4 \approx \frac{f_i^n}{ac} \left[ac(T_i^n)^4 + \sigma_{a,i}^n \beta_i^n \Delta t M_i^{0,n+1} \right] \quad (5.29)$$

where $\beta_i^n = 4ac(T_i^n)^3/C_{v,i}^n$ and $f_i^n = 1/(1 + \sigma_{a,i}^n \beta_i^n \Delta t)$. Substituting (5.29) in (5.24) gives

$$\begin{aligned} \frac{M_i^{p,n+1} - M_i^{p,(2)}}{c\Delta t} = & -\sigma_{t,i}^n M_i^{p,n+1} + \left\{ \frac{1}{2} ac\sigma_{a,i}^n f_i^n (T_i^n)^4 \right. \\ & \left. + \frac{1}{2} \sigma_{a,i}^n f_i^n \sigma_{a,i}^n \beta_i^n \Delta t M_i^{0,n+1} + \frac{1}{2} \sigma_{s,i}^n M_i^{0,n+1} \right\} \left[\frac{1 - (-1)^{p+1}}{p+1} \right] \end{aligned} \quad (5.30)$$

Putting $p = 0$ and performing some simplifications, following equation for the zeroth-order moment is obtained:

$$\frac{M_i^{0,n+1} - M_i^{0,(2)}}{c\Delta t} = -f_i^n \sigma_{a,i}^n \left[M_i^{0,n+1} - ac(T_i^n)^4 \right]. \quad (5.31)$$

This equation is used for updating the zeroth-order moment. Rest of the moments are then updated using (5.30). Substituting (5.29) in (5.25) yields

$$\frac{e_i^{n+1} - e_i^n}{\Delta t} = f_i^n \sigma_{a,i}^n \left[M_i^{0,n+1} - ac(T_i^n)^4 \right]. \quad (5.32)$$

This is used to update the material internal energy density. Note that

$$\frac{M_i^{0,n+1} - M_i^{0,(2)}}{c\Delta t} + \frac{e_i^{n+1} - e_i^n}{\Delta t} = 0. \quad (5.33)$$

Hence, the discretization method conserves the net energy. Using (5.30), the unique update of the specific intensity can be written as

$$I_i^{n+1} = \frac{1}{1 + c\Delta t\sigma_{t,i}^n} \left[I_i^{(2)} + \frac{1}{2}c\Delta t\sigma_{a,i}^n f_i^n \left\{ ac(T_i^n)^4 + \sigma_{a,i}^n \beta_i^n \Delta t M_i^{0,n+1} \right\} + \frac{1}{2}c\Delta t\sigma_{s,i}^n M_i^{0,n+1} \right]. \quad (5.34)$$

All the terms on the right hand side are non-negative, thereby guaranteeing the non-negativity of the updated specific intensity and hence the realizability of the moment set at the time level $n + 1$.

5.5 Numerical results

In this section, results are presented for some standard benchmark problems encompassing optically thin, thick and transition regimes. For simplicity, the units of all the quantities are given in Table 5.1 and hereafter all the units will be dropped while specifying the values of the quantities. The domain of the problems is defined by $z \in [z_{LB}, z_{RB}]$. Material coupling is only required for the last two problems - the Marshak wave problem and the Su-Olson problem. The two constants used in the problems are the speed of sound ($c = 3 \times 10^{10}$ cm/s) and the radiation constant ($a = 1.372 \times 10^{14}$ erg/cm³/keV⁴). For all the problems, results are presented for EQMOM with number of primary nodes from 1 through 5. Currently, any increase beyond 5 makes the round-off errors dominant. An improvement of the EQMOM algorithm to suppress the round-off errors when the number of primary nodes is increased beyond 5 will be considered as a part of future work. For, each primary node, the number of secondary nodes has been chosen such that any further increase leaves the solution almost unchanged. In all the discussions below, EQMOM-NxM refers to EQMOM with N primary nodes and M secondary

nodes per primary node. For all the problems, results are presented on successively refined grids to show the general trend of grid convergence of the EQMOM solutions.

Table 5.1 Quantities and units.

Quantity	Unit	Quantity	Unit
z	cm	σ_a	$1/cm$
σ_s	$1/cm$	σ_t	$1/cm$
t	s	S	$erg/cm^3/s$
T	keV	C_v	$erg/cm^3/keV$
e	erg/cm^3	I	$erg/cm^2/s$
M^p	$erg/cm^2/s$		

5.5.1 Plane-source problem

The plane-source problem [47] is a torture test for a model to handle very strong discontinuities. The scattering and absorption opacities are given by $\sigma_s = 1$ and $\sigma_a = 0$ respectively. There is no external source of radiation ($S = 0$). The specific intensity and the corresponding moments at $t = 0$ are given by

$$I(z, \mu) = 0.5\delta(z) + 0.00005 \quad \text{and} \quad M^p(z) = (0.5\delta(z) + 0.00005) \left[\frac{1 - (-1)^{p+1}}{p+1} \right] \quad (5.35)$$

respectively. Note that a small positive baseline value is used as in [47]. However, the method works with zero baseline value as well. The left boundary is located at $z_{\text{LB}} = 0$. Three different cases are simulated with final times of $ct = 1, 2$ and 4 with the corresponding right boundaries located at $z_{\text{RB}} = 1.1, 2.1$ and 4.1 respectively. Reflective boundary condition is applied at the left boundary:

$$I_{\text{LB},l}(\mu) = I_{\text{LB},r}(-\mu) \quad \text{and} \quad M_{\text{LB},l}^p = (-1)^p M_{\text{LB},r}^p. \quad (5.36)$$

At the right boundary, Dirichlet boundary condition with a fixed baseline specific intensity value is applied:

$$I_{\text{RB},r}(\mu) = 0.00005 \quad \text{and} \quad M_{\text{RB},r}^p = 0.00005 \left[\frac{1 - (-1)^{p+1}}{p+1} \right]. \quad (5.37)$$

Note that the boundary conditions are applied at the left side of the leftmost face and the right side of the rightmost face.

Figure 5.1 shows the results at $ct = 1$ with 220, 440 and 880 cells. The semi-analytic solution is obtained from [37]. The oscillations, also referred to as the *wave effects*, in the solutions are due to the photons traveling in waves at the speeds determined by the finite number of eigenvalues of the system. The spherical harmonics [47] and discrete-ordinates models show similar oscillations, however the oscillations there are more pronounced. Moreover, unlike spherical harmonics model, the oscillations never lead to the problem of negative density as the non-negativity is guaranteed by the use of the realizable discretization schemes. Increasing the number of primary nodes increases the number of eigenvalues thereby adding more oscillatory lobes. At the same time the magnitude of oscillation around the semi-analytic solution seems to decrease by adding more primary nodes. In particular, the magnitude of oscillations for the EQMOM-4x10 solution is less than the EQMOM-2x6 solution and the magnitude of oscillations for the EQMOM-5x12 solution is less than the EQMOM-3x8 solution. The magnitude of the oscillations can be decreased further if the use of more primary nodes becomes feasible. Another possible option to decrease the magnitude of oscillations is to choose the primary quadrature solution that corresponds to a larger value of σ . This option will be explored in future work. The maximum radiation transport speed of c is achieved by EQMOM even with one primary node. This is not a property of low order spherical harmonics models, in particular the P_1 model. Figure 5.2 shows the results at $ct = 2$ with 300, 600 and 1200 cells and Figure 5.3 shows the results at $ct = 4$ with 410, 820 and 1640 cells. As time progresses, the effect of scattering becomes dominant and the oscillation are reduced to a great extent.

5.5.2 Two-beam instability problem

The two-beam instability problem [47] is designed to test a closure's ability to handle multi-modal distributions. The closure that is unable to handle particles moving in opposing directions produces a shock in the steady state profile. The scattering and absorption opacities are given by $\sigma_s = 0$ and $\sigma_a = 2$ respectively. There is no external source of radiations ($S = 0$). The specific intensity and the corresponding moments at $t = 0$ are given by

$$I(z, \mu) = 0.00005 \quad \text{and} \quad M^p(z) = 0.00005 \left[\frac{1 - (-1)^{p+1}}{p + 1} \right] \quad (5.38)$$

respectively. The left and right boundaries are located at $z_{\text{LB}} = 0$ and $z_{\text{RB}} = 0.5$ respectively. Reflective boundary condition is applied at the left boundary:

$$I_{\text{LB},l}(\mu) = I_{\text{LB},r}(-\mu) \quad \text{and} \quad M_{\text{LB},l}^p = (-1)^p M_{\text{LB},r}^p. \quad (5.39)$$

At the right boundary, Dirichlet boundary condition with a fixed baseline specific intensity value is applied:

$$I_{\text{RB},r}(\mu) = 0.5 \quad \text{and} \quad M_{\text{RB},r}^p = 0.5 \left[\frac{1 - (-1)^{p+1}}{p+1} \right]. \quad (5.40)$$

Figure 5.4 shows the steady state results with 100, 200 and 400 cells. The semi-analytic solution is obtained from [47]. EQMOM with one primary node is not able to resolve this problem. However, increase the number of primary nodes, the EQMOM solution quickly approaches the semi-analytic solution. None of the results show the appearance of any shock.

5.5.3 Reed cell problem

The Reed cell problem [89, 14] is a demanding problem with regions in which the specific intensity takes isotropic, highly peaked and intermediate forms. This problem tests a model's ability to deal with regions of greatly differing characteristics. The left and right boundaries are located at $z_{\text{LB}} = 0$ and $z_{\text{RB}} = 8$ respectively. The space between the two boundaries is divided into five regions. The opacities and the external source terms in these regions are given in Table 5.2. The specific intensity and the corresponding moments at $t = 0$ are given by

Table 5.2 Opacities and external source terms for the Reed cell problem.

Region	σ_a	σ_s	S
$z \in (0, 2)$	50.0	0.0	50.0
$z \in (2, 3)$	5.0	0.0	0.0
$z \in (3, 5)$	0.0001	0.0	0.0
$z \in (5, 7)$	0.1	0.9	1.0
$z \in (7, 8)$	0.1	0.9	0.0

$I(z, \mu) = 0$ and $M^p(z) = 0$ respectively. Reflective boundary condition is applied at the left boundary:

$$I_{\text{LB},l}(\mu) = I_{\text{LB},r}(-\mu) \quad \text{and} \quad M_{\text{LB},l}^p = (-1)^p M_{\text{LB},r}^p. \quad (5.41)$$

At the right boundary, vacuum boundary condition is applied:

$$I_{\text{RB},r}(\mu) = \begin{cases} I_{\text{RB},l}(\mu), & \text{if } \mu > 0, \\ 0, & \text{otherwise.} \end{cases} \quad (5.42)$$

$M_{\text{RB},r}^p$ is computed accordingly.

Figure 5.5 shows the steady state results with 100, 200 and 400 cells. The reference solution is obtained from [14] which used a spherical harmonic P_{17} angular approximation and a regular spatial finite element mesh consisting of 400 elements. As the number of primary nodes is increased, the EQMOM solution approaches the reference solution. It seems that with 6 primary nodes, EQMOM may be able to completely resolve the reference solution. As mentioned earlier, increase of the number of primary nodes beyond 5 will be considered a part of future work.

5.5.4 Marshak wave problem

The Marshak wave problem [70] is an absorption dominant diffusive problem. The transport solution and the diffusion solution are expected to be the same for this problem. The scattering and absorption opacities are given by $\sigma_s = 0$ and $\sigma_a = 300/T^3$ respectively. There is no external source of radiations ($S = 0$). Initially, radiation is in equilibrium with the material. The temperature, the specific intensity and the corresponding moments at $t = 0$ are given by

$$T(z) = 10^{-9}, \quad I(z, \mu) = \frac{1}{2}ac \times 10^{-36} \quad \text{and} \quad M^p(z) = \frac{1}{2}ac \times 10^{-36} \times \left[\frac{1 - (-1)^{p+1}}{p+1} \right] \quad (5.43)$$

respectively. The heat capacity is given by $C_v = 3 \times 10^{15}$. The left and right boundaries are located at $z_{\text{LB}} = 0$ and $z_{\text{RB}} = 0.6$ respectively. Dirichlet boundary condition is applied at the left boundary by fixing the temperature:

$$T_{\text{LB},l} = 1.0, \quad I_{\text{LB},l}(\mu) = \frac{1}{2}ac \quad \text{and} \quad M_{\text{LB},l}^p = \frac{1}{2}ac \left[\frac{1 - (-1)^{p+1}}{p+1} \right]. \quad (5.44)$$

At the right boundary, vacuum boundary condition is applied:

$$I_{\text{RB},r}(\mu) = \begin{cases} I_{\text{RB},l}(\mu), & \text{if } \mu > 0, \\ 0, & \text{otherwise.} \end{cases} \quad (5.45)$$

$M_{\text{RB},r}^p$ is computed accordingly.

Figure 5.6 shows the results at $ct = 300, 1500$ and 3000 . The semi-analytic solution is obtained from [83]. Three successively refined grids with 30, 60 and 120 cells are used. As this is a diffusion limit problem, EQMOM with just one primary node is able to resolve the problem. Any increase in the number of primary nodes, does not change the solution. The EQMOM solution approaches the semi-analytic solution as the grid is refined. However, on relatively coarse grids, the wave front is not captured properly. This is the defect of the discretization scheme rather than the EQMOM. To capture the wave front, the discretization scheme should preserve the asymptotic diffusion limit [6, 54, 55, 59, 70]. The discretization scheme used here is not asymptotic preserving. However, it must be reiterated that the aim of the current paper is to demonstrate the application of EQMOM to radiation transport modeling. The development of discretization schemes for EQMOM that are asymptotic preserving will be considered in future work.

5.5.5 Su-Olson problem

The Su-Olson problem [78] is a non-equilibrium radiative transfer problem. The scattering and absorption opacities are given by $\sigma_s = 0$ and $\sigma_a = 1$ respectively. The external source of radiation is given by

$$S = \begin{cases} ac, & \text{if } 0 \leq x \leq 0.5 \quad \text{and} \quad 0 \leq ct \leq 10, \\ 0, & \text{otherwise.} \end{cases} \quad (5.46)$$

Initially, radiation is in equilibrium with the material. The temperature, the specific intensity and the corresponding moments at $t = 0$ are given by

$$T(z) = 10^{-2.5}, \quad I(z, \mu) = \frac{1}{2}ac \times 10^{-10} \quad \text{and} \quad M^p(z) = \frac{1}{2}ac \times 10^{-10} \times \left[\frac{1 - (-1)^{p+1}}{p+1} \right] \quad (5.47)$$

respectively. The heat capacity is given by $C_v = 4aT^3$. The left and right boundaries are located at $z_{\text{LB}} = 0$ and $z_{\text{RB}} = 30$ respectively. Reflective boundary condition is applied at the left boundary:

$$I_{\text{LB},l}(\mu) = I_{\text{LB},r}(-\mu) \quad \text{and} \quad M_{\text{LB},l}^p = (-1)^p M_{\text{LB},r}^p. \quad (5.48)$$

Dirichlet boundary condition is applied at the right boundary by fixing the temperature:

$$T_{\text{RB},r} = 10^{-2.5}, \quad I_{\text{RB},r}(\mu) = \frac{1}{2}ac \times 10^{-10} \quad \text{and} \quad M_{\text{RB},r}^p = \frac{1}{2}ac \times 10^{-10} \times \left[\frac{1 - (-1)^{p+1}}{p+1} \right]. \quad (5.49)$$

Figure 5.7 shows the results at $ct = 1, 3.16$ and 10 . Figure 5.8 shows the same results on a logarithmic scale. The semi-analytic solution is obtained from [105]. Three successively refined grids with 240, 480 and 960 cells are used. With increase in the number of primary nodes, the EQMOM solution closely resembles the semi-analytic solution.

5.6 Conclusions

The equations for radiation transport modeling have been formulated using EQMOM with special attention to realizability and a set of standard one-dimensional benchmark problems encompassing optically thin, thick and transition regimes has been solved. The results look very promising and lay the foundation for extending the same framework to multiple dimensions. An improvement of the EQMOM algorithm to suppress the round-off errors when increasing the number of primary nodes beyond 5 is needed. High-order accurate realizable spatial and temporal discretization schemes that preserve the asymptotic diffusion limit are to be developed. Furthermore, for multiple dimensions, a bi-variate version of EQMOM is needed. These tasks will be undertaken in future work.

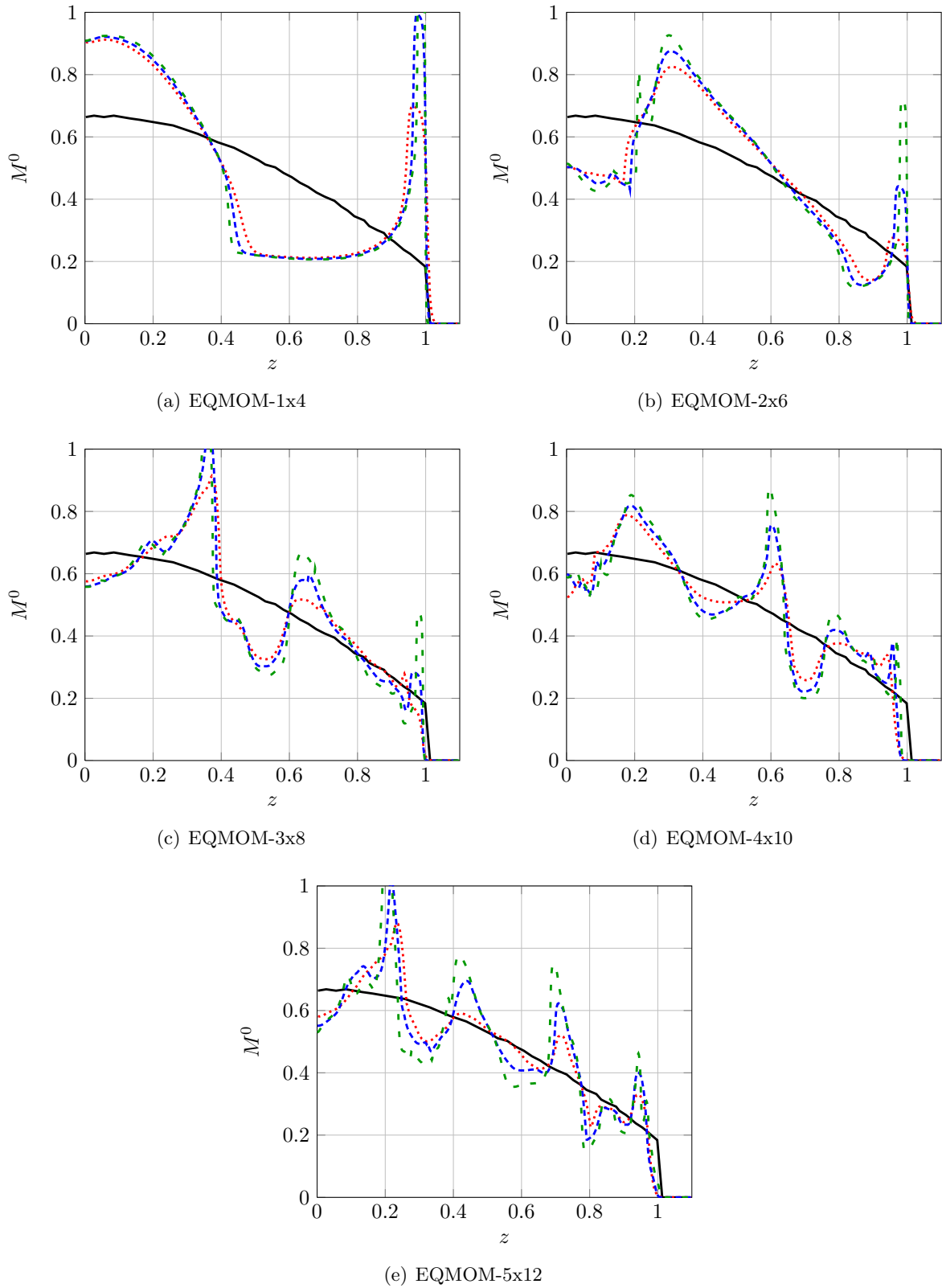


Figure 5.1 Solutions for the plane-source problem at $ct = 1$: Semi-analytic (—), 220 cells (.....), 440 cells (- - -), 880 cells (- - -).

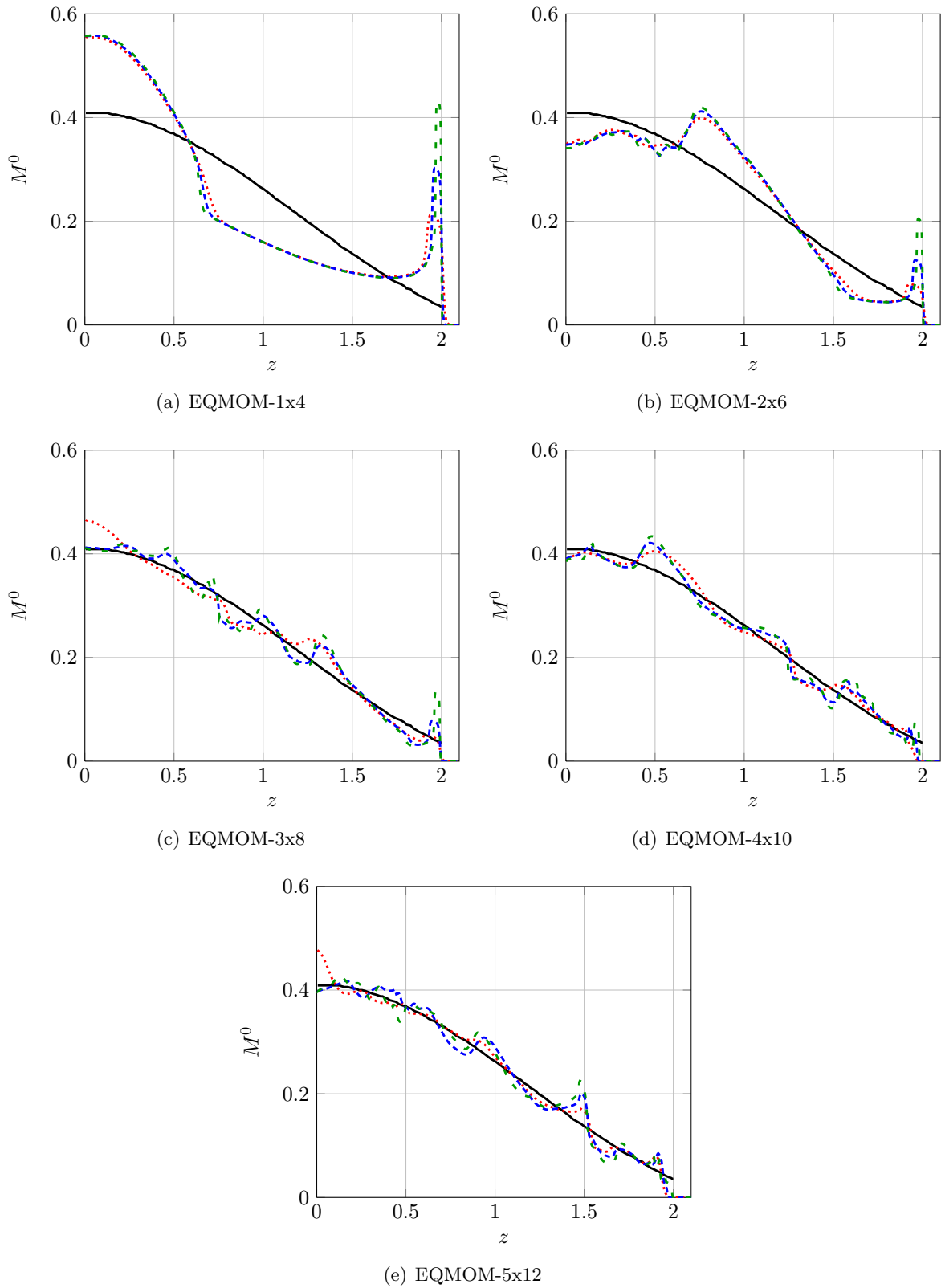


Figure 5.2 Solutions for the plane-source problem at $ct = 2$: Semi-analytic (—), 300 cells (.....), 600 cells (---), 1200 cells (-.-).

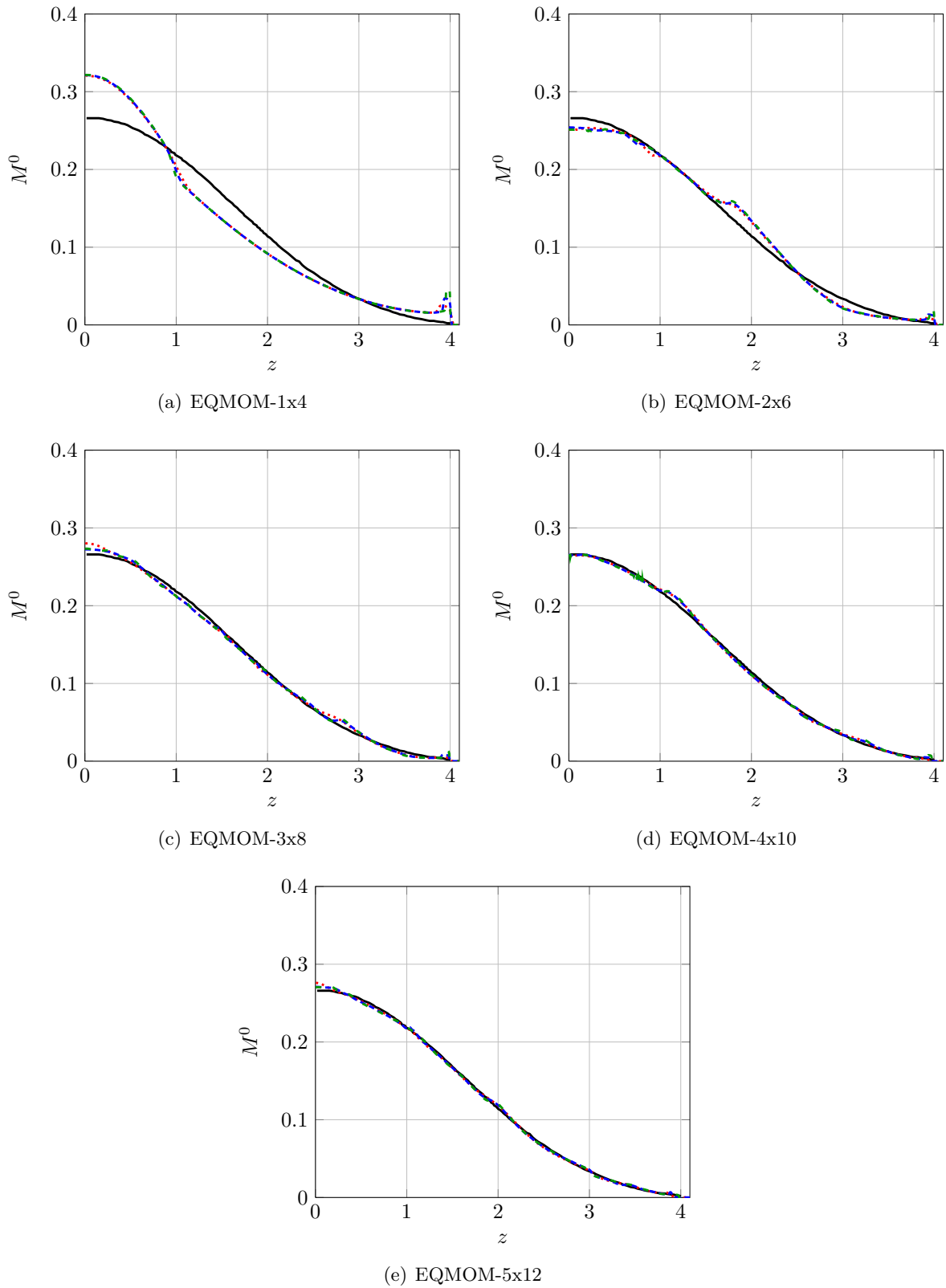
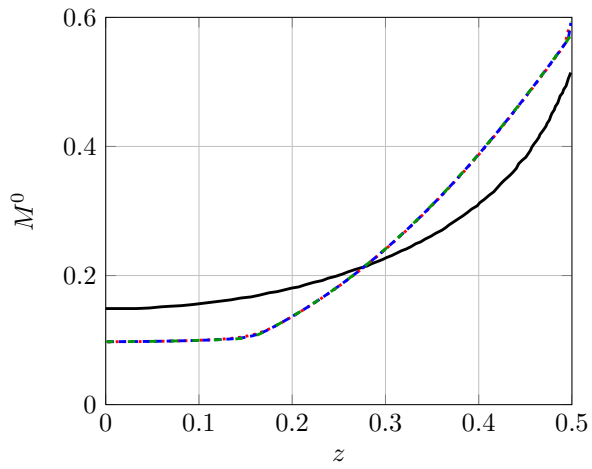
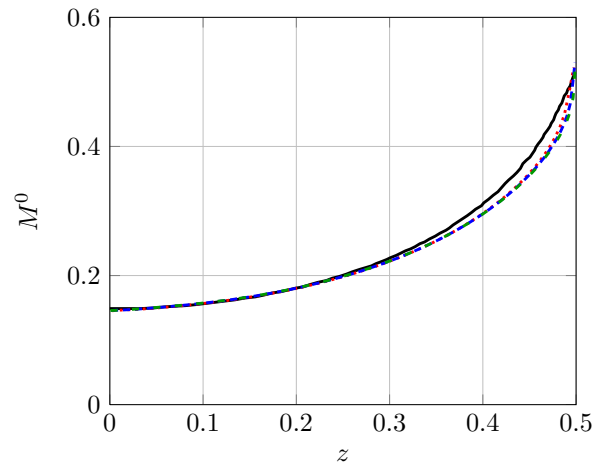


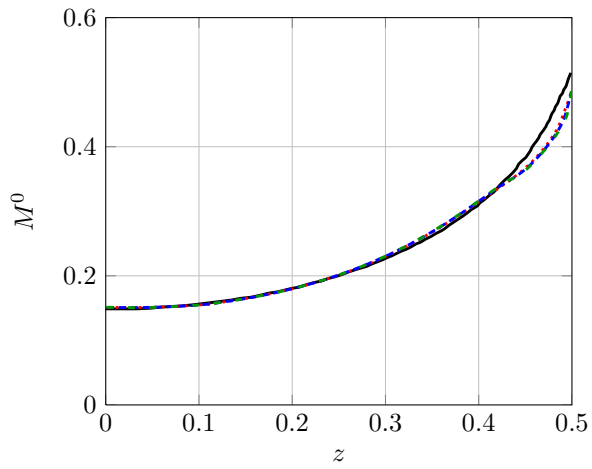
Figure 5.3 Solutions for the plane-source problem at $ct = 4$: Semi-analytic (—), 410 cells (.....), 820 cells (---), 1640 cells (-.-).



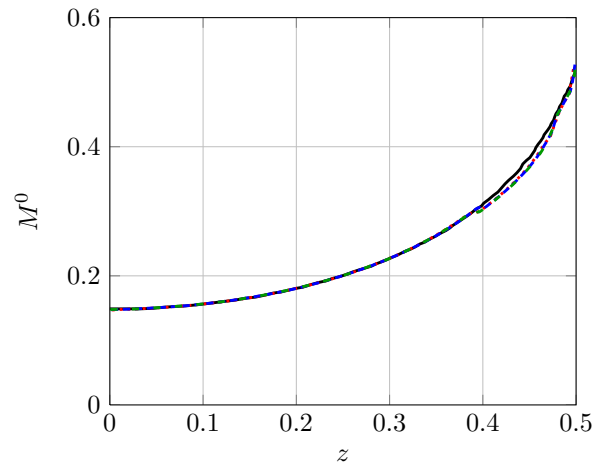
(a) EQMOM-1x4



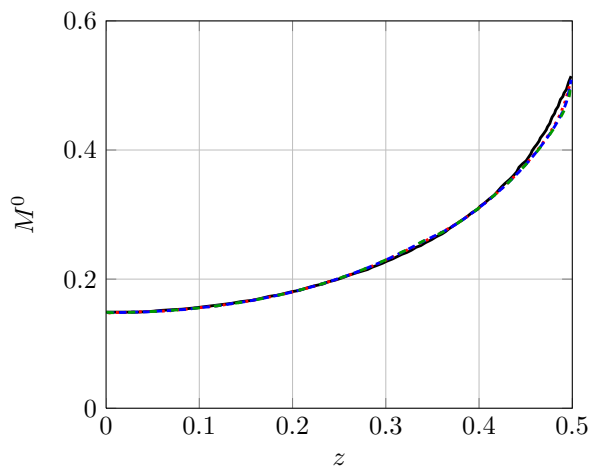
(b) EQMOM-2x6



(c) EQMOM-3x8



(d) EQMOM-4x10



(e) EQMOM-5x12

Figure 5.4 Solutions for the two-beam instability problem at steady state: Semi-analytic (—), 100 cells (⋯), 200 cells (---), 400 cells (- - -).

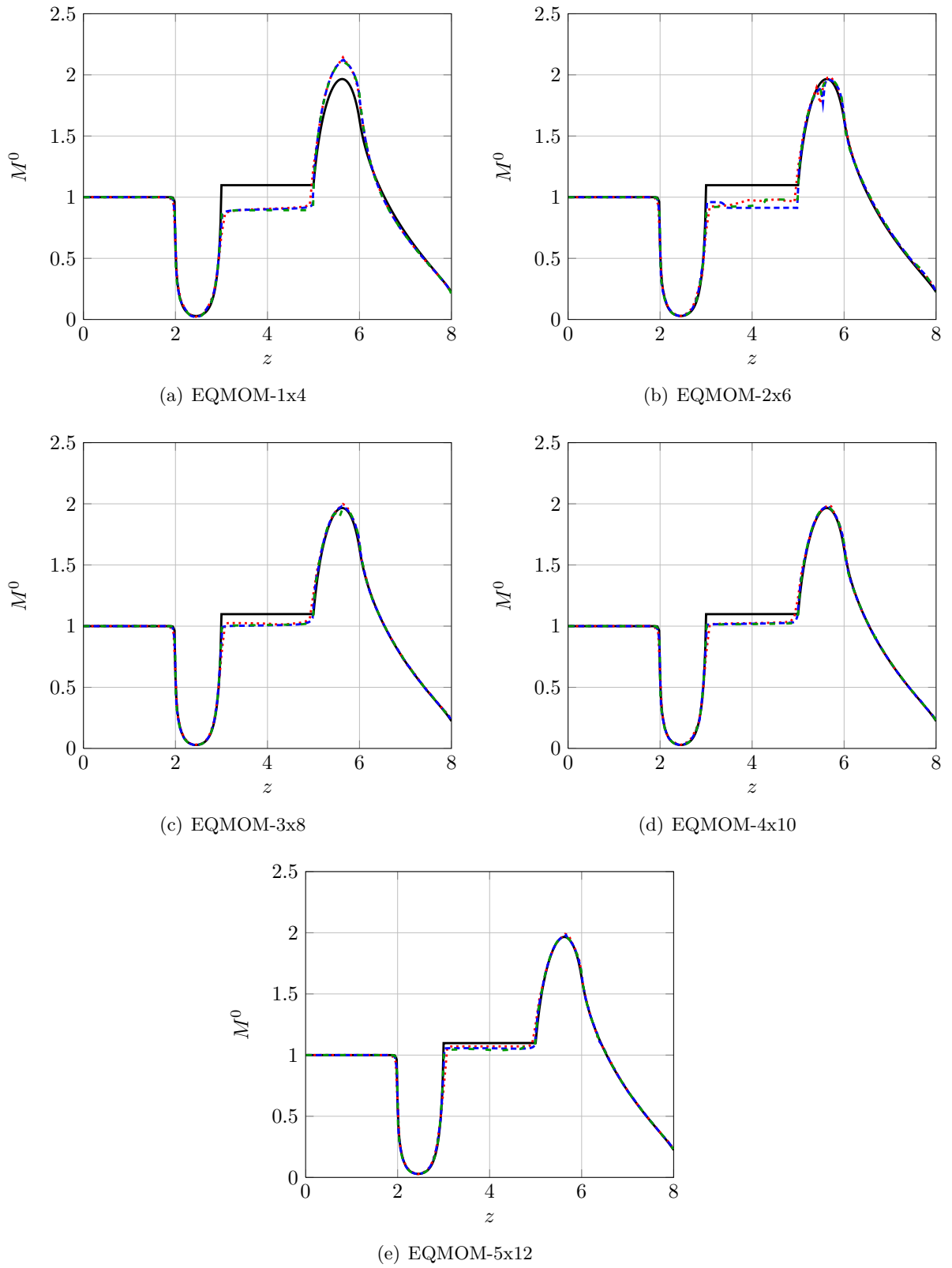


Figure 5.5 Solutions for the Reed cell problem at steady state: Reference (—), 100 cells (.....), 200 cells (---), 400 cells (- - -).

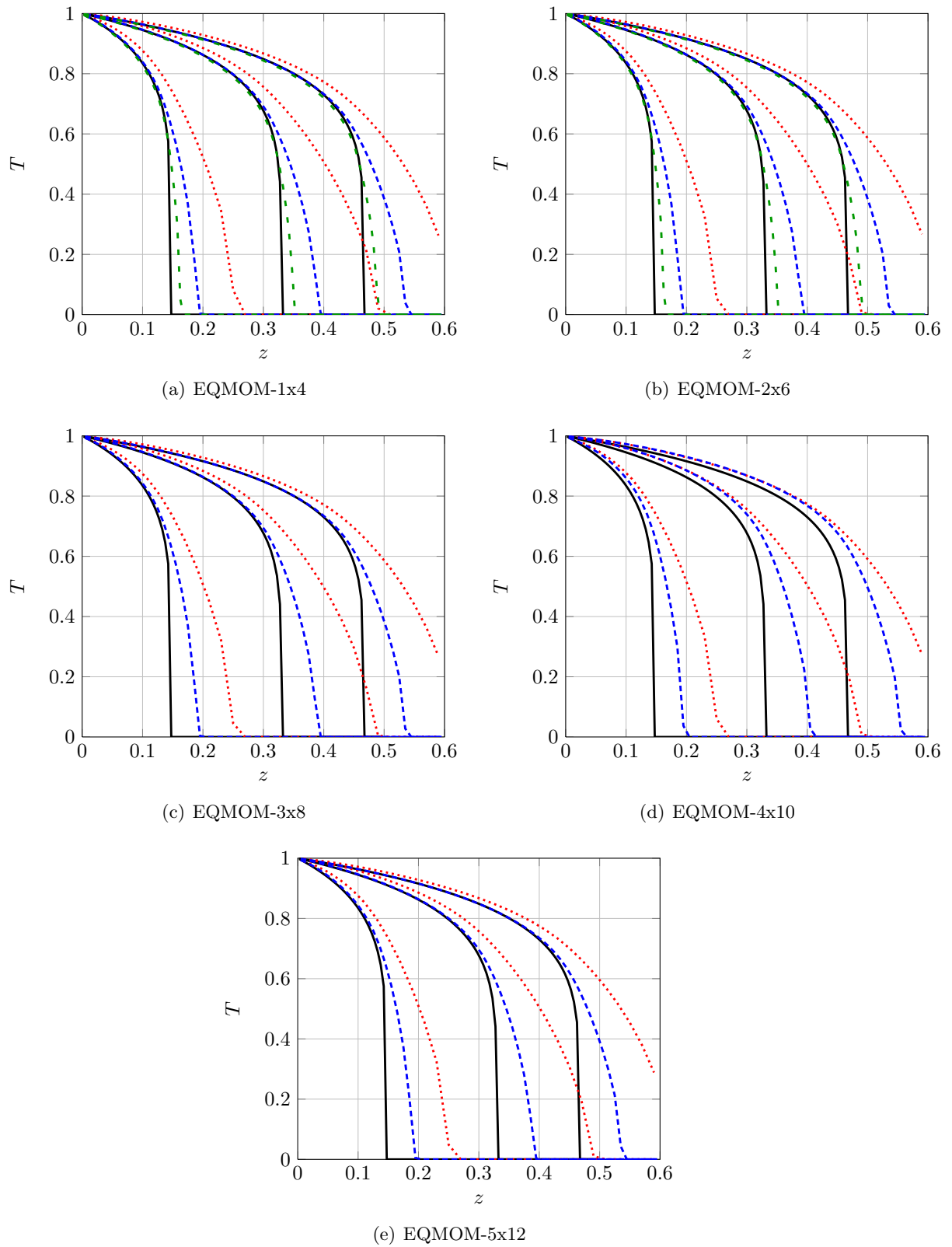


Figure 5.6 Solutions for the Marshak wave problem at $ct = 300, 1500, 3000$: Semi-analytic (—), 30 cells (.....), 60 cells (- - -), 120 cells (- - -).

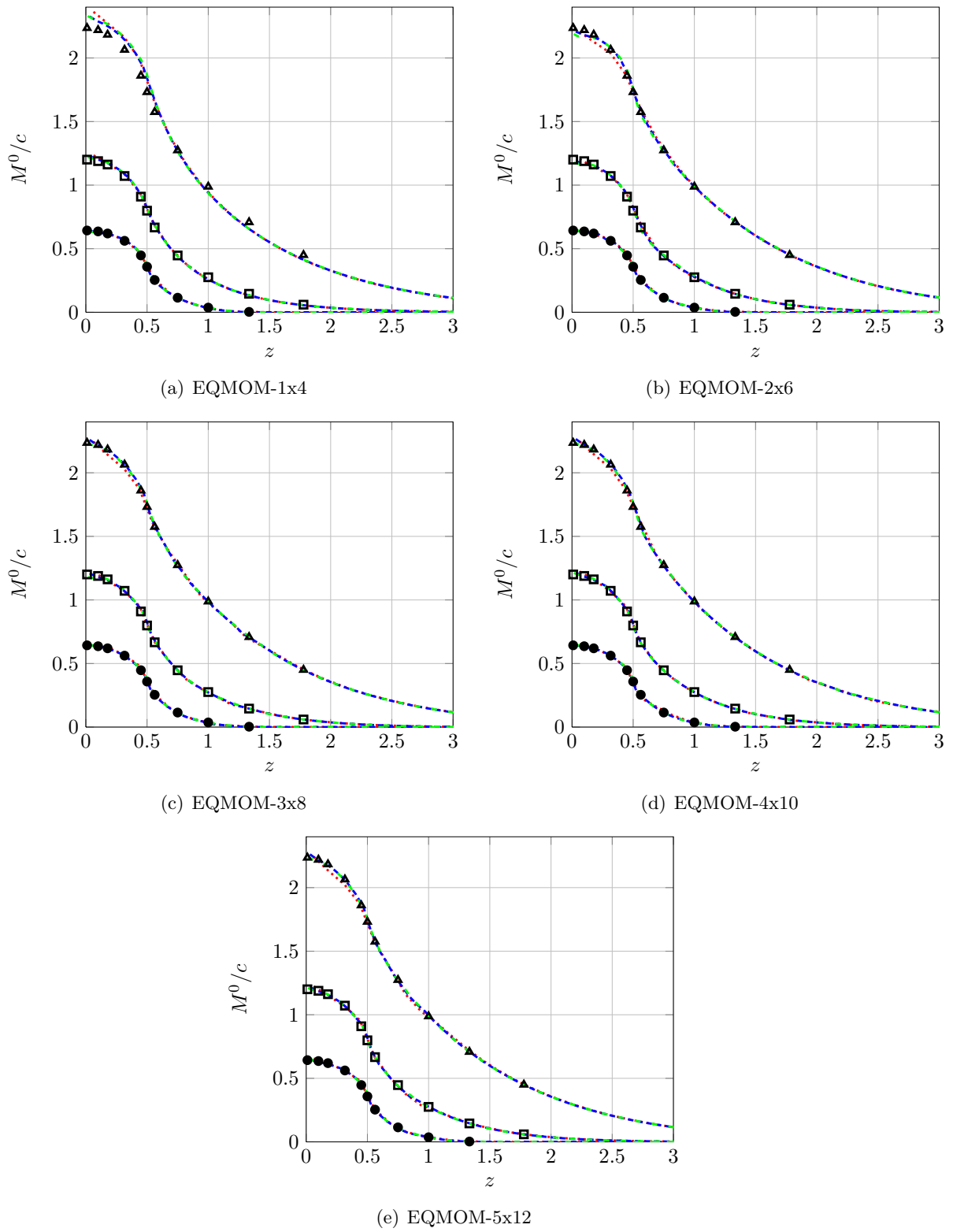


Figure 5.7 Solutions for the Su-Olson problem at $ct = 1, 3.16, 10$: Semi-analytic (\bullet , \square , \blacktriangle), 240 cells (\cdots), 480 cells ($-\cdot-$), 960 cells ($- -$).

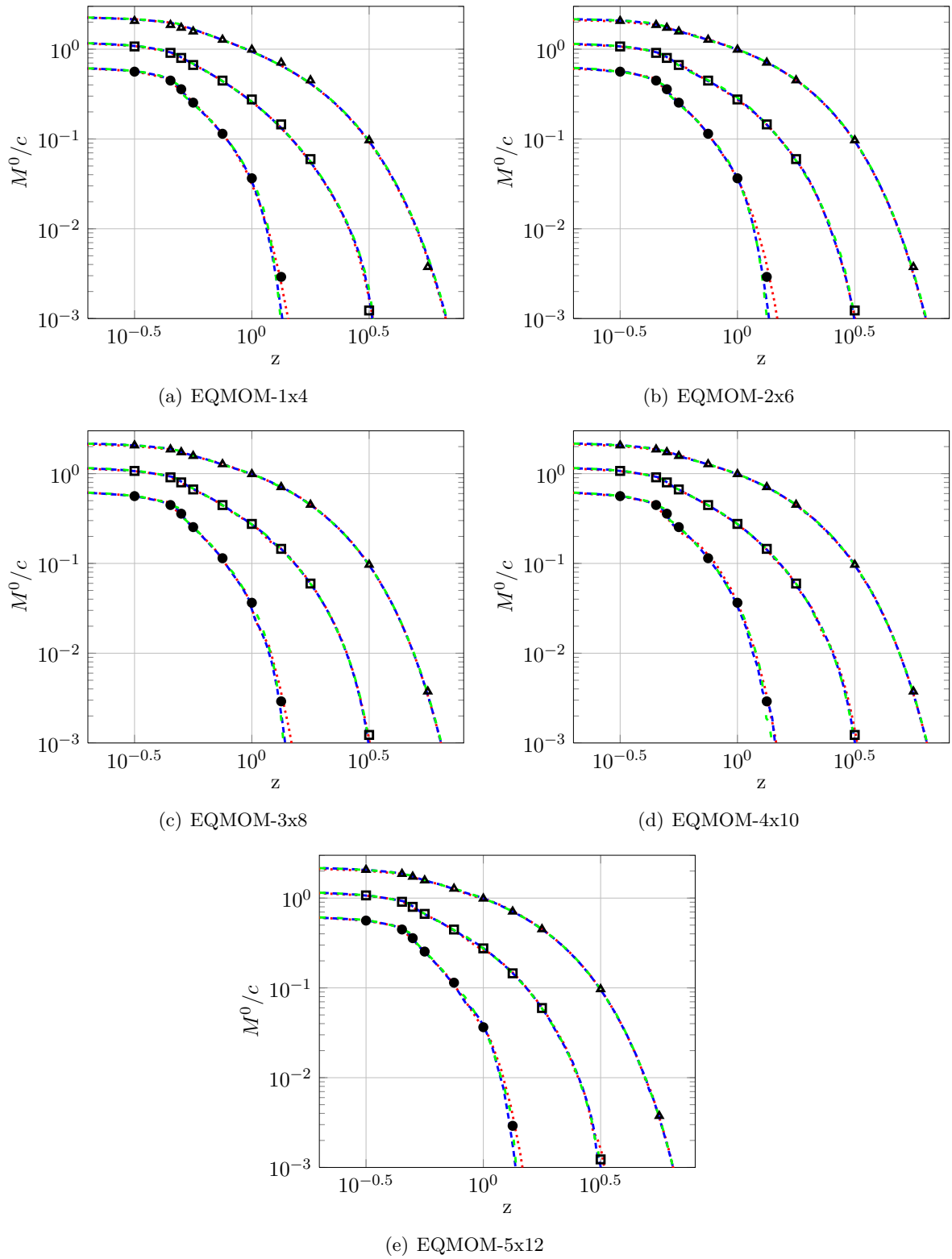


Figure 5.8 Solutions for the Su-Olson problem at $ct = 1, 3.16, 10$ on a logarithmic scale: Semi-analytic ($\bullet, \square, \blacktriangle$), 240 cells (\cdots), 480 cells ($-\cdots-$), 960 cells ($- \cdot - \cdot$).

CHAPTER 6. GENERAL CONCLUSIONS

Some general conclusions from the current research study are discussed below.

6.1 Development of high-order realizable schemes

The current research study has successfully explained why a discretization scheme using standard high-order reconstruction cannot guarantee realizability of the moment set. To counter this problem, a new class of realizable schemes has been developed for both convection and diffusion terms. It has been demonstrated that the new class of schemes attain close to formal high-order of accuracy for the problems in which abscissas are smoothly varying. Associated realizability conditions have been derived for the new schemes. These realizability conditions should be satisfied by the time step size in combination with the stability (CFL) conditions. In the current research study, only the explicit schemes have been considered. It is well known that the implicit schemes are unconditionally stable and time step size can be chosen arbitrarily large. A promising extension to the current research work will be the development of implicit schemes that are unconditionally realizable.

6.2 Bubble-column flow modeling using QMOM

A novel approach to model bubble-column flows using QMOM has been presented. Unlike the hydrodynamic models, the new approach holds for non-equilibrium flows as well. The two-dimensional simulations show promising results. Extension of the same framework to simulate three-dimensional flows is underway. The current research study only handle monodisperse flows. An approach to handle polydisperse flows is currently being formulated using EQMOM, however this approach is mono-kinetic. Development of a new approach that can handle poly-

dispersity with multi-kinetic transport will be an interesting extension.

6.3 Radiation transport modeling using EQMOM

The radiation transport equation coupled with the evolution equation for the material energy density has been solved using EQMOM. The advantages of EQMOM over other methods for radiation transport modeling have been demonstrated. EQMOM works quite well in optically thick and transition regimes. Some improvements need to be made to reduce the magnitude of oscillations in the optically thin regime. To solve a full three-dimensional radiation transport problem, a bi-variate version of EQMOM needs to be developed. In order to properly resolve the problems in optically thick regime on relatively coarse grids, realizable schemes that are consistent in the asymptotic diffusion limit are needed. It will also be interesting to apply EQMOM to other types of kinetic equations, for example Vlasov equation.

BIBLIOGRAPHY

- [1] ANILE, A. M., PENNISI, S. & SAMMARTINO, M. 1991 A thermodynamical approach to Eddington factors. *Journal of Mathematical Physics* **2**, 544–550.
- [2] ATHANASSOULIS, G. A. & GAVRILIADIS, P. N. 2002 The truncated Hausdorff moment problem solved by using kernel density functions. *Probabilistic Engineering Mechanics* **17**, 273–291.
- [3] AUTON, T. R. 1987 The lift force on a spherical body in a rotational flow. *Journal of Fluid Mechanics* **197**, 241–257.
- [4] BARTH, T. J. & JESPERSEN, D. C. 1989 The design and application of upwind schemes on unstructured meshes. *AIAA-89-0366*.
- [5] BARTH, T. J. & FREDERICKSON, P. O. 1990 High-order solution of the Euler equations on unstructured grids using quadratic reconstruction. *AIAA 90-0013*.
- [6] BATES, J. W., KNOLL, D. A., RIDER, W. J., LOWRIE, R. B. & MOUSSEAU, V. A. 2001 On consistent time-integration methods for radiation hydrodynamics in the equilibrium diffusion limit: Low-energy-density regime. *Journal of Computational Physics* **167**, 99–130.
- [7] BENAMOU, J.-D. 1996 Big ray tracing: Multivalued travel time field computation using viscosity solutions of the eikonal equation. *Journal of Computational Physics* **128**, 463–474.
- [8] BEYLICH, A. 2000 Solving the kinetic equation for all Knudsen numbers. *Physics of Fluids* **12**, 444–465.

- [9] BHATNAGAR, P. L., GROSS, E. P. & KROOK, M. 1954 A model for collisional processes in gases. I. Small amplitude processes in charged and neutral one-component systems. *Physical Review* **94**, 511–525.
- [10] BIRD, G. A. 1994 *Molecular gas dynamics and the direct simulation of gas flows*. Oxford University Press.
- [11] BOUCHUT, F., JIN, S. & LI, X. T. 2003 Numerical approximations of pressureless gas and isothermal gas dynamics. *SIAM Journal on Numerical Analysis* **41**, 135–158.
- [12] BRUNNER, T. A., HOLLOWAY, J. P. & LARSEN, E. W. 1997 On the use of maximum entropy Eddington factors in shielding calculations. *Transactions of the American Nuclear Society* **77**, 195–196.
- [13] BRUNNER T. A. 2002 Forms of approximate radiation transport. *Technical Report SAND2002-1778*, Sandia National Laboratories.
- [14] BUCHAN, A. G., PAIN, C. C., EATON, M. D., SMEDLEY-STEVENSON, R. P. & GODDARD, A. J. H. 2005 Linear and quadratic octahedral wavelets on the sphere for angular discretisations of the Boltzmann transport equation. *Annals of Nuclear Energy* **32**, 1224–1273.
- [15] CARRILLO, J. A., MAJORANA, A. & VECIL, F. 2007 A semi-Lagrangian deterministic solver for the semiconductor Boltzmann-Poisson system. *Communications in Computational Physics* **2**, 1027–1054.
- [16] CERCIGNANI, C. 1988 *The Boltzmann Equation and Its Applications*. Springer, New York.
- [17] CERCIGNANI, C., ILLNER, R. & PULVIRENTI, M. 1994 *The Mathematical Theory of Dilute Gases*. Springer-Verlag.
- [18] CHANDRASEKHAR, S. 1950 *Radiative transfer*. Dover.
- [19] CHAPMAN, S. & COWLING, T. G. 1970 *The Mathematical Theory of Nonuniform Gases*. Cambridge University Press, Cambridge.

- [20] CHU, C. K. 1965 Kinetic-theoretic description of the formation of a shock wave. *Physics of Fluids* **8**, 12–22.
- [21] COLLELA, P. 1984 The piecewise parabolic method for gas-dynamical simulations. *Journal of Computational Physics* **54**, 174–201.
- [22] DELNOIJ, E., LAMMERS, F. A., KUIPERS, J. A. M. & VAN SWAAIJ, W. P. M. 1997 Dynamic simulation of dispersed gas-liquid two-phase flow using a discrete bubble model. *Chemical Engineering Science* **52**, 1429.
- [23] DESHPANDE, S. 1986 A second order accurate, kinetic theory based, method for inviscid compressible flows. *Technical Report*, NASA Langley.
- [24] DEMIRDZIC, I. & MUZAFERIJA, S. 1994 Numerical method for coupled fluid flow, heat transfer and stress analysis using unstructured moving meshes with cells of arbitrary topology. *Computer Methods in Applied Mechanics and Engineering* **125**, 235.
- [25] DESJARDINS, O., FOX, R. O. & VILLEDIEU, P. 2008 A quadrature-based moment method for dilute fluid-particle flows. *Journal of Computational Physics* **227**, 2514–2539.
- [26] DEVANATHAN, N., DUDUKOVIC, M. P., LAPIN, A. & LUBBERT, A. 1995 Chaotic flow in bubble column reactors. *Chemical Engineering Science* **50**, 2661.
- [27] DREW, D. A. 1971 Averaged equations for two-phase flows. *Studies in Applied Mathematics* **1**, 205–231.
- [28] DREYER, W. 1987 Maximization of the entropy in non-equilibrium. *Journal of Physics A: Mathematical and General* **20**, 6505–6517.
- [29] DUBROCA, B. & FEUGEAS, J. L. 1999 Entropic moment closure hierarchy for the radiative transfer equation. *Comptes Rendus de l'Académie des Sciences - Series I* **329**, 915–920.
- [30] ENGQUIST, B. & RUNBORG, O. 1996 Multiphase computations in geometrical optics. *Journal of Computational and Applied Mathematics* **74**, 175–192.

- [31] ENWALD, H., PEIRANO, E. & ALMSTEDT, A. E. 1996 Eulerian two-phase flow theory applied to fluidization. *International Journal of Multiphase Flow* **22**, 21–66.
- [32] FLECK, J. A. & CUMMINGS, J. D. 1971 An implicit Monte Carlo scheme for calculating time and frequency dependent nonlinear radiation transport. *Journal of Computational Physics* **8**, 313–342.
- [33] FOX, R. O. 2008 A quadrature-based third-order moment method for dilute gas-particle flows. *Journal of Computational Physics* **227**, 6313–6350.
- [34] FOX, R. O. 2009a Higher-order quadrature-based moment methods for kinetic equations. *Journal of Computational Physics* **228**, 7771–7791.
- [35] FOX, R. O. 2009b Optimal moment sets for multivariate direct quadrature method of moments. *Industrial & Engineering Chemistry Research* **48**, 9686–9696.
- [36] FRANK, M., DUBROCA, B. & KLAR, A. 2006 Partial moment entropy approximation to radiative heat transfer. *Journal of Computational Physics* **218**, 1–18.
- [37] GANAPOL B. D. 1999 Homogeneous Infinite Media Time-Dependent Analytic Benchmarks for X-TM Transport Methods Development. *Technical Report*, Los Alamos National Laboratory.
- [38] GAUTSCHI, W. 2004 *Orthogonal polynomials: Computation and approximation*. Oxford University Press, Oxford.
- [39] GODUNOV, S. K. 1959 Finite difference methods for the computation of discontinuous solutions of the equations of fluid dynamics. *Math. Sbornik* **47**, 271–306.
- [40] GOSSE, L. 2002 Using K -branch entropy solutions for multivalued geometric optics computations. *Journal of Computational Physics* **180**, 155–182.
- [41] GOSSE, L., JIN, S. & LI, X. T. 2003 On two moment systems for computing multiphase semiclassical limits of the Schrödinger equation. *Mathematical Models and Methods in Applied Science* **13**, 1689–1723.

- [42] GOTTLIEB, S., SHU, C. W. & TADMOR, E. 2001 Strong stability-preserving high-order time discretization methods. *SIAM Review* **43**, 89–112.
- [43] GRAD, H. 1949 On the kinetic theory of rarefied gases. *Communications on Pure and Applied Mathematics* **2**, 331–407.
- [44] GRIENBERGER, J. & HOFMAN, H. 1992 Investigations and modelling of bubble columns. *Chemical Engineering Science* **47**, 2215.
- [45] HAUCK, C. D., LEVERMORE, C. D. & TITS, A. L. 2008 Convex duality and entropy-based moment closures: Characterizing degenerate densities. *SIAM Journal on Control and Optimization* **47**, 1977–2015.
- [46] HAUCK, C. D. & MCCLARREN, R. G. 2010 Positive P_N closures. *SIAM Journal on Scientific Computing* **32**, 2603–2626.
- [47] HAUCK, C. D. 2011 High-order entropy-based closures for linear transport in slab geometries. *Communications in Mathematical Sciences* **9**, 187–205.
- [48] HJERTAGER, B. H. & MORUD, K. 1995 Computational fluid dynamics of bioreactors. *Modelling, Identification and Control* **16**, 177.
- [49] HOWELL, J. R. 1998 The Monte Carlo method in radiative heat transfer. *Journal of Heat Transfer* **120**, 547–560.
- [50] JIN, S. & LI, X. T. 2003 Multi-phase computations of the semiclassical limit of the Schrödinger equation and related problems: Whitham vs Wigner. *Physica D* **182**, 46–85.
- [51] JIN, S., LIU, H., OSHER, S. & TSAI, R. 2005 Computing multi-valued physical observables for the semiclassical limit of the Schrödinger equation. *Journal of Computational Physics* **205**, 222–241.
- [52] JUNG, J., CHIJIWA, H., KOBAYASHI, K. & NISHIHARA, H. 1972 Discrete ordinate neutron transport equation equivalent to P_L approximation. *Nuclear Science and Engineering* **49**, 1–9.

- [53] KERSHAW, D. S. 1976 Flux limiting nature's own way. *Technical Report UCRL-78378*, Lawrence Livermore National Laboratory.
- [54] KLAR, A. 1998 An asymptotic-induced scheme for nonstationary transport equations in the diffusive limit. *SIAM Journal on Numerical Analysis* **35**, 1073–1094.
- [55] KLAR, A. & UNTERREITER, A. 2002 Uniform stability of a finite difference scheme for transport equations in diffusive regimes. *SIAM Journal on Numerical Analysis* **42**, 891–913.
- [56] KNIGHT, D. D. 2006 *Elements of Numerical Methods for Compressible Flows*. Cambridge University Press, Cambridge.
- [57] KOCH, R., KREBS, W., WITTING, S. & VISKANTA, R. 1995 The discrete ordinate quadrature schemes for multidimensional radiative transfer. *Journal of Quantitative Spectroscopy and Radiative Transfer* **53**, 353–372.
- [58] LAPIN, A. & LUBBERT, A. 1994 Numerical simulation of the dynamics of two phase gas-liquid flows in bubble columns. *Chemical Engineering Science* **49**, 3661–3674.
- [59] LARSEN, E. W., POMRANING, G. C. & BADHAM, V. C. 1983 Asymptotic analysis of radiative transfer problem. *Journal of Quantitative Spectroscopy and Radiative Transfer* **29**, 285–310.
- [60] LEVEQUE, R. 2002 *Finite Volume Methods for Hyperbolic Problems*. Cambridge University Press, Cambridge.
- [61] LEVERMORE, C. D. & POMRANING, G. C. 1981 A flux-limited diffusion theory. *The Astrophysical Journal* **248**, 321–334.
- [62] LEVERMORE, C. D. 1984 Relating Eddington factors to flux limiters. *Journal of Quantitative Spectroscopy and Radiative Transfer* **31**, 149–160.
- [63] LI, X. T., WÖHLBIER, J. G., JIN, S. & BOOSKE, J. H. 2004 Eulerian method for computing multivalued solutions of the Euler-Poisson equations and applications to wave breaking in klystrons. *Physical Review E* **70**, 016502.

- [64] LOSTEC, N. L., FOX, R. O., SIMONIN, O. & VILLEDIEU, P. 2008 Numerical description of dilute particle-laden flows by a quadrature-based moment method. *Proceedings of the Summer Program 2008*, Center for Turbulence Research, Stanford University, 209–221.
- [65] MARCHISIO, D. L. & FOX, R. O. 2005 Solution of population balance equations using the direct quadrature method of moments. *Journal of Aerosol Science* **36**, 43–73.
- [66] MARK J. C. 1945 The spherical harmonics method, Part II. *Technical Report MT 97*, National Research Council of Canada.
- [67] MASSOT, M., LAURENT, F., KAH, D. & DE CHAISEMARTIN, S. 2010 A robust moment method for evaluation of the disappearance rate of evaporating sprays. *SIAM Journal on Applied Mathematics* **70**, 3203–3234.
- [68] MATHUR, S. R. & MURTHY, J. Y. 1997a A pressure based method for unstructured meshes. *Numerical Heat Transfer* **31**, 195.
- [69] MATHUR, S. R. & MURTHY, J. Y. 1997b Pressure boundary conditions for incompressible flow using unstructured meshes. *Numerical Heat Transfer* **32**, 283.
- [70] MCCLARREN, R. G., EVANS, T. M., LOWRIE, R. B. & DENSMORE, J. D. 2008 Semi-implicit time integration for P_N thermal radiative transfer. *Journal of Computational Physics* **227**, 7561–7586.
- [71] MCGRAW, R. 1997 Description of aerosol dynamics by the quadrature method of moments. *Aerosol Science and Technology* **27**, 255–265.
- [72] MCGRAW, R. 2006 Correcting moment sequences for errors associated with advective transport. (http://www.ecd.bnl.gov/pubs/momentcorrection_mcgraw2006.pdf).
- [73] MCGRAW, R. 2007 Numerical advection of correlated tracers: Preserving particle size/composition moment sequences during transport of aerosol mixtures. *Journal of Physics: Conference Series* **78**, 012045.
- [74] MEAD, L. R. & PAPANICOLAOU, N. 1984 Maximum entropy in the problem of moments. *Journal of Mathematical Physics* **25**, 2404–2417.

- [75] MIHALAS, D. & WEIBEL-MIHALAS, B. 1999 *Foundations of radiation hydrodynamics*. Dover.
- [76] NICODIN, I. & GATIGNOL, R. 2006 Unsteady half-space evaporation and condensation problems on the basis of the discrete kinetic theory. *Physics of Fluids* **18**, 127105.
- [77] OGATA, Y., IM, H.-N. & YABE, T. 2007 Numerical method for Boltzmann equation with Soroban-grid CIP method. *Communications in Computational Physics* **2**, 760–782.
- [78] OLSON, G. L., AUER, L. H. & HALL, M. L. 2000 Diffusion, P1, and other approximate forms of radiation transport. *Journal of Quantitative Spectroscopy and Radiative Transfer* **64**, 619–634.
- [79] PASSALACQUA, A., FOX, R. O., GARG, R. & SUBRAMANIAM, S. 2010 A fully coupled quadrature-based moment method for dilute to moderately dilute fluid-particle flows. *Chemical Engineering Science* **65**, 2267.
- [80] PASSALACQUA, A. & FOX, R. O. 2011 Advanced continuum modeling of gas-particle flows beyond the hydrodynamic limit. *Applied Mathematical Modelling* **35**, 1616–1627.
- [81] PATANKAR, S. V. 1980 *Numerical Heat Transfer and Fluid Flow*. McGraw-Hill.
- [82] PERTHAME, B. 1990 Boltzmann type schemes for compressible Euler equations in one and two space dimensions. *SIAM Journal on Numerical Analysis* **29**, 1–19.
- [83] PETSCHKE A. G., WILLIAMSON, R. E. & WOOTEN, J. K. 1960 The penetration of radiation with constant driving temperature. *Technical Report*, Los Alamos National Laboratory.
- [84] POMRANING, G. C. 1973 *The equations of radiation hydrodynamics*. Pergamon Press.
- [85] PRATHER, M. J. 1986 Numerical advection by conservation of second-order moments. *Journal of Geophysical Research* **91**, 6671–6681.

- [86] PRESS, W. H., TEUKOLSKY, S. A., VETTERLING, W. T. & FLANNERY, B. P. 1992 *Numerical Recipes in Fortran 77: The Art of Scientific Computing*. Cambridge University Press, Cambridge.
- [87] PULLIN, D. I. 1980 Direct simulation methods for compressible inviscid ideal gas-flows. *Journal of Computational Physics* **34**, 53–66.
- [88] RANADE, V. V. 1992 Flow in bubble column: some numerical experiments. *Chemical Engineering Science* **47**, 1857–1869.
- [89] REED, W. H. 1971 New difference schemes for the neutron transport equation. *Nuclear Science and Engineering* **46**, 31–39.
- [90] REED, W. H. 1972 Spherical harmonic solutions of the neutron transport equation from discrete ordinate codes. *Nuclear Science and Engineering* **49**, 10–19.
- [91] RHIE, C. M. & CHOW, W. L. 1983 Numerical study of the turbulent flow past an airfoil with trailing edge separation. *AIAA Journal* **21**, 1525–1532.
- [92] RIBOUX, G., RISSO, F. & LEGENDRE, D. 2010 Experimental characterization of the agitation generated by bubbles rising at high Reynolds number. *Journal of Fluid Mechanics* **643**, 509–539.
- [93] RIDER, W. J., & KNOLL, D. A. 1999 Time step size selection for radiation diffusion calculations. *Journal of Computational Physics* **152**, 790–795.
- [94] RUNBORG, O. 2000 Some new results in multiphase geometrical optics. *Mathematical Modelling and Numerical Analysis* **34**, 1203–1231.
- [95] RUNBORG, O. 2007 Mathematical models and numerical methods for high frequency waves. *Communications in Computational Physics* **2**, 827–880.
- [96] SAKIZ, M. & SIMONIN, O. 1998 Numerical experiments and modelling of non-equilibrium effects in dilute granular flows. *Proceedings of the 21st International Symposium on Rarefied Gas Dynamics*, Cépaduès-Éditions, Toulouse, France.

- [97] SATO, Y. & SEKOGUCHI, K. 1975 Liquid velocity distribution in two-phase bubble flow. *International Journal of Multiphase Flow* **2**, 79–95.
- [98] SCHILLER, L. & NAUMANN, A. 1935 A drag coefficient correlation. *V. D. I. Zeitung* **77**, 318–320.
- [99] SHERMAN, M. P. 1967 Moment methods in radiative transfer problems. *Journal of Quantitative Spectroscopy and Radiative Transfer* **7**, 89–109.
- [100] SHOHAT, J. A. & TAMARKIN J. D. 1943 *The problem of moments*. American Mathematical Society, New York.
- [101] SOKOLICHIN, A. & EIGENBERGER, G. 1994 Gas liquid flow in bubble columns and loop reactors. Part I. Detailed modelling and numerical simulation. *Chemical Engineering Science* **49**, 5735.
- [102] STRUCHTRUP, H. 1997 An extended moment method in radiative transfer: The matrices of mean absorption and scattering coefficients. *Annals of Physics* **257**, 111–135.
- [103] STRUCHTRUP, H. 1998 On the number of moments in radiative transfer problems. *Annals of Physics* **266**, 1–26.
- [104] STRUCHTRUP, H. 2005 *Macroscopic Transport Equations for Rarefied Gas Flows*. Springer, Berlin.
- [105] SU, B. & OLSON, G. L. 1997 An analytical benchmark for non-equilibrium radiative transfer in an isotropically scattering medium. *Annals of Nuclear Energy* **24**, 1035–1055.
- [106] SU, B. 2001 Variable Eddington factors and flux limiters in radiative transfer. *Nuclear Science and Engineering* **137**, 281–297.
- [107] TOMIYAMA, A., MATSUOKA, T., FUKUDA, T. & SAKAGUCHI, T. 1995 A simple numerical method for solving an incompressible two-fluid model in a general curvilinear coordinate system. *Advances in Multiphase Flow Society of Petroleum Engineers*, 241–252.

- [108] TOMIYAMA, A., KATAOKA, I., ZUN, I. & SAKAGUCHI, T. 1998 Drag coefficients of single bubbles under normal and microgravity conditions. *JSME International Journal Series B, Fluids and Thermal Engineering* **41**, 472–479.
- [109] TORRILHON, M. & STRUCHTRUP, H. 2004 Regularized 13-moment equations: shock structure calculations and comparison to Burnett models. *Journal of Fluid Mechanics* **513**, 171–198.
- [110] TORVIK, R. & SVENDSEN, H. F. 1990 Modelling of slurry reactors, a fundamental approach. *Chemical Engineering Science* **45**, 2325.
- [111] TRAPP, J. A. & MORTENSEN, G. A. 1993 A discrete particle model for bubble slug two phase flow. *Journal of Computational Physics* **107**, 367.
- [112] VANCE, M. W., SQUIRES, K. D. & SIMONIN, O. 2006 Properties of the particle velocity field in gas-solid turbulent channel flow. *Physics of Fluids* **18**, 063302.
- [113] VAN LEER, B. 1997 Towards the ultimate conservative difference schemes V. A second order sequel to Godunov's method. *Journal of Computational Physics* **135**, 229–248.
- [114] VENKATKRISHNAN, V. 1995 Convergence to steady state solutions of the Euler equations on unstructured grids with limiters. *Journal of Computational Physics* **118**, 120–130.
- [115] VIKAS, V., WANG, Z. J., PASSALACQUA, A. & FOX, R. O. 2011a Realizable high-order finite-volume schemes for quadrature-based moment methods. *Journal of Computational Physics* **230**, 5328–5352.
- [116] VIKAS, V., YUAN, C., WANG, Z. J. & FOX, R. O. 2011b Modeling of bubble-column flows with quadrature-based moment methods. *Chemical Engineering Science* **66**, 3058–3070.
- [117] VLASOV, A. A. 1938 On vibration properties of electron gas. *Journal of Experimental and Theoretical Physics* **8**, 291–317.
- [118] WANG, Z. J. 1998 A Quadtree-based adaptive Cartesian/Quad grid flow solver for Navier-Stokes equations. *Computers & Fluids* **27**, 529–549.

- [119] WANG, Z. J. 2002 Spectral (finite) volume method for conservation laws on unstructured grids: Basic Formulation. *Journal of Computational Physics* **178**, 210–251.
- [120] WANG, Z. J. 2007 High order methods for Euler and Navier Stokes equations on unstructured grids. *Journal of Progress in Aerospace Sciences* **43**, 1–47.
- [121] WHEELER, J. C. 1974 Modified moments and Gaussian quadratures. *Rocky Mountain Journal of Mathematics* **4**, 287–296.
- [122] WILLIAMS, F. A. 1958 Spray combustion and atomization. *Physics of Fluids* **1**, 541–545.
- [123] WÖHLBIER, J. G., JIN, S. & SENGELE, S. 2005 Eulerian calculations of wave breaking and multivalued solutions in a traveling wave tube. *Physics of Plasmas* **12**, 023106.
- [124] WRIGHT, D. L. 2007 Numerical advection of moments of the particle size distribution in Eulerian models. *Journal of Aerosol Science* **38**, 352–369.
- [125] WU, C. L., ZHAN, J. M., LIC, Y. S. & LAM, K. S. 2006 Dense particulate flow model on unstructured mesh. *Chemical Engineering Science* **61**, 5726.
- [126] YUAN, C. & FOX, R. O. 2011 Conditional quadrature method of moments for kinetic equations. *Journal of Computational Physics* **230**, 8216–8246.
- [127] YUAN, C., LAURENT, F. & FOX, R. O. 2012 An extended quadrature method of moments for population balance equations. *Journal of Aerosol Science* **51**, 1–23.